Role of Radiation Treatment on Bone Strength and Fracture Risk

By

Shannon R. Emerzian

A dissertation submitted in partial satisfaction of the

requirements for the degree of

Doctor of Philosophy

In

Engineering – Mechanical Engineering

in the

Graduate Division

of the

University of California, Berkeley

Committee in charge:

Professor Tony M. Keaveny, Chair
Professor Lisa Pruitt
Professor Jasmina Vujic
Professor Rebecca Abergel

Summer 2021

Role of Radiation Treatment on Bone Strength and Fracture Risk

Copyright 2021
by
Shannon R. Emerzian

Abstract

Role of Radiation Treatment on Bone Strength and Fracture Risk

By

Shannon R. Emerzian

Doctor of Philosophy in Engineering – Mechanical Engineering

University of California, Berkeley

Professor Tony M. Keaveny, Chair

While bones are highly adaptable and regulated by external and internal stimuli, their structural integrity can be compromised by aging, diseases such as osteoporosis, and treatments such as radiation therapy. Thus, understanding of the fundamental connection between the effect of treatment on bone strength and fracture risk is critical to understanding the etiology of bone fractures as well as the mechanisms by which aging, disease, and treatments can alter the mechanical performance of bone. However, the connection between treatment effects on changes in bone strength, and bone strength changes on fracture risk, is not completely understood. First, it is unclear how much treatment-induced changes in bone strength are due to changes in bone mass versus in microstructure versus in tissue material. Second, it is unknown why small treatment-induced changes in bone strength are associated with large changes in fracture risk. To address this, we conducted two studies exploring the connection between treatment effects on bone strength and fracture risk. The overall goal of this dissertation was to develop a better understanding of the relative treatment effects on bone strength and to elucidate how small changes in bone strength can be associated with large changes in fracture risk. Together, the work in this dissertation will lead to improved understanding of radiation and osteoporosis treatments and provide new insight into how small changes in bone strength influence fracture risk.

First, using the latest advances in microcomputed tomography and high-resolution finite element modeling combined with biomechanical characterization, we investigated the effect of radiation treatment on bone strength in a rat model of localized irradiation. Changes in material accounted for 24% of the overall observed biomechanical effect, while changes in mass and microstructure together accounted for about 76% of the observed reduction in vertebral strength (~60% and 16%, respectively). For the first time we have directly quantified the contribution of tissue material changes to whole bone strength following irradiation treatment. If the observed material effect is present clinically, it may help to explain the increased fracture risk for patients undergoing radiation therapy despite the inconclusive correlation between irradiation and decreased bone mass. Importantly, we have presented a useful evaluation tool in any application where the effects of mass, microstructure, and material on bone strength are at play, including aging, disease, or pre-clinical evaluation of therapies. This work expands our understanding of the radiosensitivity of

bone tissue and emphasizes the complex nature of bone strength loss following exposure to radiation.

Next, we developed a theoretical framework to mechanistically evaluate how changes in bone strength are linked to changes in fracture risk. As there are no clinical bone strength data available to develop a relevant model for radiation therapy-induced fracture risk, we utilized a better characterized treatment—osteoporosis antiresorptive drugs. Through a Monte Carlo approach with conditional probability and data from placebo-controlled osteoporosis trials, we replicated a clinically observed treatment efficacy of 41% using simulated treatment-induced changes in bone strength. Our results demonstrated the sensitivity of fracture risk reduction to the net difference in treatment-induced bone strength changes, the baseline bone strength, and the eligibility criteria bounding the population. Importantly, by incorporating bone strength changes into the model, we were able to duplicate the risk reduction in a clinical trial and provide a mechanistic explanation for the observed large changes in fracture risk—a relatively low number of fractures with an inordinately large weight on efficacy calculations. While the results are specific to hip fracture risk reduction due to osteoporotic treatments in post-menopausal women, this model can be easily adapted to explore the influence of other treatments on fracture risk. For example, the current model has provided important understanding and may help to explain the increased fracture risk for patients undergoing radiation therapy despite the inconclusive correlation between irradiation and decreased bone mass.

Together, the resulting insight from these studies can aid in understanding the underlying mechanisms influencing changes in bone strength and their connection to fracture risk, which may help to improve pre-clinical evaluation of therapies and their potential for fracture risk. Specifically, this dissertation provided insight into the effect of treatment on bone strength and fracture risk, especially the role of radiation and osteoporosis drug therapies. Collectively, this dissertation answered fundamental open questions regarding treatment effects on bone strength and fracture risk and highlighted areas in need of further research.

Table of Contents

Abstract *1*

List of Figures ..... *iv*

List of Tables ..... *vii*

Acknowledgements ..... *viii*

1 Introduction *1*

1.1 Bone **3**

1.1.1 Composition and Structure 3

1.1.2 Bone modeling and remodeling 5

1.1.3 Mechanical behavior of bone 7

1.2 Radiation, radiobiology, and radiation therapy **11**

1.2.1 Radiobiology: the biological damage of radiation 12

1.2.2 Radiation therapy for cancer treatment 13

1.2.3 Increased fracture risk following clinical radiation therapy 15

1.3 Effect of radiation therapy and osteoporosis drug therapy on bone **15**

1.3.1 Response of bone to radiation 15

1.3.2 Response of bone to osteoporosis drug therapies 16

1.4 Objective and Scope **16**

2 Relative Effects of Radiation-Induced Changes in Bone Mass, Microstructure, and Tissue Material Behavior on Vertebral Strength in a Rat Model *18*

2.1 Introduction **18**

2.2 Methods **19**

2.2.1 Study design and specimens 19

2.2.2 Specimen preparation and micro-CT imaging 20

2.2.3 Biomechanical testing 21

2.2.4 Nonlinear finite element analysis 22

2.2.5 Statistical analyses 22

2.3 Results 22

2.3.1 MicroCT analysis 22

2.3.2 Biomechanical testing and finite element analyses 25

2.4 Discussion 27

3 Theoretical Effects of Treatment-Induced Changes in Bone Strength on Fracture Risk Reduction in Post-Menopausal Women 30

3.1 Introduction 30

3.2 Methods 31

3.2.1 Baseline cohort 32

3.2.2 Eligibility criteria 34

3.2.3 Treatment-related parameters 34

3.2.4 Fracture risk prediction 35

3.2.5 Outcome — Risk Reduction 36

3.3 Results 37

3.3.1 Reference case 37

3.3.2 Baseline population bone strength mean 38

3.3.3 Baseline population bone strength changes 39

3.3.4 Eligibility criteria 40

3.4 Discussion 41

3.5 Supplementary Material 44

4 Conclusions 46

5 References 49

6 Appendices 62

6.1 Fracture Risk Modeling – Definition of Key Variables 62

6.2 Standard Operating Procedures 64

6.2.1 In vivo X-Ray Irradiation at X-RAD 320 in Li Ka Shing 64

6.2.2 Rat Dissection and Cleaning: Vertebrae + Femur 72

6.2.3 Specimen Preparation of Whole Rat Vertebrae for Biomechanical Testing 75

6.2.4 Method for Scanning Rat Vertebrae on BIDMC ChaCha microCT Scanner 83
6.2.5 Image Processing of Rat Vertebral microCT Scans 85
6.2.6 Build Connected Volume for Rat Vertebral Body Finite Element Analysis 91
6.2.7 Nonlinear FE Workflow and Protocol for Rat Vertebral Bodies 102
6.2.8 Nonlinear FEA Post-Processing with MATLAB 119
6.2.9 Compressive Testing of Whole Rat Vertebrae on the MTS 128

List of Figures

Figure 1-1: Hierarchical structures of bone from the sub-micron length scale to the centimeter length scale. Image adapted from [33]. 3

Figure 1-2: Cross-sections of a human vertebral body (left) and proximal femur (right) showing typical arrangements of cortical and trabecular bone. Image adapted from [34]. 4

Figure 1-3: A representation of the bone remodeling process, shown in two dimensions. Image adapted from [48]. 6

Figure 1-4: Schematic showing the role of bone quality in whole bone strength (i.e., resistance to fracture). Factors that contribute to bone strength/fracture resistance but are not explained by measures of bone mass/quantity are bone quality effects. Image adapted from [51] 7

Figure 1-5: Hypothetical strength-density relationships for normal bone and bone from two different treatment groups. Both treatment groups show the same increase in bone strength. However, the relationship between the bone strength and density in bone exposed to Treatment 1 has an increased slope, indicating improved bone quality. In contrast, bone exposed to Treatment 2 shows a similar relationship between bone strength and density as compared to the control group, suggested that strength effects are due to bone quantity, not quality, effects. Adapted from [51]. 8

Figure 1-6: (A) Mechanical testing modes in bone. When the ends of the bone are pulled apart or pushed together, the bone is under axial tension and compression, respectively. In contrast, if load is applied across the bone, shear is induced. If the ends of the bone are twisted relative to one another, the bone is under torsion. Bones can also be loaded in bending, with load and support applied perpendicular to the long axis. Figure adapted from [61]. (B) Load-displacement behavior for a whole bone structural test. Many important characteristics can be determined by analyzing this curve, including the strength, stiffness, deformation, and energy dissipation. The stiffness is determined from the slope of the initial linear region, where F is load and $\boldsymbol{\delta}$ is displacement. The strength is the load required to fail the whole bone, or the ultimate load during a compressive axial test. Work can be calculated as the area under the curve; work/energy can be calculated for the area under the curve until yield, ultimate load, or failure. Image adapted from [61]. 10

Figure 1-7: Direct and indirect actions of radiation. The structure of DNA is shown schematically. In indirect action, the secondary electron interacts with a water molecule to produce a free radical (e.g., hydroxyl radical, OH), which in turn produces the damage to the DNA. In direct action, a secondary electron resulting from absorption of an X-ray interacts with the DNA to produce an effect. S, sugar; P, phosphorus; A, adenine; T, thymine; G, guanine; C, cytosine. Image adapted from [75]. 13

Figure 2-1: Dorsal view of rat with target treatment area in red; image adapted from [167] 20

Figure 2-2: Specimen preparation. A. Vertebral body inside 3D printed disposable jig with alignment pin. Posterior elements are secured in polymethylmethacrylate (PMMA). B. MicroCT image of prepared vertebral body with plano-parallel surfaces. 21

Figure 2-3: Effect of radiation treatment, sex, and their interaction on trabecular microarchitecture parameters. Data are shown as mean ± 95% confidence interval. Superscripts show significant effect ($p < 0.05$) for treatment†, sex‡, and their interaction$^{\wedge}$. 23

Figure 2-4: Vertebral strength (in newtons [N]) for experimental biomechanical testing versus FEA, color-coded by treatment group. General linear least-squares regression (adjusted $R^2 = 0.86$; all data pooled), showing the treatment effect in this relationship; the term for treatment was significant before ($p \leq 0.02$) and after ($p \leq 0.03$) removing the non-significant interaction term. The vertical offset of lines indicates a treatment effect on material properties that altered overall vertebral strength by 27.6 N, or 7.6% of the average value. For reference, the dashed line shows the line of unity (Y=X). 26

Figure 3-1: Flowchart of the theoretical framework developed to investigate how small changes in bone strength influence the probability of fracture in a placebo (left) and treated (right) cohorts. All values are based on data from the literature, including population size [24], baseline bone strength mean and standard deviation [24], [155], bone strength change [24], [29], rate of fall [156], and fracture criterion [151]. All data are shown as mean ± standard deviation; values marked with an asterisk (*) were varied parametrically. 31

Figure 3-2: Femoral strength distributions for the baseline cohort (top; n = 16,000 patients) and the two groups (n = 8,000 patients for each placebo (left) and treated (right)) before the trial (middle row) and after the trial (bottom row) for a single Monte Carlo iteration. Red vertical line indicates reference baseline femoral strength mean of 3,000 N. 33

Figure 3-3: The relationship between the load-to-strength ratio **Φ** versus femoral strength for a simulated fall to the side of the hip, adapted from [151]. This relationship indicates that subjects with very low bone strength (<1,500 N) are highly likely to be above the theoretical fracture threshold (red line) but that subjects with slightly higher bone strength values (2,000 – 4,000 N) have a non-zero probability of fracture. For each bin of 500 N (vertical lines), the probability of fracture for bone strengths within that bin was calculated as the ratio of data points below the theoretical fracture threshold to all points in the bin. 36

Figure 3-4: Treatment efficacy. Fracture risk reduction due to varying bone strength mean for the baseline population. Data are presented as mean ± standard deviation for the 10,000 iterations. The red line indicates 41% risk reduction, which was observed clinically. 38

Figure 3-5: Treatment effectiveness. Number of fractures (left) and the absolute effect, or number of fractures prevented (right), with varying baseline bone strength means. Number of

fractures prevented is defined as the number of fractures in the placebo group minus the number of fractures in the treated group. The blue line indicates number of placebo fractures observed clinically (75 fractures) [24]. Data are presented as mean ± standard deviation for 10,000 iterations. 39

Figure 3-6: Risk reduction due to varying net bone strength change between treated and placebo groups. Data are presented as mean ± standard deviation for the 10,000 iterations. The red line indicates 41% risk reduction, which was observed clinically. 39

Figure 3-7: Risk reduction due to varying bone strength change for the treated (left) and placebo (right) groups. All parameters were held constant at reference values (Table 3-1) except the bone strength change, as indicated by the x-axis label. Data are presented as mean ± standard deviation for the 10,000 iterations. The red line indicates 41% risk reduction, which was observed clinically. 40

Figure 3-8: Effect of baseline population eligibility criteria on patient population for a single Monte Carlo iteration. (A) Reference case—baseline population is bounded above 0 N. (B) First eligibility criterion—population is between 1,600 and 3,700 N, equivalent to total hip T-scores between -4.0 to -1.5—an osteoporotic and osteopenic population. (C) Second eligibility criterion—population is between 1,600 and 2,900 N, equivalent to total hip T-scores between -4.0 to -2.5—an osteoporotic population. Red vertical line indicates reference baseline femoral strength mean of 3,000 N. 40

Figure 3-9: Influence of load-to-strength ratio (Φ) on fracture risk reduction (left) and number of fractures (right). The horizonal line represents 50% risk reduction (red line) and number of fractures in placebo group observed clinically [24] (blue line, 75 fractures) for left and right figures, respectively. 44

Figure 3-10: Influence of fall rate (%) on fracture risk reduction (left) and number of fractures (right). Horizonal lines represent clinically observed data for the LOFT trial at 24 months [24]: 41% risk reduction (left, red line) and the number of fractures in the placebo group (right, blue line). 45

List of Tables

Table 1-1: Some proposed physical and chemical characteristics of bone that may influence biomechanical bone quality, categorized by physical scale. Adapted from [51]. 9

Table 2-1: Effect of radiation treatment, sex, and their interaction on microstructural, FEA, and biomechanical testing parameters. Data are shown as mean ± standard deviation. Bold values indicate significant effect ($p < 0.05$) for treatment, sex, and their interaction. 24

Table 2-2: The effect of radiation treatment on the relationship between strength, as measured by either biomechanical testing or finite element analysis (FEA), and selected bone mass and volume parameters. Data pooled for L4 and L5 vertebrae by sex, male ($n = 27$) and female ($n = 25$). Bold values indicate significant effect ($p < 0.05$) for treatment. 25

Table 3-1: Reference study parameters and ranges of any varied parameters. 32

Acknowledgements

There are many people who have supported me and contributed to this work, without whom my graduate school journey would not have been as successful, joyful, and gratifying.

First, to my advisor and mentor, Tony Keaveny: thank you for giving me the opportunity to join your lab and for supporting my wild idea of conducting a small-animal *in vivo* irradiation study without funding. Your encouragement enabled me to conduct research in an area I am truly passionate about, and your willingness to connect me to collaborators made some key aspects of this work possible. I am grateful for your guidance, enthusiasm, insight, and expertise, and feel incredibly fortunate to have had the opportunity to conduct research under your supervision.

I am grateful to Professors Jasmina Vujic, Lisa Pruitt, and Rebecca Abergel for serving on my qualifying exam and dissertation committee. The success of this project and my graduate career is due in no small part to their dedication and willingness to mentor me. In particular, I would like to thank Rebecca for providing the support and framework to conduct a small-animal *in vivo* irradiation study. I appreciate you encouraging me to talk with your students as I tried to navigate my way through writing my first AUP. I am incredibly grateful for your time, expertise, and encouragement.

To my first advisor at Berkeley, Grace O'Connell: thank you for welcoming me into your lab during my first two years as a graduate student. Your willingness to keep my professional development at the forefront—even when it meant recommending I switch to Tony's lab—is admirable and deeply appreciated. I am thankful for my time in your research group and your constant support throughout graduate school.

To my NASA advisor, Josh Alwood: thanks for welcoming me into your lab. I have valued the opportunity you provided me to learn from you and collaborate with all the wonderful people in the Bone and Signaling Laboratory at NASA Ames.

I would like to thank all members of the Berkeley Biomechanics Laboratory, past and present, for making the lab a fun, supportive, and collaborative place to work. I have been surrounded by a plethora of absolute superstars, but I would especially like to thank Megan Pendleton, Saghi Sadoughi, Tongge Wu, and Shiyin Lim. To Megs – thanks a million for being simultaneously the greatest mentor and friend I could have asked for. Your enthusiasm for radiation research and willingness to take me under your wing at NASA have forever changed the trajectory of my career and research. To Saghi – thank you for being my next-desk neighbor for four years, chatting with me every day about research and life in general, and for providing my initial introduction into computational modeling. To Tongge – thank you for your friendship and endless patience, enthusiasm, humor, and expertise. I am eternally grateful that you were willing and able to teach me how to conduct finite element analyses entirely over Zoom. The novelty and insight in Chapter 2 would not have been possible without you! To Shiyin – thank you for your constant support, encouragement, and inspiration throughout the pandemic; our conversations and your friendship have been more important than you realize. I also thank Emily Lindberg, Ben Werbner, Semih Bezci, Noah Bonnheim, Bo Yang, Minhao Zhou, Gabriel Lopez, Audrey Ford, Sofia Arevalo,

Nicole McMindes, Nisha Subramanian, Jonathan McKinley, Ally Gleason, and Sarah Frank for their smiling faces, fun conversations, inspiration, feedback, knowledge, and assistance.

I have had the pleasure of working with an army of undergraduate students, all of whom have challenged me to think analytically about each step of my analysis, and several of whom have been critical in data collection. In particular, I would like to acknowledge Rebecca Bennett and Carina Hernandez for the tremendous amount of work they put into assisting me with the *in vivo* irradiation study, including daily animal health checks and weigh-ins; Jana Quan for development of the base MATLAB code used in Chapter 3; and J'Mya Gray-Martinez for her critical work in image processing. I also thank Chase Swerdlick, Albert Wang, Aditya Goel, Max Sigerman, Matthew Sie, Roshan Toopal, Ryan Louie, Aran Bahl, Rashmi Vidyasagar, Nisha Subramanian, Wan Fung Chui, Robert Wilkerson, and Jason Chang.

This work would not have been possible without support from various sources. First, this study was financially supported by the National Science Foundation Graduate Research Fellowship Program #1752814, and a UC Berkeley Chancellor's Fellowship. Computational resources were made available through the National Science Foundation via XSEDE (Grant TG-MCA00N019). Animals were obtained through the generosity of the Office of Laboratory Animal Care (OLAC) at UC Berkeley; thank you to Christie Ferrecchia, Jennifer Frohlich, Kristen Pincolini, and Monica and Ashley of the Animal Health Team. Thank you to Mike Wendland for training on the XRAD and expertise on small-animal studies; Alex Jordan and Michael Neufer for access to resources in Hesse; Ally Gleason for donating practice tissue; and Mary Bouxsein and Daniel Brooks (Harvard) for access to and training on the microCT.

On a personal note, I would like to thank my support network of friends outside of school. To my East Coast turned West Coast friends who have become family: Linda, Ray, and Pattie—thank you for your constant love and support, wishes of "good day", comic relief, and reminder of life outside of grad school. To my GRCF family: Emily, Cameron, Katrina, Tina, Andy, Ian, Nima, Maura, Celeste, and Patrick—I honestly would not have made it through grad school in one piece without seeing your smiling faces every morning at 5:30 am; thank you for challenging me and bringing so much joy to every day; best wishes, warmest regards. To my CC friends Christina and Arielle—thank you for being the best long-distance friends and for teaching me how to see life more fully. To Haley, Katie, Samantha, Stephanie, Caitlin, and Sarah—thank you for your long-distance cheerleading and constant love; I am so grateful to have had you all by my side for decades.

Finally, I owe endless thanks to my family for their unconditional love and support. To my parents, for providing me with so many opportunities to learn and grow throughout my childhood and inspiring me to never give up; to my sister, for being the best sister, best friend, best supporter, and soon to be fellow PhD in STEM—know that you inspire me every day; my in-laws, for supporting me even when it meant extending time spent on the West Coast significantly longer than originally planned. I owe the largest debt of gratitude to my husband, Matt. Thank you for making California home, and for your steadfast love, patience, selflessness, optimism, joy, motivation, and endless puns. You make each day beautiful and remind me to find the passion in my work when I am getting bogged down in the details. I love you and I like you.

1 Introduction

Bones are remarkable organs that serve both a reservoir function – as a storehouse for essential minerals – and a structural function – providing mobility, support, and protection for the body. Maintaining strong and healthy bones requires a complex and dynamic balance of bone adaptation and remodeling, all modulated by hormones within the body and external loads. However, the structural integrity of bones can be compromised by aging, treatments such as radiation therapy, diseases such as osteoporosis.

Radiation therapy plays a key role in the treatment strategy for more than half of those diagnosed with cancer [1], and has helped lead to an increase in the number of cancer survivors who are now living long enough to experience treatment-related long-term complications. In particular, radiation therapy has been shown to increase the risk of fracture for otherwise healthy bones within the radiation field [2]–[14].

Osteoporosis is one of the most prevalent skeletal diseases in the world. It is characterized by reduced bone mass and associated structural deterioration of bone tissue, which collectively lead to bone fragility and an increased risk of fracture [15]. It is estimated that approximately 50% of women and 13% of men will suffer an osteoporosis-related fracture in their lifetime, with an estimated nine million osteoporotic fractures occurring annually [16]. Regardless of the cause, fractures of the hip in particular are costly and debilitating, with up to 20% mortality in the year following such a fracture [17].

Irrespective of the mechanism of action, modifications to bone strength can influence the risk of fracture. However, the connection between treatment effects on changes in bone strength, and bone strength changes on fracture risk, is not completely understood. First, it is unclear how much treatment-induced changes in bone strength are due to changes in bone mass versus microstructure versus tissue material. In particular, small-animal models of localized irradiation have demonstrated decreases in bone strength that are accompanied by changes in bone structure and composition, suggesting that modifications to both structure and material may contribute to overall reduction in strength following treatment [18]–[22]. However, the exact mechanisms leading to reduced bone strength are unclear, particularly in terms of how much of this weakening effect is due to changes in mass and microstructure versus tissue material. Second, it is unknown why small treatment-induced changes in bone strength are associated with large changes in fracture risk. For example, patients with osteoporosis are treated with a variety of pharmaceutical drugs which have been shown to reduce the incidence of osteoporotic fracture by up to 50% [23]–[25]. However, neither the associated small increase in bone mineral density (BMD) as evaluated by DEXA—about 2-6% [26]—nor the small increase in bone strength—about 2-8% [27]–[30]—appear to fully explain this reported reduction in fracture risk.

Thus, the overall goal of this dissertation was to develop a better understanding of the relative treatment effects on bone strength and to elucidate how small changes in bone strength can be associated with large changes in fracture risk. Together, the work in this dissertation will lead to improved understanding of osteoporosis and radiation treatments and provide new insight into how these treatments influence bone strength and fracture risk.

First, we quantified the relative effects of treatment-induced changes in bone mass, microstructure, and tissue material behavior on bone strength with a unique combination of experimentation and microcomputed tomography-based nonlinear finite element analysis using a murine model of localized irradiation (Chapter 2). Next, we developed a theoretical framework to mechanistically evaluate how changes in bone strength are linked to changes in fracture risk using reported data from osteoporosis treatments (Chapter 3). Together, the resulting insight from these studies can aid in understanding the underlying mechanisms influencing changes in bone strength and their connection to fracture risk, which may help to improve pre-clinical evaluation of therapies and their potential for fracture risk.

The remainder of this chapter will establish a foundation in bone biology, biomechanics, and radiobiology as it relates to the material presented in subsequent chapters of this dissertation.

1.1 Bone

Bone is a specialized connective tissue with a complex hierarchical structure that comprises the skeletal system. The skeleton's primary functions are to provide structural support and protection, maintain mineral homeostasis, produce blood cells, and replace old or microdamaged bone to maintain structural integrity under normal loading conditions. Thus, throughout its life, each bone constantly adapts to changing biomechanical forces, and remodels to replace microdamaged bone with new stronger bone, all in an effort to preserve bone strength or stiffness [31], [32]. In general, bone structure is directly related to these functions.

1.1.1 Composition and Structure[1]

Bone tissue itself is a composite material consisting of organic and inorganic components, as well as a small amount of water. By mass, bone tissue is approximately 60% inorganic, 30% organic, and 10% water. The inorganic phase, which is a form of hydroxyapatite ($Ca_{10}(PO_4)_6(OH)_2$) mineral, gives bone its stiffness and strength. The organic phase, which is comprised of collagen (90% type I) along with non-collagenase proteins, gives bone its ductility and toughness.

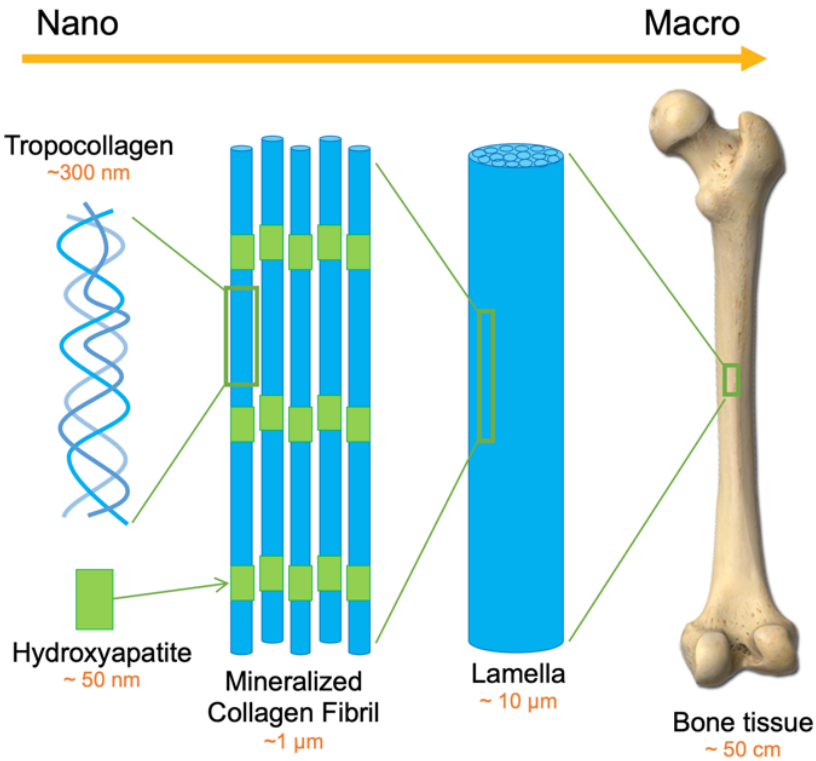


Figure 1-1: Hierarchical structures of bone from the sub-micron length scale to the centimeter length scale. Image adapted from [33].

[1] This section was adapted, in part, from [44], [168]

These constituents of bone are organized in a hierarchical manner (Figure 1-1). At the nanoscale, three collagen molecules are wound into a triple helix structure known as tropocollagen. From there, tropocollagen molecules align in a parallel in quarter-stagger arrangement to make collagen fibrils. Hydroxyapatite mineral crystals adhere to the collagen fibrils, mineralizing them. The mineralized fibrils are then staggered together in layers to make fibers, which are aligned in sheets called lamellae, which can take various forms at the next hierarchical level.

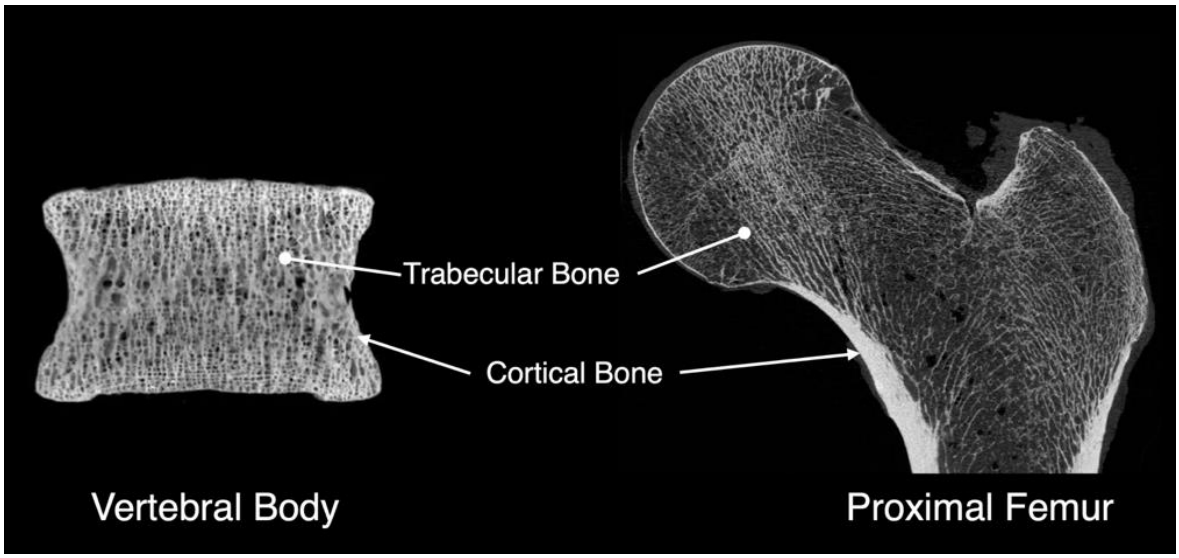


Figure 1-2: Cross-sections of a human vertebral body (left) and proximal femur (right) showing typical arrangements of cortical and trabecular bone. Image adapted from [34].

At its highest hierarchical level, there two types of bone—cortical and trabecular (Figure 1-2). The skeleton is composed of 80% cortical bone and 20% trabecular bone by mass [31]. The primary difference between cortical and trabecular bone is porosity—while the porosity of cortical bone is less than 5-10%, the porosity of trabecular bone is 75-95% [35].

Cortical bone, also called compact bone, is extremely dense. Here, tightly packed lamellae are organized into concentric cylinders in primary lamellar, Haversian, laminar, and woven bone. In general, cortical bone is found in the shafts of long bones and the cortex or shell at the ends of joints and vertebral bodies. It forms the dense outer shell of all bones, providing substantial mechanical strength.

Trabecular bone is an open cell porous network organized in a honeycomb-like structure. In contrast to highly dense and organized cortical bone, in trabecular bone the lamellae are less organized and formed into rods and plates. Trabecular bone is always surrounded by cortical bone, although the thickness of the cortical bone depends on location. Typically, trabecular bone is found near the ends of long bones (such as the femur) and in the interior of irregular bones (such as the vertebral body and pelvis). In trabecular bone, the microstructure is generally aligned in the direction of greatest mechanical stiffness and strength [36]. The trabecular struts support the outer cortical structure, like how the struts of the Eiffel Tower support its outer framework.

Different bones have differing ratios between cortical and trabecular bone. For example, in the femoral head, the ratio is 1:1, while in the radius the ratio is 95:5 [31]. For the purpose of this dissertation, there are several bones of significant interest: the vertebrae, the pelvis, and sacrum. The vertebral body is the load-bearing part of the vertebrae is called the vertebral body. In humans, the vertebral body consists of a central trabecular network surrounded by a cortical shell, with a ratio of 3:1 trabecular to cortical tissue [31], [37]. Similarly, the pelvis and sacrum both mainly consist of trabecular bone surrounded by a thin layer of cortical bone [38]. In contrast, the main shaft of the femur is primarily a thick layer of cortical bone, while the femoral head and neck contain trabecular bone surrounded by a thin layer of cortical bone.

1.1.2 Bone modeling and remodeling

The adaptation, growth, repair, and maintenance of bone are carried out by four main types of bone cells: osteoclasts, osteoblasts, bone lining-cells, and osteocytes. Osteocytes are the most numerous, making up to 90-95% of all bone cells, while osteoclasts and osteoblasts make up only 1-2% and 4-5%, respectively [39], [40].

Bone cells

Osteoclasts are the large multinucleated bone cells responsible for bone resorption [41]. Mature osteoclasts are formed by the fusion of bone marrow precursor cells in the monocyte-macrophage family [31], [42]. Once mature, osteoclasts are found on the surface of the bone mineral, where they dissolve bone mineral in acid [41]. Upon completion of bone resorption, osteoclasts undergo programmed cell death [43]

Osteoblasts are the cells responsible for bone formation. Cuboidal in shape, osteoblasts are mononuclear cells that derive from mesenchymal stem cells [31], [40]. These cells are found in a single layer adjacent to the bone surface [40]. During bone formation, osteoblasts secrete bone matrix protein on the surface of the bone, which is then mineralized [43], [44]. Upon completion of bone formation, some mature osteoblasts remain trapped in the bone as osteocytes, some flatten to cover quiescent surfaces as bone lining cells, and the remainder (approximately 60-80%) die by programmed cell death [40], [43].

Flat bone-lining cells cover 90% of trabecular bone surfaces where no active modeling or remodeling is occurring [40], [44]. Although the specific function of bone-lining cells is not fully understood. They have been shown to prevent osteoclasts from interacting with the bone matrix in locations where bone resorption should not occur [40]. Additionally, recent work suggests bone-lining cells may be a source of osteogenic precursors [43]. Importantly, bone-lining cells may also participate in calcium regulation [43].

Osteocytes are terminally differentiated osteoblasts entombed within the bone matrix after production of new tissue [44]. While not directly involved in bone synthesis or resorption, osteocytes coordinate the response of osteoclasts and osteoblasts to mechanical and chemical cues [43]. Each osteocyte body is located within a lacuna, with cytoplasmic processes extending through canaliculi to neighboring osteocytes through gap junctions [40]. Through this lacunocanalicular system, osteocytes are able to maintain connection with each other and the bone surface, acting as mechanosensors and stimulating bone adaptation to daily forces [31], [40]. In

this way, osteocytes are thought to initiate bone modeling and remodeling, although the mechanisms by which these cells convert mechanical stimuli to biochemical signals are not well known [40].

Bone adaptation

The main functions of bone remodeling are its role in adaptation to changing biomechanical forces to preserve bone strength or stiffness as well as mineral homeostasis [31], [32], [45]. First, remodeling allows bone to alter its shape, size, and/or matrix properties in response to mechanical stimulation [46]. By adapting to their mechanical environment, bones are able to produce structures that are optimized for their function [44]. This concept is described by Wolff's law, which postulated that bone shape and architecture is altered to accommodate the mechanical loads it experiences. Additionally, the skeleton contains nearly all of the body's calcium and resorption of bone mineral is crucial for maintaining extracellular levels of calcium in order to maintain life [47].

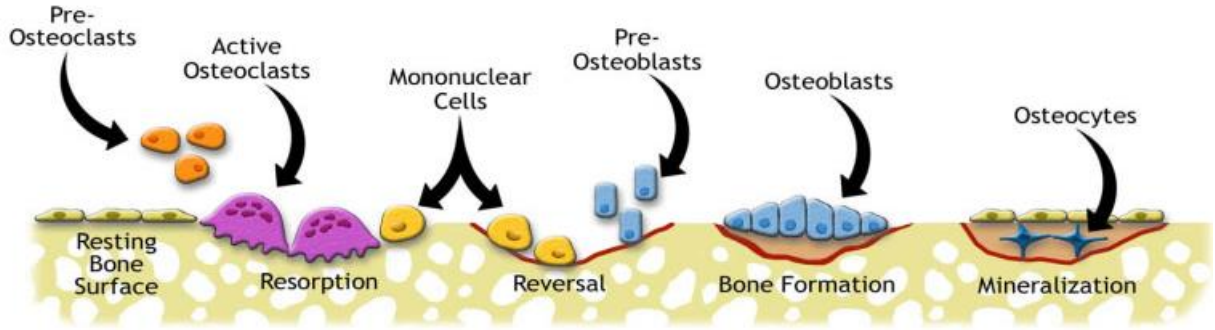


Figure 1-3: A representation of the bone remodeling process, shown in two dimensions. Image adapted from [48].

Regardless of the goal of remodeling, it is achieved by the coordinated action of osteoclasts and osteoblasts, and follows a cycle of four sequential phases: activation, resorption, reversal, and formation [31] (Figure 1-3). First, during activation, osteoclast precursors are differentiated into mature osteoclasts. Next, bone-lining cells retract from the surface and osteoclasts dissolve the bone mineral, creating resorption pits [43]. The resorption phase takes approximately two to four weeks to complete [31]. Then, during the reversal phase, osteoclast resorption ceases and bone formation begins [31], [43]. Finally, osteoblasts form new bone by filling in the resorption pits created by osteoclasts with a protein matrix called osteoid, which is comprised mostly of type I collagen [31], [40]. This osteoid is a template for inorganic hydroxyapatite crystals, which are incorporated into the collagen matrix [49]. At any given time, there are thousands of remodeling cycles taking place throughout the body, with each cycle taking approximately 4-6 months to complete [49].

Importantly, the rate and balance of bone remodeling vary throughout life. During adolescence, bone remodeling occurs at a very high rate. With advanced age (80+ years), remodeling rates in both men and women begin to decline [49]. Additionally, the balance of tissue resorbed and formed is not always equivalent. In a healthy adult, the balance is usually slightly negative [49]. However,

abnormal increases in osteoclast activity can result in excessive bone resorption and conditions such as osteoporosis [41].

There are some differences in bone turnover between cortical and trabecular tissue. In a healthy adult, cortical bone will turnover 2-3% annually, likely to maintain adequate biomechanical strength [31]. In contrast, the rate of trabecular bone is much higher at around 15-20% per year, indicating that trabecular bone turnover may be more critical for calcium homeostasis [31]. Further, there is more bone remodeling on the free surfaces of trabecular rods/plates than on the internal surfaces of Haversian canals in cortical bone. Thus, trabecular bone is slightly less mineralized than cortical bone [44].

1.1.3 Mechanical behavior of bone

While a healthy skeleton plays a critical role in structural load bearing, its function can be compromised by aging, disease, or treatment. Diseases such as osteoporosis and treatments such as cancer radiation therapy are characterized by deterioration of bone tissue, resulting in increased bone fragility and risk of fracture. Fractures negatively impact quality of life and can lead to early mortality: patients are more than twice as likely to die following a fracture [50].

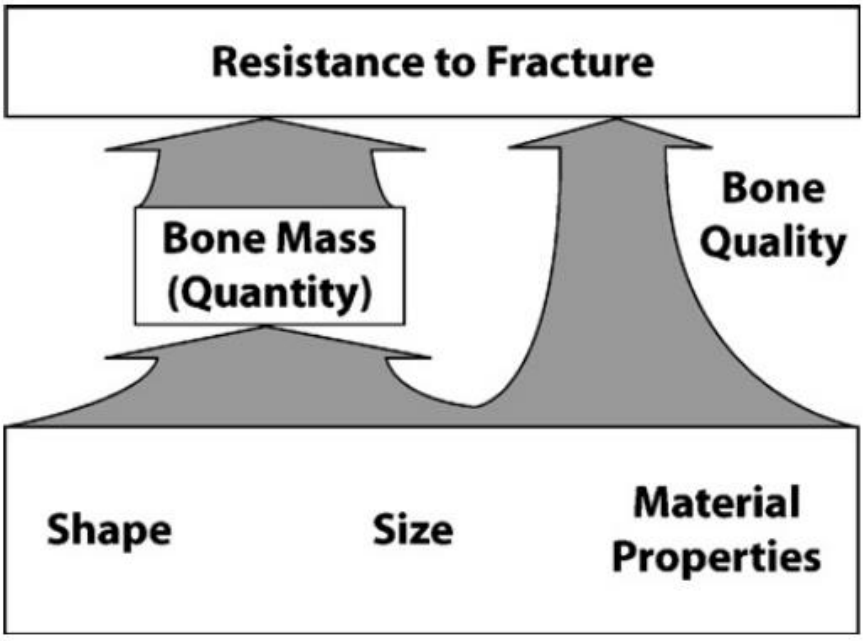


Figure 1-4: Schematic showing the role of bone quality in whole bone strength (i.e., resistance to fracture). Factors that contribute to bone strength/fracture resistance but are not explained by measures of bone mass/quantity are bone quality effects. Image adapted from [51]

In general, the ability of bone to resist fracture is determined by a combination of factors, namely bone quantity and quality (Figure 1-4). Measures of bone quantity, such as bone mass, bone volume fraction, and bone mineral density, have been shown to be strong predictors of bone strength [52]–[56]. However, these bone quantity measures do not fully explain all variations in bone strength. Thus, factors that contribute to bone strength but are not accounted for in bone

quantity measures are considered to be bone quality factors (Figure 1-5). Bone quality factors include the spatial distribution of bone mass (i.e. shape and microarchitecture), and tissue material properties [46], [51] (Figure 1-4).

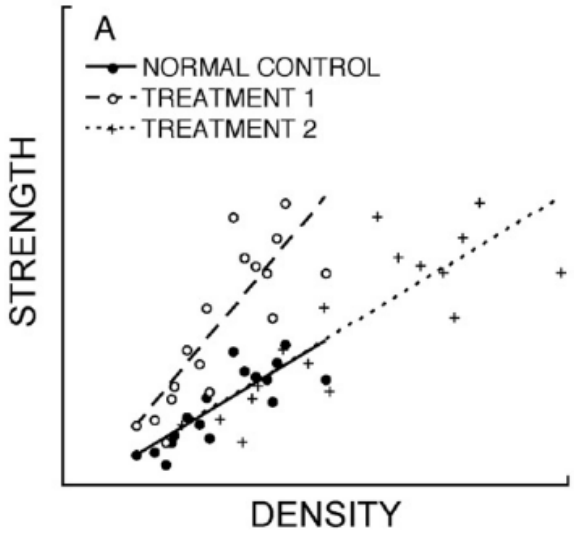


Figure 1-5: Hypothetical strength-density relationships for normal bone and bone from two different treatment groups. Both treatment groups show the same increase in bone strength. However, the relationship between the bone strength and density in bone exposed to Treatment 1 has an increased slope, indicating improved bone quality. In contrast, bone exposed to Treatment 2 shows a similar relationship between bone strength and density as compared to the control group, suggested that strength effects are due to bone quantity, not quality, effects. Adapted from [51].

The mechanical behavior of bone is qualitatively similar for cortical and trabecular bone. For both, the stiffness and strength depend on the direction of loading due to their anisotropic microstructure. Specifically, both types of bone are stronger in compression than tension. However, cortical bone is considered transversely isotropic; it is stronger and stiffer when loaded in the longitudinal direction compared to the radial or circumferential directions. In contrast, trabecular bone's anisotropy is based on the main trabecular orientation rather than the general anatomic direction. While in some skeletal sites the anatomic direction coincides with the main trabecular orientation (i.e. vertebrae), in most sites this is not the case (i.e. the proximal femur) [44].

Proper quantification of both strength as well as bone quantity and quality factors are critical in evaluating the effect of aging, disease, and treatment on bone fragility or risk of fracture [8]–[13], [57]–[59]. As previously discussed, bone is a highly heterogenous material, and many bone characteristics that may influence bone strength at all hierarchical levels – from the molecular to the whole bone – have been proposed as potentially key bone quality factors (Table 1-1). Importantly, any clinically relevant modification to bone quantity that changes bone biomechanical performance relative to its bone mass and leads to a fracture is a clinical concern [51]. A great deal of research has been generated to explore the possibility of bone quality changes to gain a better understanding of the mechanisms through which radiation or osteoporosis drugs treatment may increase fracture risk beyond decreasing bone density. Thus, a goal of this dissertation is to examine if differences in bone quality influence bone mechanical behavior in ways that are not accounted by bone mass following treatment. To assess bone biomechanical

performance, the mechanical properties of bone can be quantified via *ex vivo* laboratory testing or high-resolution finite element modeling.

Table 1-1: Some proposed physical and chemical characteristics of bone that may influence biomechanical bone quality, categorized by physical scale. Adapted from [51].

Scale (m)	Bone characteristics
$>10^{-3}$	•Whole bone morphology (size and shape) •Bone density spatial distribution
10^{-6}–10^{-3}	•Microarchitecture •Porosity •Cortical shell thickness •Lacunar number/morphology •Remodeling cavity number, size, and distribution
10^{-9}–10^{-6}	•Mineral and collagen distribution/alignment •Microdamage type, amount, and distribution
$<10^{-9}$	•Collagen structure and cross-linking •Mineral type and crystal alignment •Collagen–mineral interfaces

Biomechanical characterization of bone

There biomechanical characterization of bone material properties via experimental benchtop testing has been widely utilized via numerous types of assays. A common indicator of bone fragility is overall bone strength. Bone strength is defined as the biomechanical threshold where fracture occurs [51], [60]. In the laboratory, strength is evaluated as failure under a single load, where a bone (or a portion of a bone) is loaded in a manner most similar to its *in vivo* loading – axial (tension or compression), shear, torsion, or bending [35], [61] (Figure 1-6). For all loading modes, when a monotonically increasing load is applied until failure, deformations are produced throughout the structure, and the resulting deformation is recorded as a function of the applied load [35], [62] (Figure 1-6). The strength of the bone is then defined as either the ultimate load or load at failure, while the stiffness of the bone is defined as the slope of the load-deformation curve before yielding [35], [61]. Additionally, the work or energy required to yield or fracture a bone, is quantified as the area under the load-deformation curve [61]. Comparisons can then be made to evaluate the effect of aging, disease, or treatment on these measured properties.

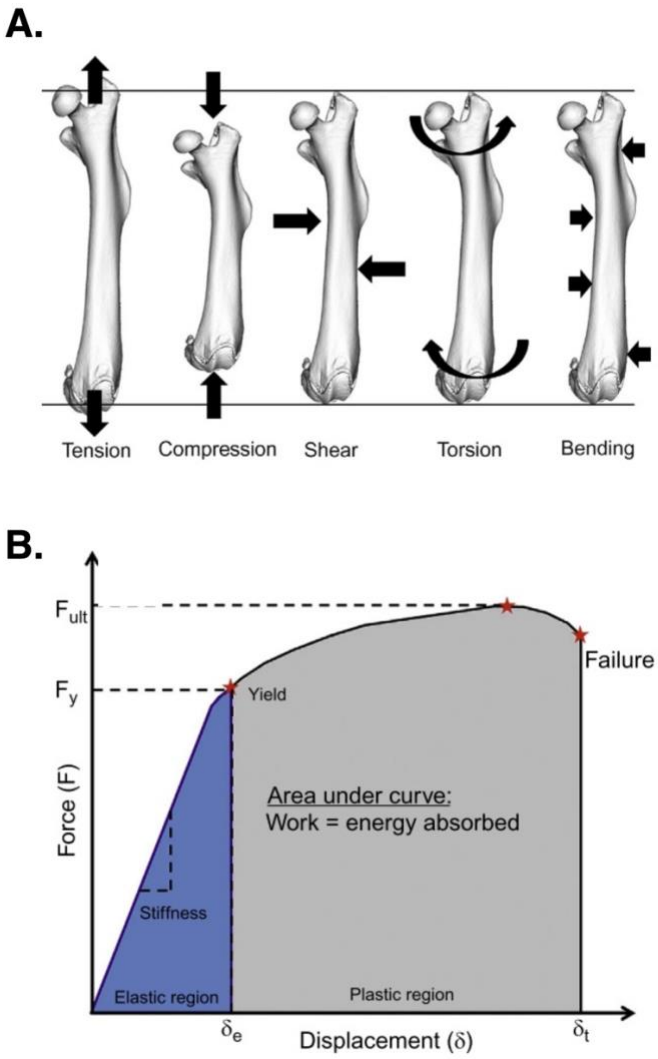


Figure 1-6: (A) Mechanical testing modes in bone. When the ends of the bone are pulled apart or pushed together, the bone is under axial tension and compression, respectively. In contrast, if load is applied across the bone, shear is induced. If the ends of the bone are twisted relative to one another, the bone is under torsion. Bones can also be loaded in bending, with load and support applied perpendicular to the long axis. Figure adapted from [61]*. (B) Load-displacement behavior for a whole bone structural test. Many important characteristics can be determined by analyzing this curve, including the strength, stiffness, deformation, and energy dissipation. The stiffness is determined from the slope of the initial linear region, where F is load and* $\boldsymbol{\delta}$ *is displacement. The strength is the load required to fail the whole bone, or the ultimate load during a compressive axial test. Work can be calculated as the area under the curve; work/energy can be calculated for the area under the curve until yield, ultimate load, or failure. Image adapted from* [61]*.*

High-resolution finite element modeling of bone

In addition to biomechanical testing, another powerful tool for investigating bone mechanical behavior is finite element modeling. When applied to bone, researchers build high-resolution models of specimens based on micro-computed tomography (microCT) images. First, each voxel in the images is converted into an eight-noded brick element [63], explicitly capturing bone structure. Then, each element is assigned isotropic homogeneous material properties to provide tissue-normalized outcomes. Finally, to replicate biomechanical testing, these models are virtually

loaded. Finite element modeling provides detailed insight into the micromechanics of the bone and its failure mechanisms. Furthermore, it allows researchers to separate the effects of bone structural changes from the effects of material property changes [64], [65]. Importantly, finite element models have correlated well with biomechanical measures of apparent-level mechanical properties, providing some validation for this method [63], [65]–[67]

Finite element modeling requires significant resources, including both state-of-the-art software and hardware. The work in this dissertation utilized a highly-scalable, implicit finite element framework [68], [69] implemented on some of the world's fastest and most advanced parallel supercomputers. Specifically, this work utilized implementations of Olympus on a Dell cluster with 1,736 48-core Intel Xeon Platinum 8160 ("Skylake") processors (Stampede2; Texas Advanced Computing Center, The University of Texas at Austin, Austin, Texas, USA).

Finite element modeling allows researchers to characterize bone biomechanics in ways that have several advantages over traditional biomechanical tests. First, finite element modeling is non-destructive, enabling detailed evaluation of the effects of loading conditions or material properties on bone biomechanical behavior via parameter studies [70]–[72]. Second, while biomechanical testing provides only apparent-level mechanical behavior, finite element modeling is able to provide detailed insight into stress and strain distributions within the bone in order to determine failure mechanisms [64], [67], [73]. Importantly, finite element modeling can be used in combination with biomechanical testing in order to leverage the strengths of each method. Using this combined approach, previous studies have gained significant insight into failure mechanisms and mechanical properties [63], [65]–[67], [73].

1.2 Radiation, radiobiology, and radiation therapy

Nearly 40% of men and women in the United States will be diagnosed with cancer at some point during their lifetimes [2], and more than half of those diagnosed will be treated with ionizing radiation therapy. In radiation therapy, radiation is delivered localized to the area of cancerous tissue from a variety of different sources in order to eradicate the tumor.

Radiation is generated by radioactive atoms or a radiation generating source and can be either nonionizing or ionizing. Nonionizing radiation has insufficient energy to eject electrons from an atom. In contrast, ionizing radiation has enough energy to ionize atoms or molecules by detaching an electron from them. Thus, ionizing radiation is the only type of radiation that can cause biological damage and thus used to destroy cancer cells. Ionizing radiation therapy is a critical component of cancer treatment: half of all cancer patients will receive radiation therapy during the course of their illness [74].

There are two ways to deliver ionizing radiation to a cancerous tumor: external and internal radiation. Internal radiation (also called brachytherapy) is delivered from inside of the patient's body via radioactive sources [74]. In contrast, external beam radiation is delivered from outside of the patient's body; high-energy beams of radiation are targeted to the location of the tumor [74], [75]. External radiation is the most common clinical approach, and thus the focus of this dissertation.

The primary type of external ionizing radiation utilized for cancer treatment are photon beams, or forms of electromagnetic radiation such as X-rays and gamma-rays [74]. X-rays are generated by devices such as linear accelerators while gamma-rays are generated by the decay of radioactive material, such as cobalt-60. Regardless of the type of electromagnetic radiation, these sparsely ionizing radiations are routinely used to penetrate deeply into tissue. For example, high-energy megavoltage X-rays are frequently utilized in pelvic radiation therapy [76].

1.2.1 Radiobiology: the biological damage of radiation

The study of the effect of ionizing radiation on biological systems, or radiobiology, has existed for nearly as long as human beings have been aware of its existence. The first observation of ionizing radiation was recorded in 1895, with the observation of X-rays [75], [77], and within a few years, the first recorded effect of ionizing radiation on the biological systems was observed via a skin burn to a researcher [75].

There are several factors to take into account when considering the effect of radiation on tissue. First, radiation exposure is most often expressed as absorbed dose, defined as the amount of energy absorbed per unit mass of material. Dose is expressed with the SI of Gray (Gy), where one Gy is equal to one Joule per kilogram (J/kg). Second, the degree of biological damage can vary depending on the type (quality) of radiation. Thus, a dose equivalent is calculated using a pre-defined quality factor to incorporate the type of radiation. In this case, Sievert (Sv) is the SI unit for dose equivalent. Because the quality factor for X-rays is equal to 1, 1 Gy of X-rays is equal to 1 Sv.

As the field of radiobiology has expanded, it has become well understood that the health effects of ionizing radiation result primarily from damage to DNA. Damage to DNA can occur directly by radiation or indirectly through radiation-generated reactive oxygen species generated by the ionization of water molecules (Figure 1-7). Direct effects are produced by the initial action of the radiation itself to biologically important molecules; a strand break in DNA caused by ionization of the molecule itself is one example [75], [77]. In contrast, indirect effects are caused by the later chemical action of free radicals or other radiation products; an OH free radical following the radiolysis of the water in the body's tissues causing a strand break in DNA or the crosslinking of two proteins are two examples [75], [77].

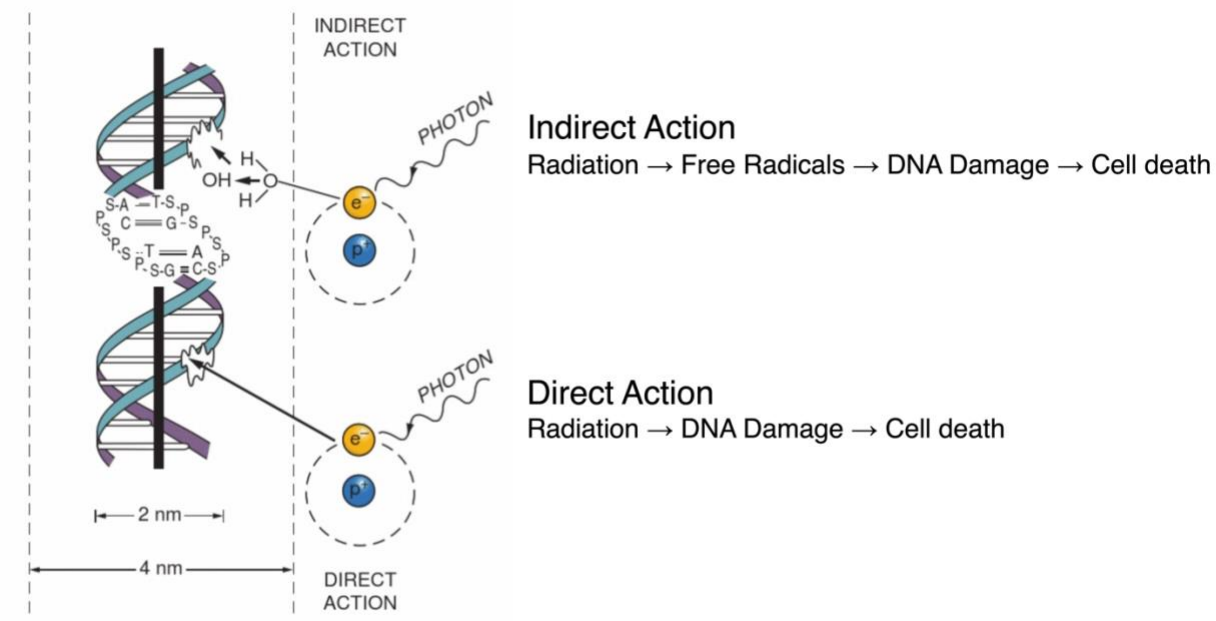


Figure 1-7: Direct and indirect actions of radiation. The structure of DNA is shown schematically. In indirect action, the secondary electron interacts with a water molecule to produce a free radical (e.g., hydroxyl radical, OH), which in turn produces the damage to the DNA. In direct action, a secondary electron resulting from absorption of an X-ray interacts with the DNA to produce an effect. S, sugar; P, phosphorus; A, adenine; T, thymine; G, guanine; C, cytosine. Image adapted from [75].

1.2.2 Radiation therapy for cancer treatment

Cells and DNA have a remarkable ability to repair damage caused by radiation, although inevitably some cells will be damaged irreparably or fail to propagate correctly, ultimately leading to cell death. With this in mind, cancer treatment via radiation requires a balance between targeting cells intended to die (i.e., cancerous cells) and minimizing damage to surrounding healthy tissues. This balance is achieved with careful treatment planning with dose fractionation and targeted treatment.

Dose fractionation

The most advantageous treatment results are obtained when radiation is delivered to a patient in fractions [75]. Unfortunately, cancerous cells and healthy cells have comparable resistance to radiation-induced death [77]. However, the method of fractionation of the radiation dose over a period of weeks produces better tumor control for a given level of healthy tissue toxicity than a single large dose given all at once [75], [77]. Currently, fractionated external beam radiation therapy is the most common type of radiation therapy used for cancer treatment [74], [76]. As the name implies, a dose of radiation is divided into multiple "fractions". This practice is designed to maximize the destruction of cancerous cells while minimizing damage to healthy, noncancerous tissue.

The efficacy of fractionation is based on four factors, known as the "four Rs" of radiobiology: repair, reassortment of cells within the cell cycle, repopulation, and reoxygenation [75], [77]. Dividing a dose of radiation into smaller fractions allows adequate time for healthy tissues to repair sublethal damage between fractions and cellular repopulation. At the same time, cancerous cells subject to the same dose fractionation scheme will result in increased damage to the tumor due to

the reoxygenation and reassortment of cells into radiosensitive phases of the cell cycle between dose fractions [75]. Thus, a fractionated radiation therapy protocol is optimized for healthy-tissue sparing and increased tumor-cell killing.

Current fractionation regimens are based on a linear-quadratic formula, which gives the time-dose factors for individual tumor types (early responding tissues) and normal tissues (late-responding tissues). This linear-quadratic model is used to calculate the biologically effective dose (BED). Most simply put, BED is equivalent to the total dose multiplied by its relative effectiveness. BED can be calculated as follows:

$$BED = (nd) \times \left(1 + \frac{d}{\alpha/\beta}\right)$$

where n is the number of fractions of dose [Gy] d, and the ratio α/β is the dose at which the linear and quadratic components of cell killing are equal [Gy]. The ratio of α/β is often assumed to be 10 Gy for early-responding tissues (i.e. cancer cells) and 3 Gy for late-responding tissues (i.e. nontumor tissue) [75].

A typical radiation therapy regimen now consists of daily fractions (Monday through Friday) of 1.5 to 3 Gy given over the course of several weeks [74]. For example, a typical pelvic radiation therapy treatment regimen is 25 fractions (n) of 1.8 Gy (d), for a total of 45 Gy to the tumor (α/β = 10 Gy). Of this dose, surrounding bone can receive as much as half of each fraction. Thus, BED to bone (α/β = 3 Gy) during clinical treatment is ~ 30 Gy.

Targeted treatment

As previously stated, the goal of radiation therapy is to deliver as much radiation dose to the tumor as possible while sparing surrounding noncancerous tissue. Technological advances outside of fractionation have helped achieve this through new imaging modalities, powerful computer-aided planning programs, and enhanced linear accelerators.

Traditional treatment planning begins with computed tomography (CT) imaging, which allows for accurate tumor localization for optimal radiation beam placement and healthy tissue shielding [74]. To mitigate toxicity to noncancerous tissues, computer and imaging treatment plans are generated to target the cancerous volume in three dimensions (3D).

With intensity modulated radiation therapy (IMRT), multiple radiation beams of varying intensity are conformed to the 3D shape of the targeted tumor by multi-leaf collimators. In use for decades, IMRT has been shown to successfully irradiate the targeted tumor and have considerable sparing of healthy tissues [78], [79].

Image guided radiation therapy (IGRT) has built on this approach by integrating imaging from 3D computed tomography (CT) just prior to treatment to verify patient position [76]. To further improve the effectiveness of IGRT, oncologists are hoping to incorporate additional imaging modalities, such as magnetic resonance imaging (MRI) or positron emission

tomography/computed tomography (PET/CT), to improve target delineation and clinical outcomes [80], [81].

1.2.3 Increased fracture risk following clinical radiation therapy

Notwithstanding the technological advances, radiation exposure to healthy tissues remains a challenge. Incidental irradiation causing secondary effects with potential long-term complications on patient health are increasingly a priority as cancer survivorship increases [3].

A common long-term complication of radiation therapy is an increased risk of fracture [8]–[13] occurring in otherwise healthy bones within the radiation treatment field [4]–[6], [14]. At directly irradiated sites, insufficiency (or fragility) fractures occur as a result of normal stress applied to weakened bone [4], [14], [82], [83]. For example, external beam radiation therapy for pelvic and abdominal cancers is known to increase the risk of fracture in the pelvis, hip, and vertebrae [4], [6], [10], [11], [13], [84]–[95], but not the risk of fractures on bones outside of the radiation field [4]. A recent meta-analysis found that one in seven gynecologic cancer patients treated with radiation develops a pelvic fracture [96]. This elevated risk of fracture is of substantial clinical concern as these types of fractures can result in substantial loss of independence, increased morbidity, and potentially diminished ability to heal, leading to a 20% greater expected mortality rate after 5 years [4], [11], [82], [88], [97]–[100].

The observed increased risk of fracture is presumably due to a radiation-induced reduction in bone strength, although the exact mechanisms leading to reduced bone strength are unclear. Specifically, it is unclear what element of the bone that is affected by treatment—mass, microstructure, or material—most affects the changes in bone strength. While one possible mechanism is radiation-induced reduction in bone mass, there are limited data, and clinical studies to date have not conclusively demonstrated a correlation between irradiation and decreased bone mass [8], [101]–[103]. Other possible mechanisms include alterations to bone quality factors which contribute to bone strength but are not accounted for in bone mass measures, including bone microstructure and tissue material properties [46], [51].

1.3 Effect of radiation therapy and osteoporosis drug therapy on bone

1.3.1 Response of bone to radiation

Although the rate of post-therapy fractures is well documented, mature bone is classified as a radioresistant material by the ICRP [104]. For this reason, the pathophysiology of the effects of radiation treatment on bone is not well understood. However, recent animal and cell studies have helped to identify mechanisms leading to radiation-induced fractures [105].

Research conducted *in vitro* demonstrates radiation effects on osteoblasts. Following irradiation, bone-forming osteoblasts are reduced in number and activity [106]. Ultimately, this is due to a decrease in osteoblast proliferation and differentiation, cell-cycle arrest, increased terminal differentiation [107]–[110]. Such effects on osteoblasts suggest that bone formation may be reduced, potentially contributing to radiation toxicity in bone.

Animal models have provided further insight into the pathophysiology of radiation-induced bone damage due to localized exposure. To date, the most direct assessment of radiation damage to bone

strength comes from murine models. For example, mouse model of hindlimb irradiation has demonstrated that therapeutic radiation can result in a loss of femoral trabecular architecture, deterioration of organic matrix mechanics, diminished bone strength and fracture toughness without the loss of bone mass [18], [20]–[22], [111]–[113]. Additionally, this same model has shown to decrease osteoblast activity, increase to osteoclast activity, alter the collagen alignment, damage the bone matrix, and increase development of non-enzymatic collagen crosslinks such as advanced glycation end products (AGEs) [18], [106], [113]–[117]. Similarly, a rat model of hindlimb irradiation demonstrated that fractionated doses of irradiation resulted in a decrease in ultimate strength, again without the loss of bone mass [118].

1.3.2 Response of bone to osteoporosis drug therapies

Osteoporosis results from an imbalance between bone resorption and bone formation. When the rate of resorption exceeds the rate of formation, as in the case of osteoporosis, there is a gradual thinning of trabeculae and the cortex. To prevent excessive bone loss, many osteoporosis therapies act by altering this balance of resorption and formation.

There are numerous pharmaceutical agents approved for the treatment of osteoporosis, which can be classified into two basic categories: antiresorptive agents and anabolic agents. These two classes of agents influence the two opposing sides of the bone remodeling process. Antiresorptive agents limit the activity of bone-resorbing osteoclasts, thereby preventing further bone loss [119]. However, the connection between bone formation and resorption are closely tied—by limiting osteoclast activity the rate of new bone formation by osteoblasts is also reduced. In effect, antiresorptive agents seek to form new bone in locations that have previously undergone resorption and then maintain bone mass and prevent further bone loss over time. In contrast, anabolic agents stimulate osteoblast recruitment to increase new bone formation without reducing the rate of resorption in order to increase bone mass [119]. Anabolic agents work by stimulating new bone formation not only on remodeling surfaces, but also on quiescent bone surface that is not undergoing remodeling [120]. Regardless of the agent utilized, osteoporosis pharmaceutical agents have been shown to reduce the incidence of vertebral and hip osteoporotic fracture by about 40-70% [23]–[25], [121]–[124]. However, the associated small changes in areal BMD [24]–[26], [121] and bone strength [27]–[30]—on the order of 2-8%—are unable to adequately explain this large reduction in fracture risk.

Addressing this, the objective of the current study is to investigate the discrepancy between the small bone strength changes and large fracture rate changes through two different treatments – radiation therapy and osteoporosis. Regardless of the treatment, these studies will improve understanding of how small changes in bone strength can be associated with large changes in fracture risk and provide new insight into how best to treat to reduce fracture risk, including patient selection.

1.4 Objective and Scope

The overall goal of this dissertation was to better understand the relationship between treatment on bone strength changes, and bone strength changes on fracture risk through two treatments – radiation therapy and osteoporosis treatments. Apart from the basic science understanding of the mechanisms through which treatment, bone strength, and fracture risk are connected for radiation

therapy and osteoporosis treatments, these studies will provide insight into methods in evaluating treatment efficacy.

The first study presented (Chapter 2), investigates the connection between radiation therapy and bone strength changes. We quantified the relative effects of treatment-induced changes in bone mass, microstructure, and tissue material behavior on bone strength with a unique combination of experimentation and microcomputed tomography-based nonlinear finite element analysis. In addition to providing insight into radiation treatment specifically, this study also provides a framework for characterizing the effects of other treatments and diseases on biomechanical bone quality and the relative contribution of factors leading to altered bone strength.

In Chapter 3, the connection between small treatment-induced changes in bone strength on clinical fracture risk were investigated. Using published data on osteoporotic drug therapies as our model, we developed a theoretical framework to mechanistically evaluate how changes in bone strength are linked to changes in risk of hip fracture risk following osteoporosis treatments. Importantly, this model will improve understanding of how small changes in bone strength can be associated with large changes in fracture risk and provide new insight into how best to treat to reduce fracture risk, including patient selection. Ultimately, this model can be applied to bone strength changes due to radiation therapy, providing a mechanistic understanding of increased fracture risk in cancer patients.

The final chapter provides concluding remarks and suggests future directions for this research. Together, these studies provide insight which can aid in understanding the underlying mechanisms influencing changes in bone strength and their connection to fracture risk. The primary novelty of this work provides a treatment evaluation model (biomechanical testing and high-resolution microCT-based finite element modeling) as well as a theoretical framework which may help to improve pre-clinical evaluation of therapies and their potential for fracture

2 Relative Effects of Radiation-Induced Changes in Bone Mass, Microstructure, and Tissue Material Behavior on Vertebral Strength in a Rat Model

2.1 Introduction

Nearly 40% of men and women in the United States will be diagnosed with cancer at some point during their lifetimes [2]. More than half of those diagnosed with cancer will be treated with ionizing radiation therapy [1], where external beams of ionizing radiation in the form of X-rays or gamma rays are localized to the area of cancerous tissue in order to eradicate the tumor [75]. Treatments such as radiation therapy are effective, and have led to an increase in the number of cancer survivors who are now living long enough to experience treatment-related long-term complications [2], [3], [7].

A common long-term complication of radiation therapy is an increased risk of fracture [8]–[13] occurring in otherwise healthy bones within the radiation treatment field [4]–[6], [14]. For example, external beam radiation therapy for pelvic and abdominal cancers is known to increase the risk of fracture in the pelvis, hip, and vertebrae [4], [6], [10], [11], [13], [84]–[95], but not the risk of fractures on bones outside of the radiation field [4]. In fact, a recent meta-analysis found that one in every seven patients with gynecologic cancer treated with radiation therapy develop a pelvic fracture [96]. This elevated risk of fracture is of substantial clinical concern, as these types of fractures can result in substantial loss of independence, increased morbidity, and potentially diminished ability to heal, leading to a 20% greater expected mortality rate after five years [97], [98].

The observed increased risk of fracture is presumably due to a radiation-induced reduction in bone strength, although the exact mechanisms are unclear. While one possible mechanism is radiation-induced reduction in bone mass, there are limited data, and clinical studies to date have not conclusively demonstrated a correlation between irradiation and decreased bone mass [8], [101]–[103]. Other possible mechanisms include alterations to bone quality factors which contribute to bone strength but are not accounted for in bone mass measures, including bone microstructure and tissue material properties [46], [51].

To investigate how localized irradiation alters bone mass, quality, and mechanical integrity, pre-clinical murine models have been widely utilized. These small-animal models have been shown to replicate human pathologic responses to radiation therapy, including trabecular bone resorption and diminished mechanical integrity [20]–[22], [111], [113], [118]. Specifically, models of mouse hindlimb irradiation have demonstrated decreases in bone strength (femoral diaphyseal bending strength and fracture toughness; femoral axial compressive strength) accompanied by changes to both bone structure (decreased trabecular bone volume fraction, decreased connectivity density, increased trabecular spacing) and composition (increased nonenzymatic collagen crosslinks, changes to the mineral to matrix ratio) [18]–[22]. Collectively, these studies suggest that modifications to both bone structure and tissue material properties may contribute to overall reduction bone mechanical performance following irradiation. However, the exact mechanisms leading to reduced bone strength are unclear, particularly in terms of how much of this weakening

effect is due to changes in mass and microstructure versus tissue material. Additionally, these models of hindlimb irradiation expose a larger percentage of the mouse's body to irradiation than occurs in clinical radiation therapy.

Addressing these issues, the overall goal of this study was to quantify irradiation-induced changes in rat vertebral bone strength and assess the distinct contribution of altered bone structure and material properties. First, we investigated if localized irradiation to the lumbar spine in a rat model could exhibit decreased bone strength following irradiation. Second, using a unique combination of experimental testing and finite element analysis (FEA), we quantified the effect of localized irradiation on rat vertebral body strength due to alterations in structure and tissue material properties. In particular, we assessed the nature of the relation between FEA and experimentally measured strength, and whether or not that relation depended on treatment. A sub-objective of this study was to determine if sex has a significant influence on bone's response to irradiation.

2.2 Methods

2.2.1 Study design and specimens

Understanding if irradiation treatment effects vertebral bone material properties require observing how bone strength changes following treatment while accounting for any structural (i.e., bone mass or microstructural) changes. This is difficult to achieve through biomechanical testing alone, so we coupled biomechanical tests with high-resolution, microCT based finite element analysis. This unique combination allowed us to separate out the effect of mass and microstructural changes from material changes and quantify their contribution to overall treatment effect on strength.

All experiments were approved in advance by the Institutional Animal Care and Use Committee at the University of California, Berkeley. Animals were randomly assigned to treatment groups. Throughout the study, animals were maintained in community housing and supplied with water and chow *ad libitum*.

Twenty-seven skeletally mature Sprague-Dawley rats at 17 weeks of age were randomly assigned to one of two groups: treated (n = 7 for each female and male) or sham (n = 6 female, n = 7 male). The treated group were subject to 10 fractions of 3 Gy given one fraction per day, 5 days per week, for an overall treatment time of 2 weeks (10 F × 3 Gy/2 weeks) (see Appendix 6.2.1 for details). The biologically effective dose (BED) for this fractionation scheme bone is 60 Gy, calculated using the following equation:

$$BED = (nd) \times \left(1 + \frac{d}{\alpha/\beta}\right)$$

where n is the number of fractions (n = 10) of dose d per fraction (d = 3 Gy), and the ratio α/β is 3 Gy for bone, which is considered a late-responding tissue (i.e. nontumor) [75]. This BED is within the dose limit (< 74 Gy) used clinically for pelvic malignancies [125]. Radiation was delivered from a collimated X-ray source (320 kV beam at 17 mA, 3.7mm Cu beam filter, X-RAD 320, Precision X-Ray, North Branford, CT, USA), which focused the beam on the lumbar spine (surface area ~8-18 cm^2, dependent on animal size; Figure 2-1). Rats were anesthetized with

isoflurane gas and positioned under a lead shield. Sham-irradiated animals were subjected to the same treatment protocol (handling, anesthesia, recovery) excluding actual irradiation. For the duration of the experiment, animals were weighed daily; body mass did not significantly differ between irradiated and sham groups at any time point (data not shown). All animals were euthanized using CO_2 asphyxiation 12 weeks following treatment. All experiments and analyses were performed blinded to treatment code.

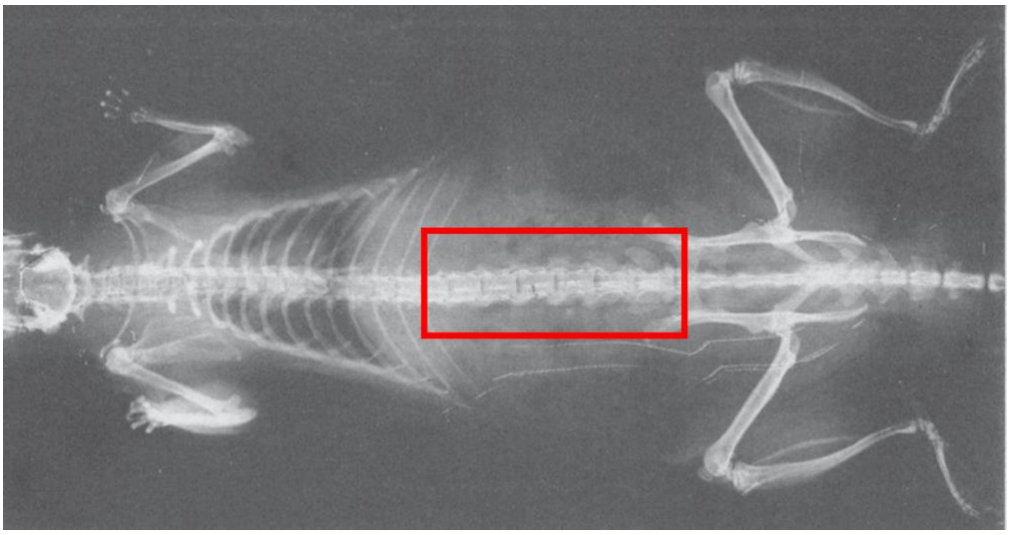


Figure 2-1: Dorsal view of rat with target treatment area in red; image adapted from [167]

2.2.2 Specimen preparation and micro-CT imaging

After humane sacrifice, both the L4 and L5 lumbar vertebrae were excised, gently cleaned of soft tissue, wrapped in saline-soaked gauze, and stored at -20°C (see Appendix 6.2.2). After removing intervertebral discs and soft tissue, the posterior elements and endplates were removed, following a specialized protocol similar to those used in other experimental and finite element studies [71], [126], [127] (see Appendix 6.2.3). Briefly, each vertebra was aligned inside a 3D printed disposable jig with alignment pin, and the posterior elements were secured with polymethylmethacrylate (PMMA) (Figure 2-2A). The combined jig-bone construct was then used to mount the vertebra in a custom holder of a diamond blade precision saw (IsoMet 1000, Buehler, Lake Bluff, IL, USA). Under constant irrigation, two parallel cuts were made to remove the cranial and caudal endplates such that the mid-50% of the original height remained. The vertebral body was removed from the jig and isolated using bone clippers (Figure 2-2B). To confirm surfaces were plano-parallel, vertebral body height was measured with calipers four times at 90° intervals; the percent variation in specimen height was required to be within 1.5% of mean height. Only one sample was rejected.

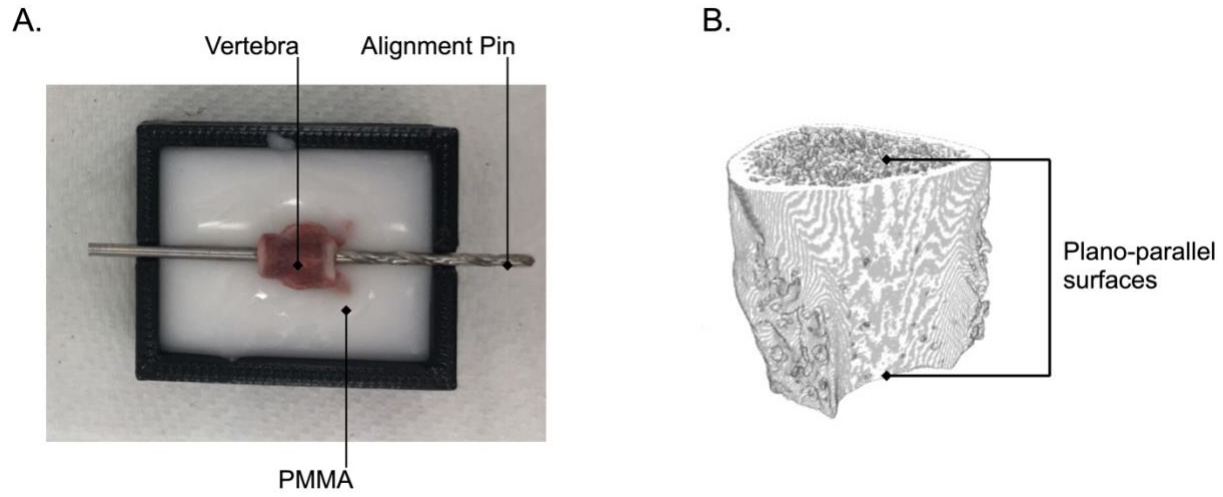


Figure 2-2: Specimen preparation. A. Vertebral body inside 3D printed disposable jig with alignment pin. Posterior elements are secured in polymethylmethacrylate (PMMA). B. MicroCT image of prepared vertebral body with plano-parallel surfaces.

Next, all prepared specimens were imaged using quantitative microCT (μCT 40, Scanco Medical AG, Wangen-Brüttisellen, Switzerland) using an isotropic voxel size of 15μm (70 kVp, 114 μA, 300 ms integration time) to characterize cortical and trabecular microstructure and to create image datasets for subsequent finite element analysis (see Appendix 6.2.4). A global threshold of 500 mgHA/cm^3 was applied, and tissue mineral density (TMD) was quantified. Additionally, the manufacturer's software was used to compute various microstructural indices: bone height, bone mineral density (BMD), trabecular bone volume (Tb.BV), trabecular bone volume fraction (Tb.BV/TV), trabecular number (Tb.N), trabecular separation (Tb.Sp), trabecular thickness (Tb.Th), structure model index (SMI), connectivity density (Conn.D), bone volume in the cortical (Ct.BV), trabecular (Tb.BV) and integral (BV) compartments, and integral bone volume fraction (BV/TV) [128]. The average bone cross-sectional area (CSA) of the vertebral body was calculated by dividing BV by the slice thickness multiplied by the bone height (i.e., BV/(15μm × height)). Bone mineral content (BMC) was estimated based on measured bone volume and the assumption of a constant tissue density of 2.05 g/cm^3 [129] (i.e., BV × 2.05 g/cm^3).

2.2.3 Biomechanical testing

After imaging, the specimens were mechanically compressed to failure via uniaxial compression to measure vertebral strength, stiffness, and energy-to-failure using an established testing protocol [54], [71], [73], [126], [127] (see Appendix 6.2.9). Briefly, the vertebral bodies were placed on the center of the bottom platen of a servohydraulic load frame (858 Mini-Bionix, MTS, Eden Prairie, MN, USA). To ensure the top platen rested flat on the vertebral body during loading, we used a spherically seated platen on a lubricated ball-bearing. Once preloaded to ~10 N, the set screws on the upper platen locked the ball-bearing in place. To minimize any effects of machine compliance, apparent strain was measured using a 25 mm gage length extensometer (632.11F-20, MTS, Eden Prairie, MN, USA) attached directly to the platens. Tests included five preconditioning cycles to 0.3% strain followed by a final ramp to 8% strain at a rate of 0.5% strain/sec. Strength was defined as the peak load on the resulting force-deformation curve (i.e., failure). Stiffness was defined as

the slope of the force-displacement curve prior to failure. Energy-to-failure was quantified as the area under the force-displacement curve until the peak load.

2.2.4 Nonlinear finite element analysis

Finite element models were built from the binary microCT images of each vertebral body by converting each voxel into an 8-noded brick element (15 μm element size; [130]) (see Appendices 6.2.5 and 6.2.6). To provide tissue-normalized outcomes regardless of treatment, all bone finite elements in each model were assigned the same homogeneous isotropic tissue material properties: elastic modulus of 19.7 GPa, Poisson's ratio of 0.3, and tissue-level compressive and tensile yield strains of 0.81% and 0.33%, respectively [67], [73], [131]. To simulate the experimental compression testing, each model was subjected to uniaxial compressive loading to 2% apparent strain, using fixed boundary conditions (see Appendix 6.2.7). Depending on bone size, models contained three to eight million elements. All nonlinear analyses were solved using a highly scalable, implicit parallel finite-element framework—Olympus [68], [69]—running on a Dell Linux Cluster supercomputer (Stampede2, Texas Advanced Computing Center).

A vertebral-level yield strength (in Newtons) was defined from the overall force-strain curve as the force defined from a 0.2% strain-offset criterion, and is henceforth referred to as the FEA strength [67]; apparent yield strain was calculated as the displacement at this force divided by the original specimen height. Stiffness was calculated as the initial slope of the force-displacement curve. Finally, the finite element-predicted stiffness was calibrated to the biomechanically measured vertebral stiffness to provide an averaged measure of tissue modulus for each vertebra, called the effective tissue modulus [63], [131]. (Details on post-processing can be found in Appendix 6.2.8.)

2.2.5 Statistical analyses

Each outcome—vertebral strength from mechanical testing and FEA, bone volume and microstructure from the microCT analysis—was compared for treatment and sex effects, as well as their interaction, by ANOVA. For any parameter with a significant effect of treatment or the interaction factor, percent differences in measurements were calculated between sham and irradiated specimens for each sex. Final data for all parameters consisted of 52 total vertebrae, with 12-14 samples (L4 and L5 vertebrae) in each group.

We used linear-least squares regression to separate bone mass, microstructure, and tissue material effects. First, to separate bone mass and microstructure effects from tissue material effects, we directly compared strength for individual specimens as measured by FEA (predictor; all specimens with identical material properties), versus biomechanical test (outcome). Next, to separate bone mass effects from microstructure effects, we directly compared bone mineral content (BMC; predictor) versus biomechanical strength (outcome). All statistical analyses were performed using JMP (SAS Institute, Inc., Cary, NC, USA), where $p \leq 0.05$ was defined as significant.

2.3 Results

2.3.1 MicroCT analysis

While measurements of trabecular and integral bone structure were diminished by irradiation, cortical bone volume and tissue mineral density were not. There were significant reductions in bone mass and volume following radiation treatment for both sexes. In the trabecular compartment, treatment resulted in lower Tb.BV/TV (-32%), and Tb.BV (-29%) (Table 2-1, Figure 2-3). Overall, integral BV/TV, BV, and BMC were lower by 18% in the irradiated group compared to the sham group ($p < 0.001$ for all, Table 2-1). In contrast, Ct.BV was not significantly lower for irradiated animals ($p = 0.07$). Further, neither Tb.TMD nor integral TMD were altered by treatment ($p = 0.21$ and $p = 0.28$, respectively, Table 2-1).

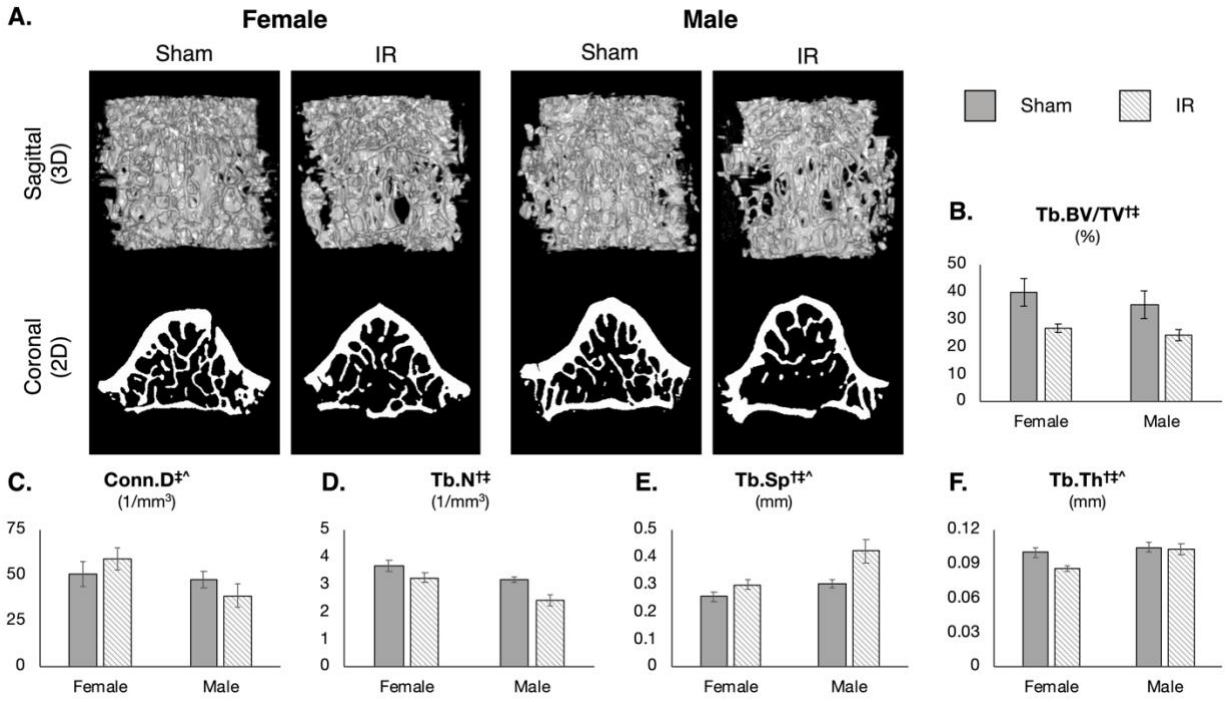


Figure 2-3: Effect of radiation treatment, sex, and their interaction on trabecular microarchitecture parameters. Data are shown as mean ± 95% confidence interval. Superscripts show significant effect ($p < 0.05$) for treatment†, sex‡, and their interaction^.

While the radiation-induced changes in bone volume did not depend on sex, the changes in microarchitecture did (Table 2-1). Following radiation, the trabeculae were fewer in number, lower in thickness, and greater in separation, with the magnitude of the treatment effect depending on sex. Specifically, Tb.Sp was altered by treatment to a greater extent in males than females (+40% versus +17%, respectively), while Tb.Th was reduced more in females than males (-14% versus -2%, respectively) (Table 2-1). For these parameters, the direction of change was consistent for both sexes. In contrast, the direction of change to trabecular Conn.D depended on sex ($p < 0.01$)—increasing (+17%) in females and decreasing (-19%) in males (Table 2-1, Figure 2-3).

Table 2-1: Effect of radiation treatment, sex, and their interaction on microstructural, FEA, and biomechanical testing parameters. Data are shown as mean ± standard deviation. Bold values indicate significant effect ($p < 0.05$) for treatment, sex, and their interaction.

	ANOVA			Female			Male		
	Treatment	**Sex**	**Interact**	**Sham**	**Irradiated**	**% diff.**	**Sham**	**Irradiated**	**% diff.**
Microstructure - Trabecular									
Tb.CSA (mm^2)	**0.000**	**0.000**	0.787	1.77 ± 0.31	1.26 ± 0.22	-28.6%	1.97 ± 0.23	1.42 ± 0.29	-27.7%
Tb.BV (mm3)	**0.000**	**0.000**	0.226	6.02 ± 1.22	4.37 ± 0.78	-27.5%	8.21 ± 1.02	5.80 ± 1.33	-29.4%
Tb.BV/TV (%)	**0.000**	**0.001**	0.394	39.83 ± 4.89	26.79 ± 2.81	-32.7%	35.15 ± 3.74	23.91 ± 3.48	-32.0%
Tb.Conn.D ($1/mm^3$)	0.894	**0.000**	**0.005**	50.63 ± 12.32	59.08 ± 11.04	16.7%	47.68 ± 8.47	38.42 ± 11.82	-19.4%
Tb.SMI	**0.000**	**0.000**	0.221	-0.94 ± 0.57	0.69 ± 0.30	-173.6%	-0.36 ± 0.44	0.98 ± 0.31	-376.6%
Tb.N (1/mm)	**0.000**	**0.000**	0.062	3.67 ± 0.33	3.23 ± 0.33	-11.9%	3.16 ± 0.23	2.38 ± 0.38	-24.6%
Tb.Th (mm)	**0.001**	**0.000**	**0.006**	0.100 ± 0.008	0.086 ± 0.004	-14.0%	0.104 ± 0.009	0.103 ± 0.009	-1.7%
Tb.Sp (mm)	**0.000**	**0.000**	**0.005**	0.25 ± 0.03	0.30 ± 0.03	17.1%	0.30 ± 0.03	0.42 ± 0.08	39.7%
Tb.BMD ($mgHA/cm^3$)	**0.000**	**0.002**	0.930	465 ± 40	341 ± 35	-26.7%	431 ± 37	308 ± 39	-28.4%
Tb.TMD ($mgHA/cm^3$)	0.207	**0.018**	0.207	962 ± 14	954 ± 11	-	950 ± 12	950 ± 9	-
Microstructure - Cortical									
Ct.BV (mm3)	0.066	**0.000**	0.376	9.90 ± 2.35	9.22 ± 1.37	-	16.05 ± 3.08	14.12 ± 2.80	-
Ct.CSA (mm^2)	0.056	**0.000**	0.675	2.83 ± 0.60	2.58 ± 0.33	-	3.82 ± 0.72	3.44 ± 0.57	-
Microstructure - Integral									
CSA (mm^2)	**0.000**	**0.000**	0.620	4.60 ± 0.66	3.85 ± 0.40	-16.3%	5.79 ± 0.80	4.86 ± 0.56	-16.0%
BV (mm^3)	**0.000**	**0.000**	0.208	15.93 ± 2.94	13.58 ± 1.69	-14.7%	24.26 ± 3.44	19.92 ± 2.86	-17.9%
BV/TV (%)	**0.000**	0.070	0.862	58.21 ± 4.37	47.85 ± 2.88	-17.8%	56.09 ± 4.40	46.10 ± 3.12	-17.8%
BMD ($mgHA/cm^3$)	**0.000**	0.134	0.699	650 ± 39	547 ± 36	-15.8%	638 ± 45	526 ± 35	-17.5%
TMD ($mgHA/cm^3$)	0.280	0.114	0.101	1064 ± 11	1066 ± 19	-	1064 ± 13	1054 ± 10	-
BMC (mg)	**0.000**	**0.000**	0.208	32.65 ± 6.02	27.84 ± 3.46	-14.7%	49.74 ± 7.04	40.84 ± 5.86	-17.9%
Height (mm)	0.923	**0.000**	0.254	3.66 ± 0.17	3.72 ± 0.16	-	4.42 ± 0.20	4.35 ± 0.26	-

2.3.2 Biomechanical testing and finite element analyses

For both sexes, irradiation treatment had a substantial and consistent negative effect on vertebral strength, as measured by biomechanical testing. Compared to the sham-irradiated group, vertebral strength was 27% lower ($p < 0.0001$, Table 2-1) for the irradiated group, with an average reduction in of 117 N. This trend was consistent in both female and male animals. As expected, vertebral strength was associated with both bone mass and volume. The relationship between biomechanical strength and bone mass and volume parameters was consistent for both sexes. Specifically, cortical and integral bone volume were most strongly associated with strength for (adjusted $R^2 = 0.71$ and 0.72 for female; adjusted $R^2 = 0.79$ and 0.86 for male, respectively; Table 2-2).

Table 2-2: The effect of radiation treatment on the relationship between strength, as measured by either biomechanical testing or finite element analysis (FEA), and selected bone mass and volume parameters. Data pooled for L4 and L5 vertebrae by sex, male (n = 27) and female (n = 25). Bold values indicate significant effect (p < 0.05) for treatment.

	Female		Male	
	Adj. R^2	Treatment	Adj. R^2	Treatment
Trabecular				
Tb.BV (mm^3)	0.45	0.058	0.53	**0.036**
Tb.BV/TV (%)	0.50	0.917	0.56	0.410
Tb.BMD ($mgHA/cm^3$)	0.50	0.948	0.55	0.411
Cortical				
Ct.BV (mm^3)	0.71	**0.000**	0.79	**0.000**
Integral				
BV (mm^3)	0.72	**0.009**	0.86	**0.006**
BV/TV (%)	0.51	0.729	0.59	0.288
BMD ($mgHA/cm^3$)	0.50	0.625	0.59	0.361

While treatment had a substantial negative effect on vertebral strength, it was quantified differently by biomechanical testing and FEA. As previously mentioned, vertebral strength as measured by mechanical testing was 27% lower ($p < 0.0001$, Table 2-1) for the irradiated group. In contrast, compared to the sham group, vertebral strength as measured by FEA was 20% lower for the irradiated group ($p < 0.001$, Table 2-1).

Importantly, while vertebral strength measured by FEA was highly correlated (adjusted $R^2 = 0.86$) with strength measured by biomechanical testing, the relationship between these two strength measurements depended on treatment ($p < 0.05$; Figure 2-4). In the general linear regression model ($n = 52$) of biomechanical strength as a function of FEA strength, treatment, and their interaction, the term for treatment was significant both before ($p \leq 0.02$) and after ($p \leq 0.03$) removing the non-significant ($p = 0.29$) interaction term.

The significant effect of treatment on this relationship indicates that irradiation altered some biomechanical feature that was not contained in the FEA models, namely some aspect of the bone tissue material properties since they were assumed to be the same in all FEA models. The vertical offset of lines in Figure 2-4 quantified this effect in terms of vertebral strength (by biomechanical

testing). Those data indicate a treatment effect on material properties that altered overall vertebral strength by 27.6 N, which represents 23.6% of the observed average reduction of 117 N in vertebral strength.

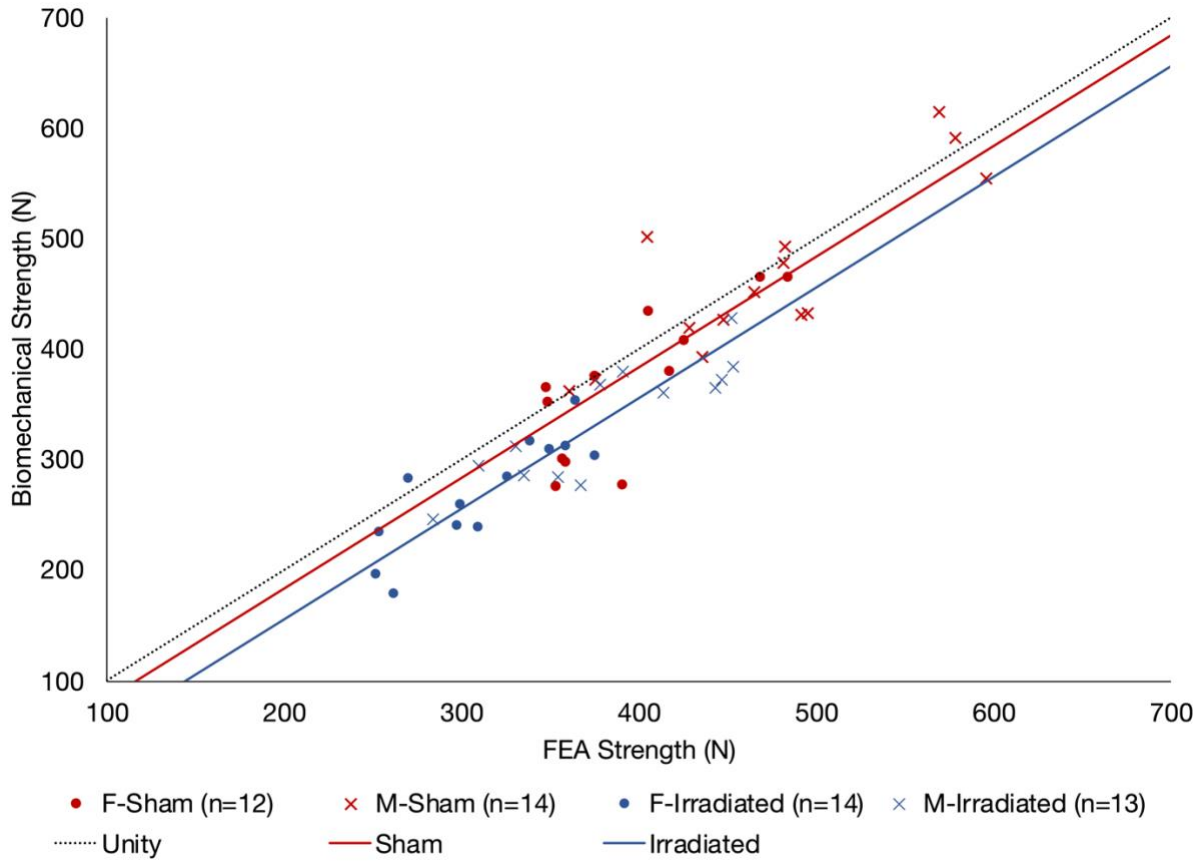


Figure 2-4: Vertebral strength (in newtons [N]) for experimental biomechanical testing versus FEA, color-coded by treatment group. General linear least-squares regression (adjusted R^2 = 0.86; all data pooled), showing the treatment effect in this relationship; the term for treatment was significant before ($p \leq 0.02$) and after ($p \leq 0.03$) removing the non-significant interaction term. The vertical offset of lines indicates a treatment effect on material properties that altered overall vertebral strength by 27.6 N, or 7.6% of the average value. For reference, the dashed line shows the line of unity (Y=X).

Similarly, BMC was highly correlated (adjusted R^2 = 0.82) with strength measured by biomechanical testing, the relationship between these two strength measurements depended on treatment ($p < 0.05$). In the general linear regression model (n = 52) of biomechanical strength as a function of BMC, treatment, and their interaction, the term for treatment was significant both before ($p < 0.0001$) and after ($p < 0.0001$) removing the non-significant ($p = 0.57$) interaction term. Here, the significant effect of treatment on this relationship indicates that irradiation altered bone mass (i.e., BMC) independently of bone microstructure, quantified in terms of vertebral strength (by biomechanical testing). The effect of treatment on BMC altered overall vertebral strength by 71.1 N, which represents 60.8% of the observed average reduction of 117 N in vertebral strength.

2.4 Discussion

In this rat model of localized irradiation, changes in material accounted for 24% of the overall observed biomechanical effect, while changes in mass and microstructure together accounted for about 76% of the observed reduction in vertebral strength (61% and 16%, respectively). To separate bone mass and structure effects from tissue material effects, we directly compared strength for individual specimens as measured by FEA versus biomechanical test using linear least-squares regression. Importantly, the relationship between these measures of strength was significantly altered by treatment, suggesting the reduction in bone strength was altered by a factor that was not contained in our FEA models. While FEA and biomechanical evaluation both accounted for bone mass and structure (i.e., internal spatial distribution of bone mass), each FEA model was assigned identical tissue material properties to provide tissue-normalized outcomes regardless of treatment. Therefore, the treatment effect on the biomechanical-FEA strength relationship is attributed to a treatment-induced alteration to some aspect of tissue material properties. The vertical offset of the lines of best fit in Figure 2-4 quantified this material effect to be a consistent 27.6 N, representing 23.6% of the observed average reduction in vertebral strength (117 N). Thus, in weaker specimens (i.e., irradiated specimens), the relative effect is greater due to significant alterations in trabecular microstructure following treatment. By quantifying the treatment effect on overall bone strength changes, out results provide new insight into the adverse effects of irradiation on bone biomechanics, and for the first time quantify the relative contribution of mass, structure, and material on overall bone strength, albeit for the rat vertebral body.

Our findings are consistent with other published studies and for the first time directly quantify the contribution of tissue material changes to whole bone strength following irradiation treatment. Consistent with our rat model, mouse models have shown a reduction in bone mass, architecture, and strength [20]–[22], [125]. For example, a mouse hindlimb fractionated irradiation model (4F × 5 Gy) with a similar BED to the current study (55.7 Gy) exhibited reduced bone mass via diminished femoral diaphyseal area and cortical thickness, as well as decreased femoral bending strength and fracture toughness [20], [22]. Importantly, these studies demonstrated that radiation can reduce strength by diminishing bone material properties, such as decreased fracture toughness [22] and flexural strength [20], independent of changes to bone mass and structure. Further, these same mouse hindlimb irradiation models have quantified alterations in bone composition, such as increased collagen crosslinks and matrix/mineral alignment [115], [116], decreased mineral to matrix ratio [19], [22], [114] and crystallinity [114], as well as a reduction in collagen energy-to-failure [18] at 12 weeks following treatment, which could influence bone material properties. While the aforementioned studies measured material changes in cortical bone, others have characterized similar material effects in the trabecular-rich distal femur [21].

If the observed material effect is present clinically, there are several implications. First, although our model suggests the overall biomechanical effect of radiation is dominated by mass and microarchitecture, comparatively small material alterations can account for nearly a quarter of the observed 27% change in bone strength, or about 6% of the overall mean strength. Relatively small changes in bone strength in the same order of magnitude (2-8%) due to osteoporosis therapies are associated with large changes in fracture risk [23]–[25], [27]–[30]. While it is not clear from clinical data if fracture risk is altered linearly with change in bone strength, our model in Chapter 3 suggests that bone strength changes of the observed magnitude (6%) can significantly alter

fracture risk (~40%). Thus, if a similar change in bone strength due to treatment-induced material changes is present with clinical radiation, it may help to explain the increased fracture risk for patients undergoing radiation therapy despite the inconclusive correlation between irradiation and decreased bone mass [8], [101]–[103]. Second, our results emphasize the need for a more complete assessment of the efficacy of countermeasures to prevent bone loss due to treatment. Evaluation of treatments, including anti-resorptive drugs [132]–[136], strength training [137], and diet [138], should include assessment of both structural and material changes on biomechanical strength; the quantification of bone morphology and mechanical behavior following irradiation is not sufficient on its own.

The inclusion of both male and female rats provided new insight into sex-specific effects of radiation treatment, namely to bone microarchitecture. Despite the differential treatment effect on trabecular thickness, separation, and connectivity for male and female rats ($p < 0.01$ for all), the overall biomechanical effect on strength did not depend on sex (p=0.35). While this may seem counterintuitive, the concept of structural redundancy may provide some insight. Structural redundancy is the ability of a structure to retain its function even if some parts of the structure fail. In this way, overall strength is maintained via multiple redundant load paths where loads can be redistributed to parts of the structure that have not yet failed. In bone tissue, structural redundancy has been demonstrated in trabecular-rich human vertebrae [73] and may be present in murine tissue as well. Thus, despite sex differences in microarchitecture, the overall redundancy of the trabecular structure may maintain overall strength by offsetting the specific microarchitectural changes from differentially impacting bulk failure. However, while male vertebrae are consistently larger than female vertebrae across murine and human spines, bone morphology and strength differ between male and female mice [139] and rats. Thus, a direct comparison between sexes may be limited. This highlights a need for future investigations to identify sex- mechanisms for these observed effects and proposed means of interventions

There are several limitations to this study that should be considered when interpreting our results. First, we do not expect the absolute effect reported for this murine model to translate directly to humans due to differences in human-murine dosing, physiology, bone remodeling processes, and vertebral bone shape, size, and microstructure. Notwithstanding, this work provides new insight into the mechanisms leading to reduced strength and provides motivation for experiments on humans. Second, the observed material effect could be due any number of biochemical and compositional changes, including alterations to collagen structure, tissue mineralization, or mineral-collagen interactions. While the characterization of potential material compositional changes at the molecular level was beyond the scope of this study, others have demonstrated compositional changes and alterations to the bone organic matrix in irradiated cortical bone in murine models [18], [19], [22], [114], [115]. Further investigation into the treatment effect on bone composition and their connection to reductions in bone strength remain potential topic of future research. Additionally, our results are limited in that they only give insight into a single point in time following treatment (12 weeks). Although out of the scope of this project, time post-irradiation has been shown to be a key variable in the severity of loss of bone strength following treatment [20]. However, the 12-week endpoint after final radiation treatment was chosen to mimic clinical fracture rates approximately 1 year following treatment. As rodents have a metabolic rate that is four to six times higher than that of humans [140], [141], the 12-week post irradiation

interval would be comparable to a follow-up period of approximately 1-1.5 years, within the range of median time to fracture observed clinically (7.1 to 19 months following treatment) [96].

As our FE models and associated mineral density measures are based on measurements taken using microCT, there are inherent resolution issues that must be considered when interpreting our results. First, the voxel size of the microCT scans was 15μm, and the resulting TMD and BMD measurements that may not reflect irradiation-induced changes that could occur at smaller scales, including within mineral crystals themselves [114], [116]. However, our microCT-based FEA strength is highly correlated with the experimental results, suggesting the current resolution is indeed adequate to capture volume fracture and architecture. Second, we observed no alterations to integral or Tb.TMD with radiation treatment (p = 0.28 and p = 0.21, respectively). While consistent with clinical observations that bone mineral density does not change following radiation therapy, it is possible that changes to tissue mineralization were not well captured by microCT. Previous work has demonstrated that measurements of mineral density via microCT are well correlated with but underestimate measures of mineral density via synchrotron microCT and ash density [142], [143].

Despite these limitations, we have presented a useful evaluation tool in any application where the effects of mass, microstructure, and material on bone strength are at play, including aging, disease, or pre-clinical evaluation of therapies. The combination of experimental and finite element analysis provides a systemic approach for characterizing biomechanical behavior from treatments. This evaluation tool takes advantage of relatively common analyses, including microCT imaging and biomechanical testing, and supplements it with previously validated high-resolution finite element methodology. This contrasts with more frequently utilized evaluation tools, which measure bone characteristics in isolation from other factors, resulting in a potentially incomplete understanding of treatment effects. The combined usage of experimental and FE analyses provides a systemic approach for integrating treatment effects at all scales and enables measurement of treatment effects that cannot be quantified by a single method. This method of evaluation has been utilized before, where changes due to aging and anti-resorptive drug treatment have been shown to be driven by changes to mass and microstructure, not tissue material [65], [73]. Importantly, this method could be utilized further in other applications, and may provide new insight into other bone-altering treatments and diseases, specifically in animal models or cadaver studies where it is possible to combine microCT and mechanical testing— for example, on bone biopsies or cadaver tissue from radiation therapy patients.

In summary, the current study quantified the relative contribution of radiation-induced changes to mass and structure versus tissue material on bone strength. Importantly, while the overall reduction in strength was dominated by changes to bone mass and structure (76%), the effect of radiation treatment on tissue material was significant and measurable (24%). Although in a small animal model, our results may have clinical implications if material changes are influencing bone strength to a similar magnitude in radiation therapy patients. Further, our evaluation tool, a combination of experimental and finite element analyses, could be utilized to quantify the relative contributions to bone strength in applications beyond radiation treatment, including aging, disease, and drug therapies. Taken together, the current work expands our understanding of the radiosensitivity of bone tissue and emphasizes the complex nature of bone strength loss following exposure to radiation.

3 Theoretical Effects of Treatment-Induced Changes in Bone Strength on Fracture Risk Reduction in Post-Menopausal Women

3.1 Introduction

While radiation therapy plays a key role in the treatment strategy for more than half of those diagnosed with cancer [1], this treatment has been shown to increase the risk of fracture for otherwise healthy bones within the radiation field [2]–[14], presumably due to changes in bone strength. However, the connection between treatment on changes in bone strength and the subsequent change to fracture risk is not well characterized, and no studies to date have quantified the clinical effects of radiation therapy on bone strength. Although there are limited data available for radiation therapy in particular, other treatments, such as antiresorptive drugs for osteoporosis, are much better characterized. For both radiation therapy and antiresorptive drug treatments, the exact mechanisms leading to an altered risk of fracture following osteoporotic drug treatments are unclear. Thus, osteoporosis treatment data on bone strength and fracture risk can provide a framework to gain insight into how changes in bone strength from treatment are related to fracture risk.

Osteoporosis is an asymptomatic skeletal disease affecting millions of people worldwide characterized by low bone density, poor bone quality, and reduced bone strength. For those affected by osteoporosis, the risk of fracture is substantial: 50% of women and 20% of men over the age of 50 will suffer from an osteoporosis-related fracture during their lifetime [144] leading to decreased quality of life and increased morbidity and mortality [145]. Despite a decline in fracture rates from 2007 to 2013, recent trends indicate that fracture rates are no longer declining [57]. Thus, with the size of the elderly population continuing to increase [146], the already high burden of osteoporotic fractures [17], [147] remains a serious public health problem.

While osteoporosis therapeutic treatments alendronate, denosumab, risedronate, zoledronic acid, and odanacatib have been shown to reduce the incidence of hip fracture in the relatively narrow range of 40-50% [23]–[25], [121], [122], [148], the underlying biophysical mechanisms are not well understood. In particular, compared to such a large treatment effect on fracture risk, the associated increase in bone mineral density (BMD) as evaluated by DEXA is small across these various treatments, in the range of 2-6% [24]–[26], [121], as is the estimated change in bone strength from finite element analysis, in the range of 2-8% [27]–[30]. Numerous studies have sought to provide an explanation for this enigma. In a meta-analysis of data from multiple clinical trials, changes in BMD were significantly associated with reduction in fracture risk [149]. However, the relation was weak, particularly for hip fracture prediction, and lacked any mechanistic basis. Addressing mechanisms, other studies have sought provide a mechanistic explanation through stress raisers [150] or changes to bone strength [151]. To date these theories have not been supported by clinical or animal studies. For example, it has been theorized that the suppression of resorption cavities with osteoporosis therapies may improve bone strength by reducing stress risers, but previous studies have produced inconsistent results without strong evidence of stress risers disproportionately effecting strength [152]–[154]. Further, Keaveny and Bouxsein [151] presented the conceptual implications of the existence of a biomechanical fracture

threshold above which a bone will fracture, theorizing that treatment-induced changes in bone strength may move patients below the threshold and prevent fracture. However, the authors did not apply this concept to evaluate fracture risk in clinical cohorts with changing bone strengths. Thus, this fundamental issue remains unexplained despite millions of patients being treated for hip fractures annually.

We sought to mechanistically explain how small changes in bone strength, as observed in clinical trials, can lead to the large observed changes in fracture risk using a biomechanical approach as applied to reported clinical trial data. Our theoretical analysis also provides insight into how best to treat to reduce fracture risk, including patient selection.

3.2 Methods

The basis for this study is a mechanistic Monte Carlo-based prediction of bone fracture as applied to reported clinical trial data for an antiresorptive drug treatment. These reported clinical data—including baseline bone strength and strength change with treatment—were used to calculate the reduction in the risk of fracture using a custom MATLAB (MathWorks, Natick, Massachusetts) program. Following a Monte-Carlo approach, each step (as shown in Figure 3-1) was repeated 10,000 times to generate an overall mean outcome (relative risk of fracture) and standard deviation. Details of each step are explained below. See Figure 3-1 for an overview of this process and Table 3-1 for the reference study characteristics and description of parameters, some of which were varied parametrically.

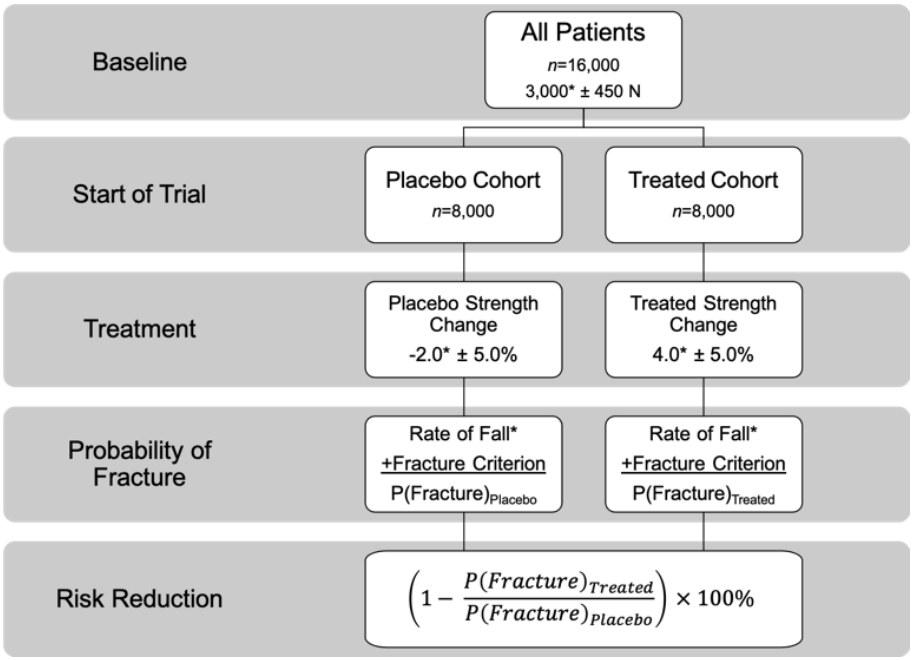


Figure 3-1: Flowchart of the theoretical framework developed to investigate how small changes in bone strength influence the probability of fracture in a placebo (left) and treated (right) cohorts. All values are based on data from the literature, including population size [24], *baseline bone strength mean and standard deviation* [24], [155], *bone strength change* [24], [29], *rate of fall* [156], *and fracture criterion* [151]. *All data are shown as mean ± standard deviation; values marked with an asterisk (*) were varied parametrically.*

3.2.1 Baseline cohort

For all analyses the reference case values were taken from the "LOFT" odanacatib clinical trial [24], [29] due to its relatively large sample with FEA-derived strength measurements, and representation of the general problem of small changes in strength corresponding to large changes in hip fracture risk reduction. As bone strength is not typically measured during clinical trials, we developed a relationship to specify femoral strength that corresponds to the reported femoral neck areal BMD, using data reported by Hong et al. [155] for white women in the U.S.

To validate this relationship, we applied it to the baseline data from Brixen et al. in the LOFT trial [29], which reported both areal BMD and bone strength. For this cohort, the reported baseline mean (± SD) femoral strength was 3200 ± 400 N; using Hong, the predicted mean femoral strength for Brixen from the reported mean femoral neck areal BMD values in Brixen was approximately 3500 N. As the predicted mean strength for Brixen was within one standard deviation of the reported mean for Brixen, the BMD-bone strength prediction model from Hong was accepted.

Table 3-1: Reference study parameters and ranges of any varied parameters.

Parameter	Value	Range	Reference
Population size	16,000		McClung and colleagues [24]
Baseline Strength [N]			
Mean	3,000	2,000 – 4,000	Hong and colleagues [155]
Standard Deviation	450		McClung and colleagues [24] Adams and colleagues [157]
Fall rate [%]	18	12-28	U.S. Dept. of Health and Human Services [156]
Fracture criterion	**Φ** = 1.5		Keaveny and Bouxsein [151]
Net strength change [%]			
Mean	6%	4-10	Brixen and colleagues [29]
Standard Deviation	5%	1-10	
Placebo			
Strength change [%]			
Mean	-2	0 to -6	Brixen and colleagues [29]
Standard Deviation	5	1-10	
Treated			
Strength change [%]			
Mean	4	2-9	Brixen and colleagues [29]
Standard Deviation	5	1-10	

Based on reported values of femoral neck areal BMD from the LOFT trial, we generated a baseline cohort (n = 16,000 patients) with a defined average strength normally distributed within defined boundary conditions (Figure 3-1). First, we utilized the aforementioned relationship between BMD and bone strength to estimate the starting cohort bone strength mean and standard deviation. In the LOFT trial [24], the reported areal BMD of the femoral neck of the baseline cohort provided a reference case baseline bone strength mean and standard deviation of approximately 3000 ± 450

N (Table 3-1). In all analyses, the baseline bone strength values for the simulated patient population (n = 16,000) were normally distributed about the mean bone strength (Figure 3-2, top).

At the start of the trial, the baseline population was split into two, with each individual femoral strength value (or patient) randomly assigned to either the placebo (n = 8,000) or treatment (n = 8,000) group (Figure 3-2, middle row). After random assignment, the distributions of each group were confirmed to maintain the prescribed mean strength (reference case: 3000 ± 450 N). These distributions for each cohort were the bone strengths for the start of the simulated trial.

We investigated the sensitivity of risk reduction to the baseline population mean femoral strength through a parametric analysis. Here, all reference values in Table 3-1 were held constant except the baseline strength mean, which varied from 2,000 to 4,000 N in increments of 250 N.

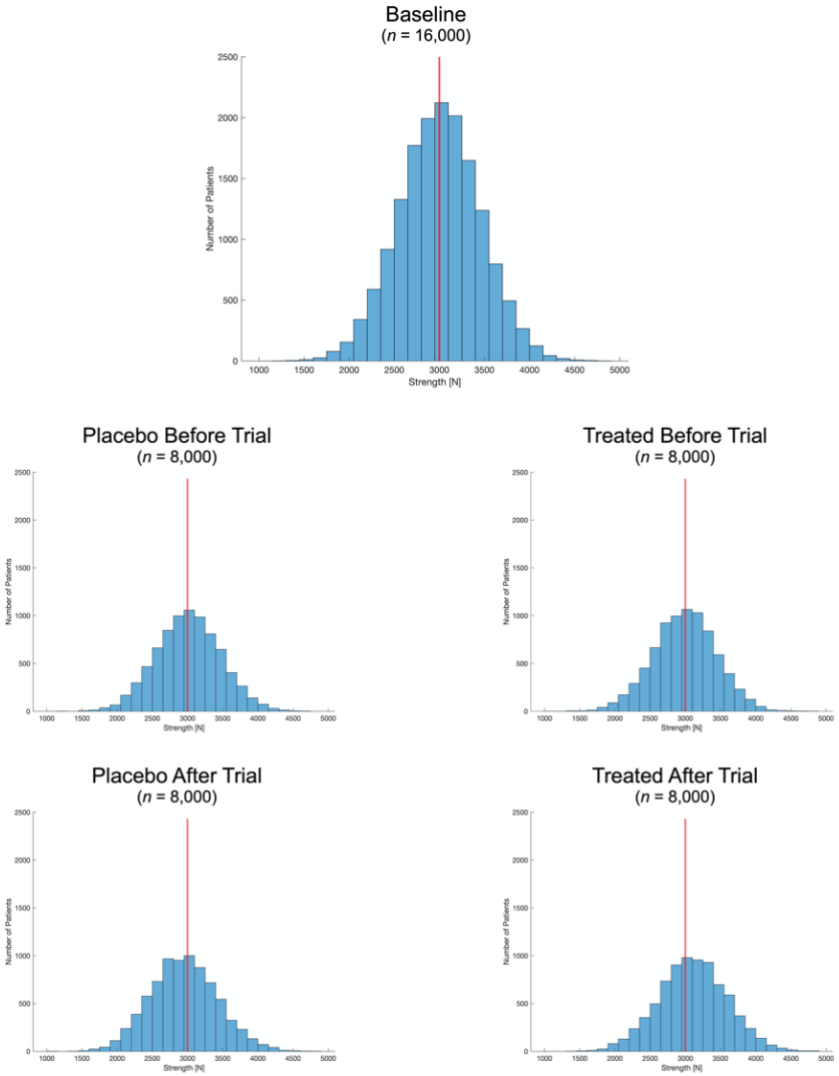


Figure 3-2: Femoral strength distributions for the baseline cohort (top; n = 16,000 patients) and the two groups (n = 8,000 patients for each placebo (left) and treated (right)) before the trial (middle row) and after the trial (bottom row) for a single Monte Carlo iteration. Red vertical line indicates reference baseline femoral strength mean of 3,000 N.

3.2.2 Eligibility criteria

A critical factor in a clinical trial is the set of criteria by which patients are eligible to participate in the study, thereby defining the patient population under investigation. While these criteria are often tailored to allow assessment of treatment effectiveness in a well-defined population, at times this results in the enrollment of study populations that may not represent the broader patient population in eventual clinical practice. Inclusion criteria specify the characteristics required for entry into a study; in the case of osteoporotic drug treatments, this is usually postmenopausal women. In contrast, exclusion criteria specify characteristics that disqualify patients from participation in a study, and often include factors such as comorbidities or concomitant treatment that could mask the effect of the treatment under review. Regardless, eligibility criteria could impact the patient populations in the current study and is an important factor to consider.

A common eligibility criterion in trials for osteoporotic treatments are patient T-scores. While some studies may require all patients to be osteoporotic (T-score -2.5 and below), some may include osteopenic patients with low bone density who are not osteoporotic (T-score between -1 and -2.5). The lower a person's T-score, the lower the baseline bone strength. Introducing a lower bound may render the population non-normally distributed, which might affect treatment risk reduction.

Here, we compared the reference study parameters (femoral strength > 0 N) to a population with strength values bounded by T-score criteria from clinical trials. We examined the impact of two commonly used BMD criteria: (1) osteoporotic and osteopenic T-scores of -4.0 to -1.5 [23], [24] at the femoral neck, which equates to approximately 1600 to 3700 N [155] and (2) only osteoporotic T-scores of -4.0 to -2.5 [24], [121], or approximately 1600 to 2900 N [155]. These bone strength bounds were enforced on the baseline population prior to treatment-induced bone strength changes.

3.2.3 Treatment-related parameters

Treatment effects were then implemented for each group (Figure 3-1). We focused on bone strength changes at 24 months, the usual trial duration required by regulatory agencies. Bone strength changes were based on a finite element analysis of bone strength for a smaller cohort of LOFT participants before and after treatment [29]. The mean percentage change in both femoral neck and total hip areal BMD between the placebo and treated groups for the smaller [29] and larger [24] cohort were in good agreement, at approximately 4% at 24 months. This agreement suggests that all mean percent changes in the bone — including changes in femoral strength — for the larger cohort were similar to those in the smaller cohort.

For the current analysis, at 24 months placebo patients lost bone strength (reference value: -2 ± 5%) while treated patients gained bone strength (reference value: 4 ± 5%). As with baseline bone strength values, a distribution of strength changes was created to be normally distributed about the prescribed means with the requisite standard deviation, this time for each group (Table 3-1). Then, each starting bone strength value (i.e., each patient) was randomly assigned a bone strength change based on its group, resulting in a final distribution of bone strengths. On average, the mean of the final distribution of bone strengths at the end of the trial increased for the treated group and decreased for the placebo group (Figure 3-2, bottom row).

We examined the effects of variations in the assumed values for the changes in mean bone strength. All reference values were held constant except for the change in bone strength, which ranged from 2 to 8% for the treated group and 0 to -6% for the placebo group (Table 3-1). Collectively, this resulted in an investigation of a net change in bone strength between treated and placebo groups ranging from 4% to 10%.

3.2.4 Fracture risk prediction

To evaluate fracture risk for each simulated patient, we utilized a load-to-strength ratio approach for a simulated sideways fall coupled with the probability of falling (Figure 3-1). With this approach, the patient will fracture only if they fall and the applied force to the side of the hip exceeds the femoral strength.

Fall rate

The rate of patients in this age group falling was set to 18% based on literature from the U.S. Department of Health and Human Services [156] and calibration to produce an absolute number of fractures consistent with the LOFT clinical trial. Changing the fall rate did not influence the reduction in risk and was chosen to produce an absolute number of fractures consistent with the clinical trial [24]. See Supplementary Material for details.

*Load-to-Strength Ratio (**Φ**)*

The likelihood of a falling patient to fracture is determined by their femoral bone strength and its relationship to the load to the side of the hip. Thus, using previously published clinical data [151] we developed a continuous sigmoidal function between femoral strength and fall load. Specifically, femoral strength for simulated fall to the side of the hip was plotted against a load-to-strength ratio (**Φ**) based on a biomechanical fracture threshold [151] (Figure 3-3). This ratio of **Φ** represents the external force during a fall to the strength of the femur. Theoretically, when the biomechanical fracture threshold is exceeded—the external load exceeds the femoral strength—the bone will fracture. The published model uses factors such as patient weight and height to estimate the loads acting on the hip during a sideways fall, and ultimately defines a value of 1.0 as the theoretical value of the fracture threshold. However, factors which can attenuate the external impact force of the fall, such as soft tissue thickness or muscle contraction, were not fully accounted for. Attenuation of the external load would result in a lower impact force to be delivered to the femur (i.e., the "load" in the original model is an overestimate). Thus, we investigated the effect of simulated force attenuation by varying the load-to-strength ratio (**Φ**) from 1.0 to 1.6 and selected a value of **Φ** = 1.5 to simulate the effect of attenuation on femoral impact force [158] (see Supplemental Materials for details).

Fracture Criterion

With this model of fracture risk, there is a transition range of bone strengths where the prediction of fracture upon falling is not certain. Specifically, those with very low bone strength (<1500 N) are guaranteed to fracture (probability of fracture = 1), while those with very high bone strength (>4000 N) are guaranteed to *not* fracture (probability of fracture = 0) (see Figure 3-3). For those values of bone strength in between these extremes, the probability of fracture varies nonlinearly between zero and one. Utilizing data from Keaveny and Bouxsein [151], we established this

nonlinear relationship between bone strength and probability of fracture is based on the ratio of points above the theoretical fracture ratio to all points for bone strength values within 500 N bins. Ultimately, if a patient were to fall, the probability of their fracture would be based on this sigmoidal relationship.

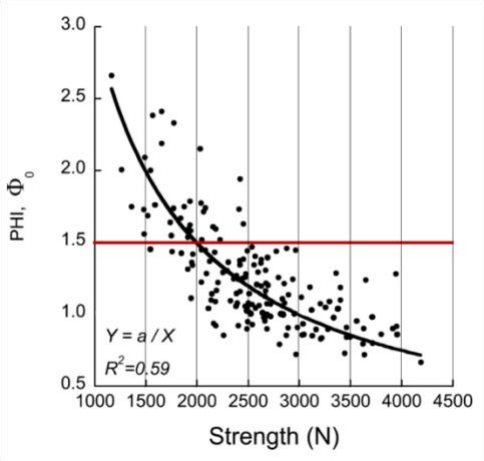


Figure 3-3: The relationship between the load-to-strength ratio $\boldsymbol{\Phi}$ *versus femoral strength for a simulated fall to the side of the hip, adapted from* [151]*. This relationship indicates that subjects with very low bone strength (<1,500 N) are highly likely to be above the theoretical fracture threshold (red line) but that subjects with slightly higher bone strength values (2,000 – 4,000 N) have a non-zero probability of fracture. For each bin of 500 N (vertical lines), the probability of fracture for bone strengths within that bin was calculated as the ratio of data points below the theoretical fracture threshold to all points in the bin.*

3.2.5 Outcome — Risk Reduction

For all analyses, we quantified the reduction in the risk of fracture for patients in the treatment group (compared to the placebo group) using Bayes theorem. Regardless of treatment group, we used Bayes theorem to define the probability of fracture as a combination of (a) fall rate (b) the likelihood of falling given a fracture and (c) the likelihood of fracturing given a fall. The fall rate, or the probability of falling **P(Fall)**, is the ratio of the number of patients who have fallen to the total number of patients in each group. The likelihood of falling given that an individual has fractured is the probability of a patient falling given that they have fractured **P(Fall | Fracture)**, while the likelihood of an individual fracturing given they have fallen is the probability of fracturing given a fall **P(Fracture | Fall)**. Thus, the probability of fracture for each group was equivalent to:

$$P(Fracture) = \frac{P(Fracture \mid Fall) \times P(Fall)}{P(Fall \mid Fracture)}$$

The relative risk of a patient fracturing was defined as to the ratio of the probability of a fracture occurring in the treatment group to the probability of a fracture in the placebo group:

$$\frac{P(Fracture)_{Treated}}{P(Fracture)_{Placebo}} = \frac{P(Fracture \mid Fall)_{Treated} \times P(Fall)_{Treated} \times P(Fall \mid Fracture)_{Placebo}}{P(Fall \mid Fracture)_{Treated} \times P(Fracture \mid Fall)_{Placebo} \times P(Fall)_{Placebo}}$$

Importantly, we assumed a fracture can only occur following a fall (i.e., no spontaneous fractures). Further, our model assumed the probability of falling to be constant for both groups, relying solely

on the strength of the bone and its relation to the fracture criterion. Additionally, we did not examine the probability of falling given a fracture as it was assumed constant for both groups. Thus, the calculation of relative risk was simplified via two assumptions:

(1) the probability of fall is equivalent for both groups

$$P(Fall)_{Treated} = P(Fall)_{Placebo}$$

(2) the probability of falling given a fracture is equivalent for both groups

$$P(Fall \mid Fracture)_{Treated} = P(Fall \mid Fracture)_{Placebo}$$

Thus, the calculation for risk reduction was simplified to:

$$\frac{P(Fracture)_{Treated}}{P(Fracture)_{Placebo}} = \frac{P(Fracture \mid Fall)_{Treated}}{P(Fracture \mid Fall)_{Placebo}}$$

The final metric used to evaluate each study is the risk reduction, or the reduction in the risk of fracture for patients in the treatment group.

$$Risk\ Reduction = \left(1 - \frac{P(Fracture)_{Treated}}{P(Fracture)_{Placebo}}\right) \times 100\%$$

In the LOFT trial, the relative risk of fracture at 24 months was approximately 0.59, with treatment providing a risk reduction of 41% [24], our target metric.

Monte Carlo Approach

This entire procedure, from the creation of an initial distribution of bone strengths through calculation of risk reduction, was repeated 10,000 times for each of the parameters analyzed.

Parameter Studies

In total, we conducted three parameter studies investigating the effect of altering the reference study parameters, as listed in Table 3-1, on risk reduction. For each parameter evaluated, the mean and standard deviation of the risk reduction for all 10,000 Monte Carlo iterations were calculated and compared to the risk reduction for LOFT at 24 months—41%. Starting with the reference case, details on each parametric analysis and their respective influence on risk reduction are outlined below. All data are reported as mean ± standard deviation.

3.3 Results

3.3.1 Reference case

In our reference case analysis, our model resulted in a risk reduction of 37 ± 4% and was consistent with the clinical trial result of 41%. As expected from our choice of fall rate (Supplementary Material), the total number of fractures was consistent with clinical observations, with 78 ± 4 fractures in the placebo group (compared to approximately 75 fractures observed clinically at 24 months [24]).

3.3.2 Baseline population bone strength mean

Treatment efficacy—i.e., risk reduction—increased with increasing baseline mean femoral strength, in an approximately linear fashion (Figure 3-4). At the reference bone strength mean (3,000 N), the risk reduction was 37 ± 4%. When the baseline mean strength was decreased to 2,000 N, the risk reduction decreased to 16 ± 2%. In contrast, when the baseline mean strength was increased to 4,000 N, the risk reduction increased to 53 ± 8%. As mean baseline strength decreased, the standard deviation on the risk reduction tightened.

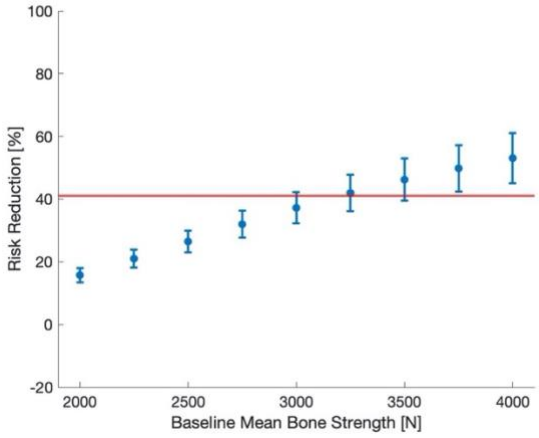


Figure 3-4: Treatment efficacy. Fracture risk reduction due to varying bone strength mean for the baseline population. Data are presented as mean ± standard deviation for the 10,000 iterations. The red line indicates 41% risk reduction, which was observed clinically.

Mechanistically, improved efficacy with increasing femoral strength is explained by a decrease in the absolute number of fractures. With increasing femoral strength, the absolute number of fractures and the number of prevented fractures decreased in a non-linear fashion (Figure 3-4). The reduction in the absolute number of fractures was due to a larger number of patients with femoral strengths with little to no risk of fracture based on the fracture threshold (Figure 3-3). Further, as the total number of fractures decreased the number of prevented fractures also decreased, resulting in diminished effectiveness (compare Figure 3-4 and Figure 3-5). However, with a relatively small absolute number of fractures, each individual fracture played a significant role in our risk reduction statistics. For example, a single prevented fracture had a minimal influence on risk reduction when the absolute number of fractures was large (i.e., > 1,000 fractures as seen for a mean femoral strength of 2,000 N), but an exceedingly large influence when the number of fractures was small (i.e., < 10 fractures as seen for a mean femoral strength of 4,000 N). Thus, while the treatment may have high efficacy via measure of fracture risk reduction for large baseline femoral strength, the effectiveness or actual number of prevented fractures is relatively small.

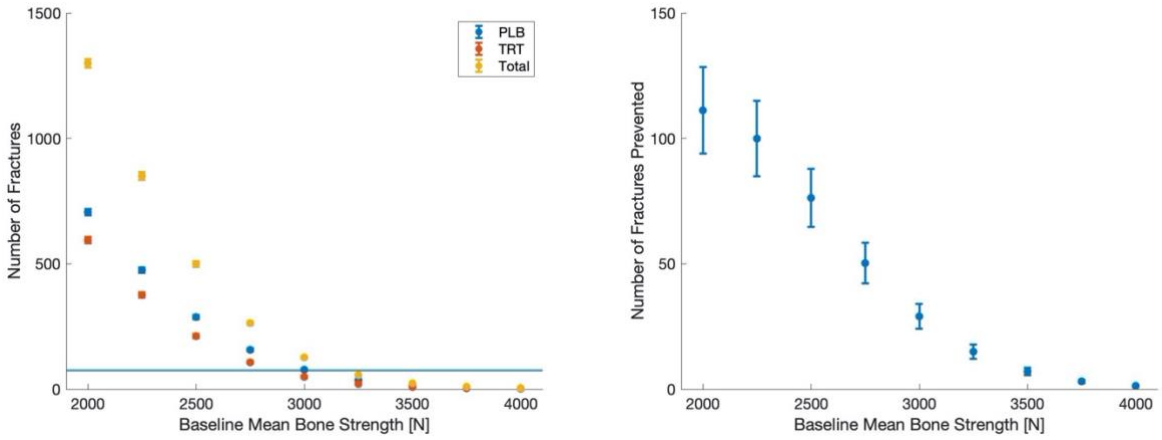


Figure 3-5: Treatment effectiveness. Number of fractures (left) and the absolute effect, or number of fractures prevented (right), with varying baseline bone strength means. Number of fractures prevented is defined as the number of fractures in the placebo group minus the number of fractures in the treated group. The blue line indicates number of placebo fractures observed clinically (75 fractures) [24]. *Data are presented as mean ± standard deviation for 10,000 iterations.*

3.3.3 Baseline population bone strength changes

Small changes in bone strength resulted in large changes in risk reduction, again in an approximate linear fashion. At the reference net femoral strength change of 6% (+4% treated, -2% placebo), the overall reduction in risk was 37 ± 4%. Increasing the net strength change from 4 to 10% reduced fracture risk from 26 ± 6 to 54 ± 4%, respectively (Figure 3-6). The overall risk reduction trends are consistent regardless of the specific bone strength changes in the placebo or treated group (Figure 3-7); ultimately, the *net* change in bone strength determined the overall risk reduction.

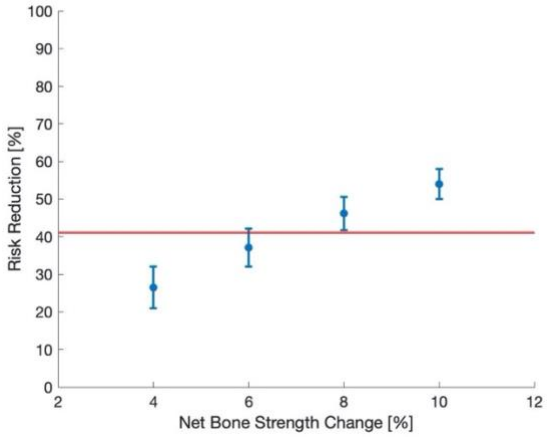


Figure 3-6: Risk reduction due to varying net bone strength change between treated and placebo groups. Data are presented as mean ± standard deviation for the 10,000 iterations. The red line indicates 41% risk reduction, which was observed clinically.

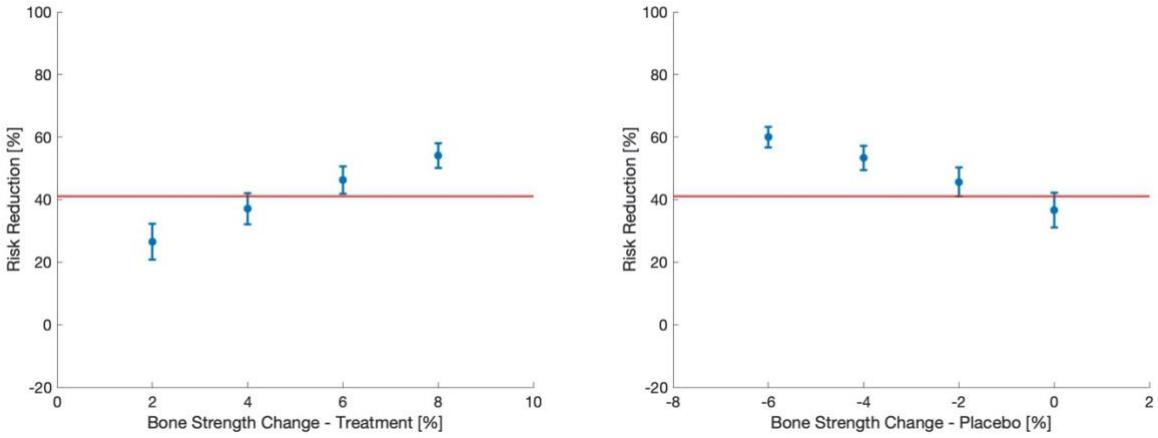


Figure 3-7: Risk reduction due to varying bone strength change for the treated (left) and placebo (right) groups. All parameters were held constant at reference values (Table 3-1) except the bone strength change, as indicated by the x-axis label. Data are presented as mean ± standard deviation for the 10,000 iterations. The red line indicates 41% risk reduction, which was observed clinically.

3.3.4 Eligibility criteria

While the baseline population was unaltered for the reference case (>0 N; Figure 3-8A), both bounded eligibility criteria resulted in truncations of some baseline bone strength values, albeit with negligible impact on risk reduction. Enforcing the first bounded eligibility criterion (T-score -4.0 to -1.5; strength 1,600 to 3,700 N) resulted in a slight truncation of the population, with a loss of approximately 4%, or less than 1,000 of the 16,000 patients (Figure 3-8B). As a result, the actual baseline mean bone strength was slightly lower at 2,950 N, and the fracture risk reduction was minimally altered (reference model: 37 ± 5%; for the truncated model: 38 ± 5%). In contrast, enforcing the second eligibility criterion (T-score -4.0 to -2.5; strength 1,600 to 2,900 N) truncated the population by nearly 60%, resulting in a baseline mean of 2,600 N and a non-normal distribution (Figure 3-8C). Interestingly, these truncation effects did not substantially alter the risk reduction (reference model: 37 ± 5%; truncated model: 36 ± 5%).

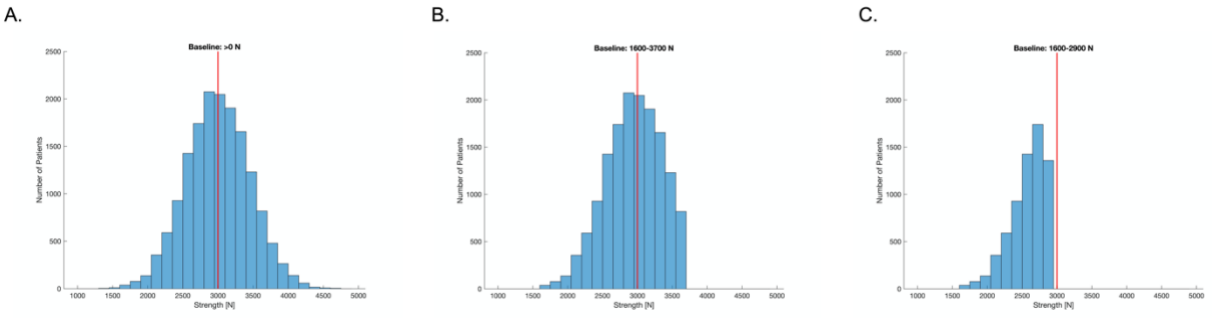


Figure 3-8: Effect of baseline population eligibility criteria on patient population for a single Monte Carlo iteration. (A) Reference case—baseline population is bounded above 0 N. (B) First eligibility criterion—population is between 1,600 and 3,700 N, equivalent to total hip T-scores between -4.0 to -1.5—an osteoporotic and osteopenic population. (C) Second eligibility criterion—population is between 1,600 and 2,900 N, equivalent to total hip T-scores between -4.0 to -2.5—an osteoporotic population. Red vertical line indicates reference baseline femoral strength mean of 3,000 N.

In contrast, for baseline bone strength means well above and below the reference mean (i.e., 3000 ± 1000 N), enforcing the eligibility criterion had a significant impact. For the first eligibility criterion, a prescribed mean of 2,000 N resulted in truncation of ~12% of the population, ultimately resulting in an actual mean of 2,200 N. As a result, the risk reduction was higher for the truncated group (~22%) than the reference population (~16%). Conversely, for a prescribed mean of 4,000 N the first eligibility criterion removed ~75% of the population, decreasing the mean to 3,400 N and resulting in a risk reduction slightly lower for the truncated group (~51%) than the reference population (~53%). The second criterion followed a similar trend, with a very low average strength resulting in a higher risk reduction than the reference, while a very high mean strength predicting a lower risk reduction.

3.4 Discussion

The goal of this study was to provide a mechanistic explanation of how small changes in bone strength, as observed in clinical trials, can lead to the large observed changes in fracture risk. Using a Monte Carlo approach, we developed a theoretical framework which provided a biomechanical understanding of osteoporosis treatment-induced fracture risk reduction. The results confirm that small changes in bone strength—based on clinical measures of net 6%—can reduce the risk of fracture by approximately 40%, consistent with clinical observations [23]–[25], [121]. Further, greater net bone strength changes were associated with greater reductions in hip fracture risk. Overall, we found that the predicted fracture risk reduction was sensitive to the net difference in treatment-induced bone strength changes, the starting baseline bone strength, and the eligibility criteria bounding the population.

We determined that a net difference in bone strength changes between the treated and placebo groups dictated fracture risk reduction—a net change of 8% reduced fracture risk by approximately 50%. These trends are consistent regardless of the absolute bone changes in either group, suggesting the relative behavior of both arms of a clinical trial is more critical than the absolute performance of the treatment. Although our model for hip fracture risk reduction is theoretical, its feasibility is supported by real world clinical evidence. The model performance is consistent with the antiresorptive odanacatib clinical trial data [24] by design and can be extrapolated to other treatments that have been shown to prevent hip fractures. For example, clinical trials for denosumab and alendronate have shown net bone strength changes of approximately 8% after two years [27], [30] with an associated 50% reduction in risk for hip fracture [23], [25], [121]. This is consistent with our model, which estimates an 8% difference in net strength can reduce hip fracture risk by approximately 50%.

Surprisingly, our model indicated that risk reduction in a clinical trial should be greater if the trial is run on a healthier population. This is due to a reduction in the overall number of fractures, causing each prevented fracture to have a greater influence on risk reduction statistics, ultimately resulting in high treatment efficacy. However, in the same healthier population the effectiveness of treatment trended in the opposite manner, where fewer than 10 fractures were prevented. This highlights an important distinction between the risk reduction observed in a clinical trial, or the efficacy, and the clinical benefit, or the effectiveness. Further, it suggests that these treatments may not have much clinical benefit if utilized in mainly osteopenic patients, supporting current practices [159]. These results are in line with previous work suggesting that baseline

characteristics, in particular BMD, can be indicators for fracture risk [149], [160], [161]. While our model showed that risk reduction is greater in a healthier population, clinical trials have shown the opposite—lower baseline BMD is required for measurable risk reduction [123], [148], [162]. Our model provides a possible explanation for this discrepancy. Our results indicated a larger standard deviation on risk reduction for higher strength values (Figure 3-4), suggesting that clinical trials in healthier patients may not have sufficient statistical power to show efficacy. Together, our model and these results suggest that baseline strength are important in trial recruitment and clinical implementation.

Interestingly, the overall risk reduction trends due to strength changes are determined by the *net* change in femoral strength (Figure 3-6) and not the specific strength changes in the placebo or treated group (Figure 3-7). Thus, our model is agnostic to whether patients gain or lose bone, suggesting that sicker people—who would lose more bone if left untreated—have more to gain from an anti-resorptive therapeutic than an anabolic drug increasing bone mass.

Our results also demonstrated the sensitivity of fracture risk reduction to patient eligibility and exclusion criterion. Clinical trials, including those for osteoporotic therapies, are inherently biased due to the necessary patient selection and exclusion criteria. In patient populations that are much weaker or stronger than the reference population, our results showed that enforcing BMD-based bone strength bounds resulted in significant truncation of the patient population, ultimately altering the observed risk reduction. This has several implications. First, truncation renders the population non-normally distributed, suggesting standard statistical analysis of clinical outcomes may be misleading. Further, our results showed that selection bias can influence measures of efficacy. For example, removing patients with very weak bones will benefit efficacy measures with a larger risk reduction, as treatments are unlikely to move these patients beyond the fracture threshold [151] (Figure 3-8).

The proposed theoretical framework expands upon the implications of a biomechanical fracture threshold [151]. First, our model provides some level of validation for the concept, as our criterion built on a nonlinear fracture threshold was able to replicate clinical data for osteoporosis treatments. Further, the current work expanded on the concept of a fracture threshold by taking soft tissue attenuation into account. Additionally, our results support the idea that the outcome of clinical trials may be dominated by those subjects whose load-to-strength ratios $\mathbf{\Phi}$ at baseline are already relatively close to the biomechanical fracture threshold in the "transition zone". While populations with mean bone strengths within the transition zone provided high treatment efficacy, populations whose means were well below this transition zone demonstrated that increases to the patient's bone strength were insufficient to prevent fracture and resulted in low treatment efficacy. Collectively, our work demonstrates the relevance of a biomechanical fracture threshold in osteoporotic therapy fracture risk reduction predictions and could be a basis for future innovative use.

Previous analyses have sought to provide an explanation for how small changes in BMD or bone strength have a large influence on fracture risk, but the results have lacked mechanistic explanation. The results of the current study are in line with a meta-analysis of data from multiple clinical trials [149], which associated small changes BMD with fracture risk. While informative, the meta-analysis did not provide biomechanical explanation for the changes in fracture risk. Our

results expanded on this meta-analysis and provided unique insight by conclusively demonstrating how treatment-induced bone strength changes influence fracture risk reduction. For example, while risk reduction varied linearly with changing baseline strength or strength changes, the number of fractures was highly non-linear. The relationship between the number of fractures and baseline bone strength is due to the nonlinear relationship between bone strength and fracture risk (Figure 3-3). With small changes in femoral strength, patients are moving below fracture threshold and thus not fracturing. However, changing the average baseline mean strength moves the same number of patients in each group below the fracture threshold, thus keeping the relationship between the number of fractures in each group constant. Ultimately, this results in the observed linear relationship between baseline strength and risk reduction.

Although our results are consistent with real-world clinical data, the main limitation of this work is the theoretical nature of the model. Due to the assumptions built into the current model, our specific results are not generalizable beyond hip fracture risk reduction in a post-menopausal female population. Because the risk of hip fracture varies based on age [163], race [163], [164], geographic location [164], and socioeconomic status [165], [166], so too do our results. Therefore, while the results presented are necessarily specific, the approach used here to model fracture risk could be universally applicable as our model demonstrates some level of generality. For example, altering fall rate influenced the number of fractures and not the risk reduction, suggesting a level of robustness in the basic model assumption. As such, this theoretical framework can be customized with relevant data and applied to non-hip fractures, as well as other populations (i.e., men), and treatments (i.e., radiation therapy).

While the lack of clinical bone strength data was a limiting factor in developing a relevant model for radiation therapy induced fracture risk, the current model provided important insight for this treatment. As demonstrated in Chapter 2, it is possible for radiation to reduce bone strength outside of changes to bone quantity on the order of 6%. The current model suggests a net change in bone strength of this magnitude can alter fracture risk by ~40%, similar to clinical observations of increased fracture risk for irradiated patients [4]. Thus, if a similar change in bone strength due to treatment-induced material changes is present with clinical radiation, it may help to explain the increased fracture risk for patients undergoing radiation therapy despite the inconclusive correlation between irradiation and decreased bone mass [8], [101]–[103].

In summary, the current study provided a theoretical framework and a biomechanical understanding of the association between small changes in bone strength and large changes in fracture risk. Importantly, by incorporating bone strength changes into the model, we were able to duplicate the risk reduction in a clinical trial and a mechanistic explanation for the observed large changes in fracture risk. While the results are not generalizable beyond osteoporotic treatments in post-menopausal women, it is hoped that this biomechanical perspective provides some new mechanistic insight into the connection between clinical observations of altered fracture risk with various treatments. Furthermore, this theoretical framework can be customized and applied broadly to provide additional insight into clinical observations in other therapeutic areas.

3.5 Supplementary Material

Load-to-Strength Calibration

Mechanistically, if during a fall the external load to a patient's bone exceeds its strength, the bone will fracture. This biomechanical fracture threshold can be reflected by the load-to-strength ratio **Φ**, or the ratio of the external force during a fall to the strength of the bone. Thus, when the load-to-strength ratio **Φ** exceeds a value of 1.0, a fracture will occur in the event of a fall. Utilizing clinical data and patient-specific finite-element analysis, Keaveny and Bouxsein calculated the load-to-strength ratio **Φ** for a population of postmenopausal osteoporotic women [151], where the higher the value of **Φ** the greater the likelihood the bone will fracture. However, the force value used to calculate **Φ** may have overestimated the actual femoral impact force, as it did not account for attenuation of the external load by surrounding soft tissues and muscle contraction which would ultimately reduce the actual force applied to the femur by up to 58% [158]. Scaling **Φ** can account for this attenuation. Here we investigated the effect of simulated force attenuation by varying the load-to-strength ratio (**Φ**) from 1.0 to 1.6 while all other reference values in Table 3-1 were held constant.

We observed that as **Φ** increased from 1.0 to 1.4, the fracture risk reduction increased; for values of **Φ** ≥1.4, risk reduction remained constant at approximately 37% (Figure 3-9). Further, low values of **Φ** resulted in an unrealistically large number of fractures (i.e., **Φ** = 1.0 resulted in >2000 patients fracturing). We selected a value of **Φ** = 1.5 in order to simulate soft tissue attenuation to a more realistic femoral impact force and fracture risk [158].

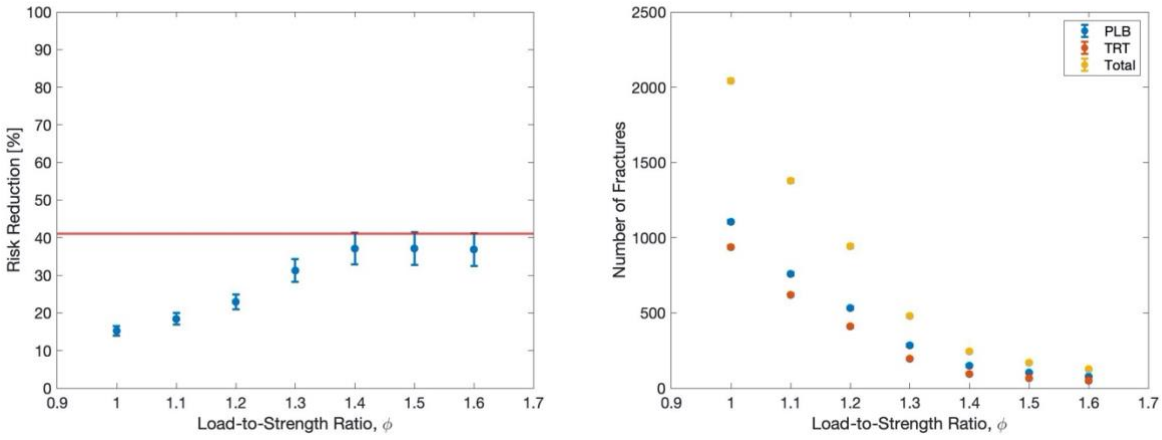


*Figure 3-9: Influence of load-to-strength ratio (**Φ**) on fracture risk reduction (left) and number of fractures (right). The horizonal line represents 50% risk reduction (red line) and number of fractures in placebo group observed clinically* [24] *(blue line, 75 fractures) for left and right figures, respectively.*

Fall Rate Calibration

Based on literature from the U.S. Department of Health and Human Services, approximately 24% of women over age 50 fall each year [156]. However, utilizing this fall rate with the references values in Table 3-1 resulted in a total number of fractures which exceeded clinical observations with 168 ± 6 fractures versus a reported total of 119 fractures at 24 months [24]. We investigated the influence of fall rate on the fracture risk reduction as well as the number of fractures in each

group. All reference values in Table 3-1 were held constant except the fall rate, which varied from 12 to 28%.

While fall rate did not significantly influence the mean fracture risk reduction, it did alter the number of fractures. Risk reduction remained approximately 37% for all fall rates (Figure 3-10, left). In contrast, the total number of fractures increased as the fall rate increased. The fall rate required to achieve approximately the same number of fractures as seen clinically at 24 months, or approximately 75 fractures in the placebo group [24], was 18% with 78±4 fractures (Figure 3-10, right). Thus, we utilized a fall rate of 18% for all analyses.

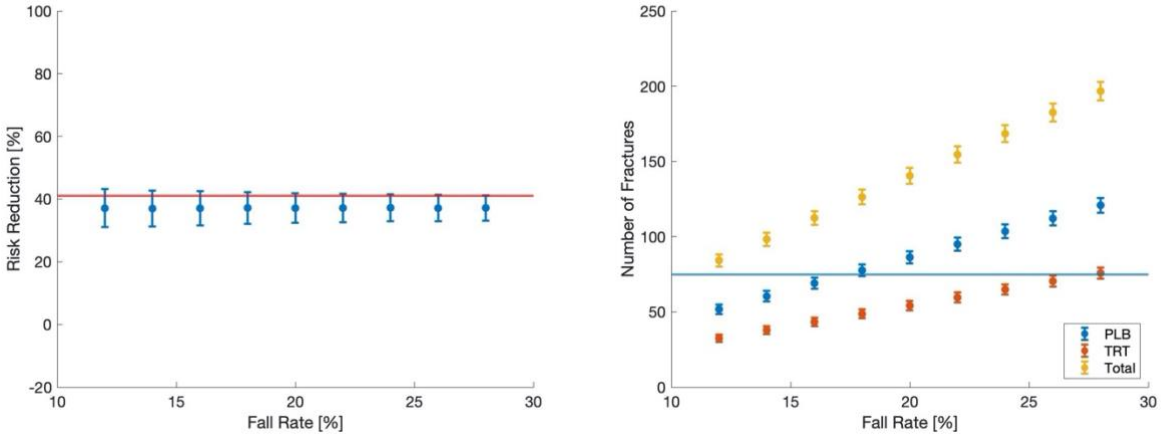


Figure 3-10: Influence of fall rate (%) on fracture risk reduction (left) and number of fractures (right). Horizonal lines represent clinically observed data for the LOFT trial at 24 months [24]*: 41% risk reduction (left, red line) and the number of fractures in the placebo group (right, blue line).*

4 Conclusions

The overall goal of this dissertation was to enhance current understanding of the biomechanical mechanisms of bone strength and elucidate how small changes in bone strength led to large changes in fracture risk. The findings of this dissertation are both scientifically and clinically significant. From a basic science perspective, substantial insight was gained into how bone mass and microstructure versus tissue material can alter bulk mechanical properties. From a clinical perspective, these insights demonstrate how bone quality factors can play a substantial role in bone strength and provide a mechanistic explanation to how small treatment-induced changes in bone strength can influence fracture risk in a significant way. Furthermore, this dissertation has provided insight into the importance in combining experimental and computational evaluation of treatment bone mechanical properties.

First, we presented our findings for the relative effects of treatment-induced changes in bone mass, microstructure, and tissue material behavior on bone strength using a murine model of radiation therapy. Radiation therapy is an effective cancer treatment, but the risk of fracture is increased for bone within the radiation field, presumably due to radiation-induced reduction in bone strength. The exact mechanisms leading to reduced bone strength are unclear in terms of how much of this weakening effect is due to changes in mass and microstructure versus tissue material. We addressed this using a unique combination of experimentation and microcomputed tomography-based nonlinear finite element analysis (FEA). Irradiation reduced the experimentally measured vertebral strength by 27.9% ($p \leq 0.001$). Importantly, the relation between the experimental and FEA strength measurements was strong ($R^2 = 0.86$) but depended on treatment ($p \leq 0.03$). This dependency indicated that irradiation altered some biomechanical feature that was not contained in the FEA models, namely some aspect of the tissue material properties since they were assumed to be the same in all FEA models. The absolute magnitude of this material effect on vertebral strength represented 23.6% of the observed average reduction in vertebral strength. We concluded that, in this rat model of localized irradiation, changes in mass and microarchitecture together accounted for about 76% of the observed reduction in vertebral strength and changes in material accounted for about 24% of the overall biomechanical effect. Our findings suggest that although the overall biomechanical effect of radiation is dominated by mass (~60%), comparatively small material alterations can account for nearly a quarter of the observed 27% change in bone strength, or about 6% of the overall mean strength.

Next we demonstrated how bone strength changes of this magnitude of ~6% are sufficient to influence fracture risk. Using a Monte Carlo approach with conditional probability and data from placebo-controlled osteoporosis trials, we provided a biomechanical approach to the phenomenon of small changes in bone strength associated with large changes in fracture risk. Our model provided a mechanistic understanding of osteoporosis treatment-induced fracture risk reduction by successfully replicating a clinically observed treatment efficacy of approximately 40% with a 6% net change in bone strength. Additionally, our unique analysis provides a foundational mechanistic explanation for how small changes in bone strength can lead to the large changes in fracture risk. For example, as demonstrated in the animal study it is possible for radiation to reduce bone strength outside of changes to bone quantity on the order of 6%. This model suggests a net change in bone strength of this magnitude can alter fracture risk by ~40%, similar to clinical observations of

increased fracture risk for irradiated patients. While the results are not generalizable, this model can be tailored to analyze bone strength changes due to radiation therapy and its association to fracture risk, ultimately providing a mechanistic understanding of increased fracture risk in cancer patients.

Together, the work in this dissertation will lead to improved understanding of radiation and osteoporosis treatments and provide new insight into how to best reduce fracture risk. A key strength of this project was the methodology used to quantify treatment effects: a combination of mechanical characterization, finite element modeling, and Monte Carlo simulations. Together, these methods provide novel information on the impact of treatment on bone structure-function relationship and have identified the relative influence of key contributors to hip fracture risk—namely, material and structural changes. Combining biomechanical testing with high resolution nonlinear micro-CT-based finite element analysis enabled us to exploit the unique capabilities of each technique and gain insight into the treatment effects of radiation therapy. This research has advanced quantitative understanding of bone mechanics following radiation treatment and enhanced the science of tissue characterization. Importantly, this work addressed key knowledge gaps regarding the determinants of the deficits that underlie skeletal fragility and has laid a foundation for future development of clinical approaches to prevent fractures.

There are several potential areas of future research that can further extend the relevance of the work presented in this dissertation. First, results from the two studies combined could provide important insight into the mechanisms driving fracture risk following radiation treatment. In particular, the current theoretical framework suggests that bone strength changes on the order of 6%, as observed following radiation treatment, can impact fracture risk outcomes significantly. This suggests that more simulations need to be done to better characterize the mechanisms driving increased risk of fracture following radiation treatment. Second, while the small-animal model of radiation therapy provided important insight into radiation treatment-specific effects on bone strength and structure, cancer therapy rarely confined to this single mode of treatment [3]. Thus, future work exploring the effect of multimodal therapy, including chemotherapy agents and/or antiresorptive drug treatments, is warranted. Finally, the combination of finite element modeling and biomechanical testing is a useful evaluation tool in any application where the effects of mass, microstructure, and material on bone strength are at play, including aging, disease, or pre-clinical evaluation of therapies. If expanded in scope, this combination of experimental and finite element analysis could provide a systemic approach for characterizing biomechanical behavior from a variety of treatments and may provide new insight into other bone-altering treatments and diseases, specifically in animal models or cadaver studies where it is possible to combine microCT and mechanical testing—for example, on bone biopsies or cadaver tissue from radiation therapy patients.

In closure, this dissertation provided insight into the effect of treatment on bone strength and fracture risk, especially the role of radiation and osteoporosis drug therapies. The first study (Chapter 2) quantified the relative effects of treatment-induced changes in bone mass, microstructure, and tissue material behavior on bone strength with a unique combination of experimentation and microcomputed tomography-based nonlinear finite element analysis using a murine model of localized irradiation. The second study (Chapter 3) provided a mechanistic understanding of the link between bone strength changes and fracture risk thorough a theoretical

framework using reported data from osteoporosis treatments. The resulting insight from these studies can aid in understanding the underlying mechanisms influencing changes in bone strength and their connection to fracture risk, which may help to improve pre-clinical evaluation of therapies and their potential for fracture risk. Collectively, this dissertation answered fundamental open questions regarding treatment effects on bone strength/fracture risk and highlighted areas in need of further research.

In summary, this dissertation supports the following:

- Bone strength by FEA accurately measures biomechanically measured bone strength in rat vertebral bodies.
- Reductions in bone strength due to radiation therapy are dominated by reductions in bone mass (~60%) but are measurably affected by alterations in material properties (~24%) and microstructure (~16%).
- A theoretical framework of fracture risk prediction accurately demonstrates how small changes in bone strength—based on clinical measures of net 6%—can reduce the risk of fracture by approximately 40%.
- Risk reduction in a clinical trial should be greater if the trial is run on a healthier population.
- The theoretical framework of fracture risk prediction developed here is generalizable and should be customized with relevant data and applied more generally, i.e., to non-hip fractures, as well as other populations (i.e., men), and treatments (i.e., radiation therapy).
- More simulations need to be done to better characterize the mechanisms driving increased risk of fracture following radiation treatment.
- While radiation therapy independently diminishes bone strength, future work should explore the effect of multimodal therapy, including chemotherapy agents and/or antiresorptive drug treatments.
- The combination of finite element modeling and biomechanical testing is a useful evaluation tool in any application where the effects of mass, microstructure, and material on bone strength are at play, including aging, disease, or pre-clinical evaluation of therapies. Future work should apply this methodology to other areas, such as clinical radiation therapy through characterization of bone biopsies or cadaver tissue.

5 References

[1] National Cancer Institute, “Radiation Therapy and You,” *NIH Publ. No. 12-7157*, 2012.

[2] National Cancer Institute, “Cancer Statistics,” 2020. [Online]. Available: https://www.cancer.gov/about-cancer/understanding/statistics. [Accessed: 18-Mar-2021].

[3] K. D. Miller *et al.*, “Cancer treatment and survivorship statistics, 2016.,” *CA. Cancer J. Clin.*, vol. 66, no. 4, pp. 271–89, 2016.

[4] N. N. Baxter, E. B. Habermann, J. E. Tepper, S. B. Durham, and B. A. Virnig, “Risk of pelvic fractures in older women following pelvic irradiation,” *JAMA*, vol. 294, no. 20, pp. 2587–2593, 2005.

[5] V. Fusco *et al.*, “Insufficiency Fractures After Radiation Therapy: An Update,” *Curr. Radiol. Rep.*, vol. 6, no. 7, p. 21, 2018.

[6] S. P. Elliott, S. L. Jarosek, S. R. Alanee, B. R. Konety, K. E. Dusenbery, and B. A. Virnig, “Three-dimensional external beam radiotherapy for prostate cancer increases the risk of hip fracture,” *Cancer*, vol. 117, no. 19, pp. 4557–4565, 2011.

[7] S. J. Henley *et al.*, “Annual report to the nation on the status of cancer, part I: National cancer statistics,” *Cancer*, vol. 126, no. 10, pp. 2225–2249, 2020.

[8] R. L. Wei *et al.*, “Bone mineral density loss in thoracic and lumbar vertebrae following radiation for abdominal cancers,” *Radiother. Oncol.*, vol. 118, no. 3, pp. 430–436, 2016.

[9] S. K. Hui, L. Arentsen, A. Wilcox, R. Shanley, D. Yee, and R. Ghebre, “Spatial and temporal fracture pattern in breast and gynecologic cancer survivors,” *J. Cancer*, vol. 6, no. 1, pp. 66–69, 2015.

[10] G. Yaprak, C. Gemici, S. Temizkan, S. Ozdemir, B. C. Dogan, and O. O. Seseogullari, “Osteoporosis development and vertebral fractures after abdominal irradiation in patients with gastric cancer.,” *BMC Cancer*, vol. 18, no. 1, p. 972, Oct. 2018.

[11] H. Uezono *et al.*, “Pelvic insufficiency fracture after definitive radiotherapy for uterine cervical cancer: retrospective analysis of risk factors,” *J. Radiat. Res.*, vol. 54, no. 6, pp. 1102–1109, 2013.

[12] C. Okoukoni *et al.*, “Radiation-Induced Bone Toxicity,” *Curr. Stem Cell Reports*, vol. 3, no. 4, pp. 333–341, 2017.

[13] K. Otani *et al.*, “Risk factors for vertebral compression fractures in preoperative chemoradiotherapy with gemcitabine for pancreatic cancer,” *Radiother. Oncol.*, vol. 118, no. 3, pp. 424–429, 2016.

[14] Z. Chen *et al.*, “Fracture Risk Among Breast Cancer Survivors: Results from the Women’s

Health Initiative Observational Study," *Arch Intern Med*, vol. 165, no. 5, pp. 552–558, 2005.

[15] N. I. of H. O. and R. B. D. N. R. Center., "Osteoporosis Overview," 2018.

[16] O. Johnell and J. A. Kanis, "An estimate of the worldwide prevalence and disability associated with osteoporotic fractures.," *Osteoporos. Int.*, vol. 17, no. 12, pp. 1726–33, Dec. 2006.

[17] D. W. Dempster, "Osteoporosis and the burden of osteoporosis-related fractures.," *Am. J. Manag. Care*, vol. 17 Suppl 6, no. May 2011, pp. 164–169, 2011.

[18] C. M. Bartlow, K. A. Mann, T. A. Damron, and M. E. Oest, "Altered Mechanical Behavior of Demineralized Bone Following Therapeutic Radiation," *J. Orthop. Res.*, no. January, p. jor.24868, Sep. 2020.

[19] G. S. Mandair, M. E. Oest, K. A. Mann, M. D. Morris, T. A. Damron, and D. H. Kohn, "Radiation-induced changes to bone composition extend beyond periosteal bone," *Bone Reports*, vol. 12, no. March, p. 100262, 2020.

[20] M. E. Oest, C. G. Policastro, K. A. Mann, N. D. Zimmerman, and T. A. Damron, "Longitudinal Effects of Single Hindlimb Radiation Therapy on Bone Strength and Morphology at Local and Contralateral Sites," *J. Bone Miner. Res.*, vol. 33, no. 1, pp. 99–112, Jan. 2018.

[21] J. D. Wernle, T. A. Damron, M. J. Allen, and K. A. Mann, "Local irradiation alters bone morphology and increases bone fragility in a mouse model," *J. Biomech.*, vol. 43, no. 14, pp. 2738–2746, Oct. 2010.

[22] C. M. Bartlow, K. A. Mann, T. A. Damron, and M. E. Oest, "Limited field radiation therapy results in decreased bone fracture toughness in a murine model.," *PLoS One*, vol. 13, no. 10, p. e0204928, 2018.

[23] D. M. Black *et al.*, "Fracture risk reduction with alendronate in women with osteoporosis: The fracture intervention trial," *J. Clin. Endocrinol. Metab.*, vol. 85, no. 11, pp. 4118–4124, 2000.

[24] M. R. McClung *et al.*, "Odanacatib for the treatment of postmenopausal osteoporosis: results of the LOFT multicentre, randomised, double-blind, placebo-controlled trial and LOFT Extension study," *Lancet Diabetes Endocrinol.*, vol. 7, no. 12, pp. 899–911, 2019.

[25] D. M. Black *et al.*, "Randomised trial of effect of alendronate on risk of fracture in women with existing vertebral fractures," *Lancet*, vol. 348, no. 9041, pp. 1535–1541, 1996.

[26] M. L. Bouxsein *et al.*, "Change in Bone Density and Reduction in Fracture Risk: A Meta-Regression of Published Trials," *J. Bone Miner. Res.*, vol. 34, no. 4, pp. 632–642, 2019.

[27] T. M. Keaveny *et al.*, "Femoral bone strength and its relation to cortical and trabecular

changes after treatment with PTH, alendronate, and their combination as assessed by finite element analysis of quantitative CT scans," *J. Bone Miner. Res.*, vol. 23, no. 12, pp. 1974–1982, Dec. 2008.

[28] E. M. Lewiecki *et al.*, "Once-Monthly Oral Ibandronate Improves Biomechanical Determinants of Bone Strength in Women with Postmenopausal Osteoporosis," *J. Clin. Endocrinol. Metab.*, vol. 94, no. 1, pp. 171–180, 2009.

[29] K. Brixen *et al.*, "Bone density, turnover, and estimated strength in postmenopausal women treated with odanacatib: A randomized trial," *J. Clin. Endocrinol. Metab.*, vol. 98, no. 2, pp. 571–580, 2013.

[30] T. M. Keaveny *et al.*, "Femoral and vertebral strength improvements in postmenopausal women with osteoporosis treated with denosumab," *J. Bone Miner. Res.*, vol. 29, no. 1, pp. 158–165, Jan. 2014.

[31] B. Clarke, "Normal bone anatomy and physiology.," *Clin. J. Am. Soc. Nephrol.*, vol. 3 Suppl 3, pp. 131–139, 2008.

[32] J. M. Hughes *et al.*, "The Central Role of Osteocytes in the Four Adaptive Pathways of Bone's Mechanostat," *Exerc. Sport Sci. Rev.*, vol. 48, no. 3, pp. 140–148, 2020.

[33] R. O. Ritchie, "The conflicts between strength and toughness," *Nat. Mater.*, vol. 10, no. 11, pp. 817–822, 2011.

[34] S. Medical, "XtremeCT." [Online]. Available: http://www.scanco.ch/en/systems-solutions/preclinical/xtremect-preclinical.html. [Accessed: 15-Feb-2019].

[35] R. B. Martin, D. B. Burr, and N. A. Sharkey, *Skeletal Tissue Mechanics*. New York: Springer, 1998.

[36] T. M. Keaveny, E. F. Morgan, G. L. Niebur, and O. C. Yeh, "Biomechanics of Trabecular Bone," *Annu. Rev. Biomed. Eng.*, vol. 3, no. 1, pp. 307–333, Aug. 2001.

[37] L. Mosekilde, "Age-related changes in bone mass, structure, and strength - effects of loading," Steinkopff Verlag, 2000.

[38] M. Dalstra, R. Huiskes, A. Odgaard, and L. van Erning, "Mechanical and textural properties of pelvic trabecular bone," *J. Biomech.*, vol. 26, no. 4–5, pp. 523–535, Apr. 1993.

[39] L. F. Bonewald, "4. Osteocytes," in *Primer on the metabolic bone diseases and disorders of mineral metabolism.*, 2009, pp. 22–27.

[40] R. Florencio-Silva, G. R. da S. Sasso, E. Sasso-Cerri, M. J. Simões, and P. S. Cerri, "Biology of Bone Tissue: Structure, Function, and Factors That Influence Bone Cells," *Biomed Res. Int.*, vol. 2015, no. 6, pp. 1–17, 2015.

[41] S. L. Teitelbaum, “Bone Resorption by Osteoclasts,” *Science (80-.).*, vol. 289, no. 5484, pp. 1504–1508, Sep. 2000.

[42] W. J. Boyle, W. S. Simonet, and D. L. Lacey, “Osteoclast differentiation and activation.,” *Nature*, vol. 423, no. 6937, pp. 337–42, May 2003.

[43] T. Bellido, L. I. Plotkin, and A. Bruzzaniti, “Bone Cells,” in *Basic and Applied Bone Biology*, D. B. Burr and M. R. Allen, Eds. Elsevier, 2019, pp. 37–55.

[44] D. L. Bartel, D. T. Davy, and T. M. Keaveny, *Orthopaedic Biomechanics: Mechanics and Design in Musculoskeletal Systems*. Upper Saddle River: Pearson Prentice Hall, 2006.

[45] G. Osterhoff, E. F. Morgan, S. J. Shefelbine, L. Karim, L. M. McNamara, and P. Augat, “Bone mechanical properties and changes with osteoporosis,” *Injury*, vol. 47, pp. S11–S20, Jun. 2016.

[46] M. L. Bouxsein, “Determinants of skeletal fragility,” *Best Pract. Res. Clin. Rheumatol.*, vol. 19, no. 6, pp. 897–911, 2005.

[47] C. Jerome, B. Hoch, and C. S. Carlson, “Skeletal System,” in *Comparative Anatomy and Histology*, Elsevier, 2018, pp. 67–88.

[48] “Bone Remodeling Cycle,” 2005. [Online]. Available: http://ns.umich.edu/Releases/2005/Feb05/bone.html. [Accessed: 05-Apr-2021].

[49] M. R. Allen and D. B. Burr, “Bone Growth, Modeling, and Remodeling,” in *Basic and Applied Bone Biology*, Elsevier, 2019, pp. 85–100.

[50] J. A. Cauley, D. E. Thompson, K. C. Ensrud, J. C. Scott, and D. M. Black, “Risk of mortality following clinical fractures,” *Osteoporos. Int.*, vol. 11, no. 7, pp. 556–561, 2000.

[51] C. J. Hernandez and T. M. Keaveny, “A biomechanical perspective on bone quality,” *Bone*, vol. 39, no. 6, pp. 1173–1181, Dec. 2006.

[52] J. C. Lotz, T. N. Gerhart, and W. C. Hayes, “Mechanical properties of trabecular bone from the proximal femur: a quantitative CT study.,” *J. Comput. Assist. Tomogr.*, vol. 14, no. 1, pp. 107–14, 1990.

[53] D. L. Kopperdahl and T. M. Keaveny, “Yield strain behavior of trabecular bone,” *J. Biomech.*, vol. 31, no. 7, pp. 601–608, 1998.

[54] A. J. Fields, S. K. Eswaran, M. G. Jekir, and T. M. Keaveny, “Role of trabecular microarchitecture in whole-vertebral body biomechanical behavior,” *J. Bone Miner. Res.*, vol. 24, no. 9, pp. 1523–1530, 2009.

[55] I. Hvid, S. M. Bentzen, F. Linde, L. Mosekilde, and B. Pongsoipetch, “X-ray quantitative computed tomography: The relations to physical properties of proximal tibial trabecular

bone specimens," *J. Biomech.*, vol. 22, no. 8–9, pp. 837–844, 1989.

[56] R. W. McCalden *et al.*, "Age-Related Changes in the Tensile Properties of Cortical Bone," *J. Bone Jt. Surg.*, vol. 75, no. 8, pp. 1193–1205, 1993.

[57] E. M. Lewiecki *et al.*, "Osteoporotic fracture trends in a population of US managed care enrollees from 2007 to 2017," *Osteoporos. Int.*, vol. 31, no. 7, pp. 1299–1304, Jul. 2020.

[58] A. Singer *et al.*, "Burden of illness for osteoporotic fractures compared with other serious diseases among postmenopausal women in the United States," *Mayo Clin. Proc.*, vol. 90, no. 1, pp. 53–62, Jan. 2015.

[59] K. E. Ensrud, "Epidemiology of Fracture Risk With Advancing Age," *Journals Gerontol. Ser. A Biol. Sci. Med. Sci.*, vol. 68, no. 10, pp. 1236–1242, Oct. 2013.

[60] C. J. Hernandez and M. C. H. van der Meulen, "Understanding Bone Strength Is Not Enough," *J. Bone Miner. Res.*, vol. 32, no. 6, pp. 1157–1162, 2017.

[61] J. M. Wallace, *Skeletal Hard Tissue Biomechanics*, Second Edi. Elsevier Inc., 2019.

[62] J. H. Cole and M. C. H. Van Der Meulen, "Whole bone mechanics and bone quality," *Clin. Orthop. Relat. Res.*, vol. 469, no. 8, pp. 2139–2149, 2011.

[63] B. van Rietbergen, H. Weinans, R. Huiskes, and A. Odgaard, "A new method to determine trabecular bone elastic properties and loading using micromechanical finite-element models," *J. Biomech.*, vol. 28, no. 1, pp. 69–81, 1995.

[64] S. K. Eswaran, G. Bevill, P. Nagarathnam, M. R. Allen, D. B. Burr, and T. M. Keaveny, "Effects of suppression of bone turnover on cortical and trabecular load sharing in the canine vertebral body," *J. Biomech.*, vol. 42, no. 4, pp. 517–523, 2009.

[65] D. C. Lee, A. Varela, P. J. Kostenuik, M. S. Ominsky, and T. M. Keaveny, "Finite Element Analysis of Denosumab Treatment Effects on Vertebral Strength in Ovariectomized Cynomolgus Monkeys," *J. Bone Miner. Res.*, vol. 31, no. 8, pp. 1586–1595, 2016.

[66] G. Bevill, S. K. Eswaran, A. Gupta, P. Papadopoulos, and T. M. Keaveny, "Influence of bone volume fraction and architecture on computed large-deformation failure mechanisms in human trabecular bone," *Bone*, vol. 39, no. 6, pp. 1218–1225, 2006.

[67] S. Nawathe, H. Akhlaghpour, M. L. Bouxsein, and T. M. Keaveny, "Microstructural failure mechanisms in the human proximal femur for sideways fall loading," *J. Bone Miner. Res.*, vol. 29, no. 2, pp. 507–515, 2014.

[68] M. F. Adams, H. H. Bayraktar, T. M. Keaveny, and P. Papadopoulos, "Ultrascalable Implicit Finite Element Analyses in Solid Mechanics with over a Half a Billion Degrees of Freedom," in *Proceedings of the ACM/IEEE SC 2004 Conference: Bridging Communities*, 2004, p. 34.

[69] M. F. Adams, H. H. Bayraktar, T. M. Keaveny, and P. Papadopoulos, “Applications of Algebraic Multigrid to Large-Scale Finite Element Analysis of Whole Bone Micro-Mechanics on the IBM SP,” in *ACM/IEEE Conf. Supercomput.*, 2003.

[70] G. Bevill, S. K. Eswaran, F. Farahmand, and T. M. Keaveny, “The influence of boundary conditions and loading mode on high-resolution finite element-computed trabecular tissue properties,” *Bone*, vol. 44, no. 4, pp. 573–578, 2009.

[71] S. K. Easley, M. G. Jekir, A. J. Burghardt, M. Li, and T. M. Keaveny, “Contribution of the intra-specimen variations in tissue mineralization to PTH- and raloxifene-induced changes in stiffness of rat vertebrae.,” *Bone*, vol. 46, no. 4, pp. 1162–9, Apr. 2010.

[72] S. Sadoughi, A. vom Scheidt, S. Nawathe, S. Zhu, A. Moini, and T. M. Keaveny, “Effect of variations in tissue-level ductility on human vertebral strength,” *Bone*, vol. 137, no. May, p. 115445, 2020.

[73] A. J. Fields *et al.*, “Vertebral fragility and structural redundancy,” *J. Bone Miner. Res.*, vol. 27, no. 10, pp. 2152–2158, 2012.

[74] R. Baskar, K. A. Lee, R. Yeo, and K. W. Yeoh, “Cancer and Radiation Therapy: Current Advances and Future Directions,” *International Journal of Medical Sciences*, vol. 9, no. 3. Int J Med Sci, pp. 193–199, 27-Feb-2012.

[75] E. J. Hall and A. J. Giaccia, *Radiobiology for the Radiologist*. Lippincott Williams and Wilkins, 2019.

[76] D. Abshire and M. K. Lang, “The Evolution of Radiation Therapy in Treating Cancer,” *Seminars in Oncology Nursing*, vol. 34, no. 2. W.B. Saunders, pp. 151–157, 01-May-2018.

[77] J. E. Turner, *Atoms, Radiation, and Radiation Protection*. 2007.

[78] A. J. Mundt *et al.*, “Intensity-modulated whole pelvic radiotherapy in women with gynecologic malignancies,” *Int. J. Radiat. Oncol.*, vol. 52, no. 5, pp. 1330–1337, Apr. 2002.

[79] M. J. ZELEFSKY *et al.*, “HIGH DOSE RADIATION DELIVERED BY INTENSITY MODULATED CONFORMAL RADIOTHERAPY IMPROVES THE OUTCOME OF LOCALIZED PROSTATE CANCER,” *J. Urol.*, vol. 166, no. 3, pp. 876–881, Sep. 2001.

[80] R. Fonti, M. Conson, and S. Del Vecchio, “PET/CT in radiation oncology,” *Semin. Oncol.*, vol. 46, no. 3, pp. 202–209, Jun. 2019.

[81] A. M. Owrangi, P. B. Greer, and C. K. Glide-Hurst, “MRI-only treatment planning: benefits and challenges.,” *Phys. Med. Biol.*, vol. 63, no. 5, p. 05TR01, 2018.

[82] J. W. Kwon *et al.*, “Pelvic bone complications after radiation therapy of uterine cervical cancer: Evaluation with MRI,” *Am. J. Roentgenol.*, vol. 191, no. 4, pp. 987–994, 2008.

[83] Ş. Iğdem *et al.*, "Insufficiency Fractures After Pelvic Radiotherapy in Patients With Prostate Cancer," *Int. J. Radiat. Oncol. Biol. Phys.*, vol. 77, no. 3, pp. 818–823, 2010.

[84] J. Kim *et al.*, "Treatment outcomes after adjuvant radiotherapy following surgery for patients with stage i endometrial cancer," *Radiat. Oncol. J.*, vol. 34, no. 4, pp. 265–272, 2016.

[85] Q. Mehmood *et al.*, "Insufficiency fractures in patients treated with pelvic radiotherapy and chemotherapy for uterine and cervical cancer," *Eur. J. Cancer Care (Engl).*, vol. 23, no. 1, pp. 43–50, 2014.

[86] K. K. Shih *et al.*, "Pelvic insufficiency fractures in patients with cervical and endometrial cancer treated with postoperative pelvic radiation," *Gynecol. Oncol.*, vol. 128, no. 3, pp. 540–543, 2013.

[87] S.-H. Park, J.-C. Kim, J.-E. Lee, and I.-K. Park, "Pelvic insufficiency fracture after radiotherapy in patients with cervical cancer in the era of PET/CT," *Radiat. Oncol. J.*, vol. 29, no. 4, p. 269, 2011.

[88] K. M. Schmeler *et al.*, "Pelvic fractures after radiotherapy for cervical cancer: Implications for survivors," *Cancer*, vol. 116, no. 3, pp. 625–630, 2010.

[89] H. Yoshihara and D. Yoneoka, "Demographic epidemiology of unstable pelvic fracture in the United States from 2000 to 2009: Trends and in-hospital mortality," *J. Trauma Acute Care Surg.*, vol. 76, no. 2, pp. 380–385, 2014.

[90] V. Blomlie, E. K. Rofstad, K. Talle, K. Sundfør, M. Winderen, and H. H. Lien, "Incidence of radiation-induced insufficiency fractures of the female pelvis: evaluation with MR imaging.," *Am. J. Roentgenol.*, vol. 167, no. 5, pp. 1205–1210, Nov. 1996.

[91] M. P. Salcedo *et al.*, "Pelvic fractures and changes in bone mineral density after radiotherapy for cervical, endometrial, and vaginal cancer: A prospective study of 239 women," *Cancer*, vol. 126, no. 11, pp. 2607–2613, Jun. 2020.

[92] K. Yamamoto *et al.*, "Pelvic fractures after definitive and postoperative radiotherapy for cervical cancer: A retrospective analysis of risk factors.," *Gynecol. Oncol.*, vol. 147, no. 3, pp. 585–588, Dec. 2017.

[93] L. Bazire *et al.*, "Pelvic insufficiency fracture (PIF) incidence in patients treated with intensity-modulated radiation therapy (IMRT) for gynaecological or anal cancer: Single-institution experience and review of the literature," *Br. J. Radiol.*, vol. 90, no. 1073, 2017.

[94] A. Ramlov *et al.*, "Risk Factors for Pelvic Insufficiency Fractures in Locally Advanced Cervical Cancer Following Intensity Modulated Radiation Therapy," *Int. J. Radiat. Oncol. Biol. Phys.*, vol. 97, no. 5, pp. 1032–1039, 2017.

[95] D. Oh and S. J. Huh, "Insufficiency fracture after radiation therapy," *Radiat. Oncol. J.*, vol.

32, no. 4, pp. 213–220, 2014.

[96] L. G. Sapienza *et al.*, "Pelvic Insufficiency Fractures After External Beam Radiation Therapy for Gynecologic Cancers: A Meta-analysis and Meta-regression of 3929 Patients," *Int. J. Radiat. Oncol. Biol. Phys.*, vol. 106, no. 3, pp. 475–484, 2020.

[97] C. Cooper, "The crippling consequences of fractures and their impact on quality of life," *Am. J. Med.*, vol. 103, no. 2, pp. S12–S19, 1997.

[98] A. Sternheim *et al.*, "Internal fixation of radiation-induced pathological fractures of the femur has a high rate of failure," *Bone Joint J.*, vol. 95-B, no. 8, pp. 1144–1148, Aug. 2013.

[99] H. Abe, M. Nakamura, S. Takahashi, S. Maruoka, Y. Ogawa, and K. Sakamoto, "Radiation-induced insufficiency fractures of the pelvis: Evaluation with 99mTc-methylene diphosphonate scintigraphy," *Am. J. Roentgenol.*, vol. 158, no. 3, pp. 599–602, 1992.

[100] S. K. Hui *et al.*, "Longitudinal assessment of bone loss from diagnostic computed tomography scans in gynecologic cancer patients treated with chemotherapy and radiation," *Am. J. Obstet. Gynecol.*, vol. 203, no. 4, pp. 353.e1-353.e7, 2010.

[101] S. Dhakal, J. Chen, S. McCance, R. Rosier, R. O'Keefe, and L. S. Constine, "Bone density changes after radiation for extremity sarcomas: Exploring the etiology of pathologic fractures," *Int. J. Radiat. Oncol. Biol. Phys.*, vol. 80, no. 4, pp. 1158–1163, 2011.

[102] H. H. W. Chen, B. F. Lee, H. R. Guo, W. R. Su, and N. T. Chiu, "Changes in bone mineral density of lumbar spine after pelvic radiotherapy.," *Radiother. Oncol.*, vol. 62, no. 2, pp. 239–242, 2002.

[103] M. E. Rodríguez-Ruiz *et al.*, "Pathological vertebral fracture after stereotactic body radiation therapy for lung metastases. Case report and literature review," *Radiat. Oncol.*, vol. 7, no. 1, pp. 1–6, 2012.

[104] International Commission on Radiological Protection., "ICRP Statement on Tissue Reactions / Early and Late Effects of Radiation in Normal Tissues and Organs – Threshold Doses for Tissue Reactions in a Radiation Protection Context. ICRP Publication 118.," *Ann. ICRP*, vol. 41, no. 1/2, 2012.

[105] J. S. Willey, S. A. J. Lloyd, and T. A. Bateman, "Radiation Therapy-Induced Osteoporosis," in *Primer on the Metabolic Bone Diseases and Disorders of Mineral Metabolism, Eighth Edition*, 2013, pp. 728–733.

[106] X. Cao *et al.*, "Irradiation induces bone injury by damaging bone marrow microenvironment for stem cells," *Proc. Natl. Acad. Sci. U. S. A.*, vol. 108, no. 4, pp. 1609–1614, Jan. 2011.

[107] T. J. Gal, T. Munoz-Antonia, C. A. Muro-Cacho, and D. W. Klotch, "Radiation Effects on Osteoblasts In Vitro," *Arch. Otolaryngol. Neck Surg.*, vol. 126, no. 9, p. 1124, Sep. 2000.

[108] K. H. Szymczyk, I. M. Shapiro, and C. S. Adams, “Ionizing radiation sensitizes bone cells to apoptosis.,” *Bone*, vol. 34, no. 1, pp. 148–56, Jan. 2004.

[109] M. E. Dudziak *et al.*, “The effects of ionizing radiation on osteoblast-like cells in vitro.,” *Plast. Reconstr. Surg.*, vol. 106, no. 5, pp. 1049–61, Oct. 2000.

[110] T. Sakurai, Y. Sawada, M. Yoshimoto, M. Kawai, and J. Miyakoshi, “Radiation-induced reduction of osteoblast differentiation in C2C12 cells.,” *J. Radiat. Res.*, vol. 48, no. 6, pp. 515–21, Nov. 2007.

[111] M. E. Oest, V. Franken, T. Kuchera, J. Strauss, and T. A. Damron, “Long-term loss of osteoclasts and unopposed cortical mineral apposition following limited field irradiation,” *J. Orthop. Res.*, vol. 33, no. 3, pp. 334–342, Mar. 2015.

[112] M. E. Oest, K. A. Mann, N. D. Zimmerman, and T. A. Damron, “Parathyroid Hormone (1–34) Transiently Protects Against Radiation-Induced Bone Fragility,” *Calcif. Tissue Int.*, vol. 98, no. 6, pp. 619–630, 2016.

[113] L. E. Wright *et al.*, “Single-Limb Irradiation Induces Local and Systemic Bone Loss in a Murine Model,” *J. Bone Miner. Res.*, vol. 30, no. 7, pp. 1268–1279, Jul. 2015.

[114] B. Gong, M. E. Oest, K. A. Mann, T. A. Damron, and M. D. Morris, “Raman spectroscopy demonstrates prolonged alteration of bone chemical composition following extremity localized irradiation,” *Bone*, vol. 57, no. 1, pp. 252–258, 2013.

[115] M. E. Oest and T. A. Damron, “Focal Therapeutic Irradiation Induces an Early Transient Increase in Bone Glycation,” *Radiat. Res.*, vol. 181, no. 4, pp. 439–443, Apr. 2014.

[116] M. E. Oest *et al.*, “Parathyroid hormone attenuates radiation-induced increases in collagen crosslink ratio at periosteal surfaces of mouse tibia,” *Bone*, vol. 86, pp. 91–97, 2016.

[117] J. S. Willey *et al.*, “Risedronate prevents early radiation-induced osteoporosis in mice at multiple skeletal locations,” *Bone*, vol. 46, no. 1, pp. 101–111, 2010.

[118] M. M. Nyaruba, I. Yamamoto, H. Kimura, and R. Morita, “Bone fragility induced by X-ray irradiation in relation to cortical bone-mineral content.,” *Acta radiol.*, vol. 39, no. 1, pp. 43–46, 1998.

[119] D. Saul and M. T. Drake, “Update on Approved Osteoporosis Therapies Including Combination and Sequential Use of Agents,” *Endocrinol. Metab. Clin. North Am.*, vol. 50, no. 2, pp. 179–191, Jun. 2021.

[120] N. E. Lane and A. Kelman, “A review of anabolic therapies for osteoporosis.,” *Arthritis Res. Ther.*, vol. 5, no. 5, pp. 214–22, 2003.

[121] S. R. Cummings *et al.*, “Denosumab for prevention of fractures in postmenopausal women with osteoporosis,” *Obstet. Gynecol. Surv.*, vol. 64, no. 12, pp. 805–807, 2009.

[122] D. M. Black *et al.*, "Once-Yearly Zoledronic Acid for Treatment of Postmenopausal Osteoporosis," *N. Engl. J. Med.*, vol. 356, no. 18, pp. 1809–1822, May 2007.

[123] C. H. Chesnut *et al.*, "Effects of Oral Ibandronate Administered Daily or Intermittently on Fracture Risk in Postmenopausal Osteoporosis," *J. Bone Miner. Res.*, vol. 19, no. 8, pp. 1241–1249, Aug. 2004.

[124] J.-Y. Reginster *et al.*, "Randomized Trial of the Effects of Risedronate on Vertebral Fractures in Women with Established Postmenopausal Osteoporosis," *Osteoporos. Int.*, vol. 11, no. 1, pp. 83–91, Jan. 2000.

[125] D. Jia, D. Gaddy, L. J. Suva, and P. M. Corry, "Rapid Loss of Bone Mass and Strength in Mice after Abdominal Irradiation," *Radiat. Res.*, vol. 176, no. 5, pp. 624–635, 2011.

[126] M. M. Pendleton *et al.*, "Effects of ex vivo ionizing radiation on collagen structure and whole-bone mechanical properties of mouse vertebrae," *Bone*, vol. 128, no. August, p. 115043, Nov. 2019.

[127] M. M. Pendleton, S. Sadoughi, A. Li, G. D. O'Connell, J. S. Alwood, and T. M. Keaveny, "High-precision method for cyclic loading of small-animal vertebrae to assess bone quality," *Bone Reports*, vol. 9, no. October, pp. 165–172, 2018.

[128] M. L. Bouxsein, S. K. Boyd, B. A. Christiansen, R. E. Guldberg, K. J. Jepsen, and R. Müller, "Guidelines for assessment of bone microstructure in rodents using micro-computed tomography," *J. Bone Miner. Res.*, vol. 25, no. 7, pp. 1468–1486, 2010.

[129] E. F. Morgan, H. H. Bayraktar, and T. M. Keaveny, "Trabecular bone modulus-density relationships depend on anatomic site," *J. Biomech.*, vol. 36, no. 7, pp. 897–904, 2003.

[130] S. J. Hollister, J. M. Brennan, and N. Kikuchi, "A homogenization sampling procedure for calculating trabecular bone effective stiffness and tissue level stress," *J. Biomech.*, 1994.

[131] H. H. Bayraktar, E. F. Morgan, G. L. Niebur, G. E. Morris, E. K. Wong, and T. M. Keaveny, "Comparison of the elastic and yield properties of human femoral trabecular and cortical bone tissue," *J. Biomech.*, vol. 37, no. 1, pp. 27–35, 2004.

[132] S. Dhesy-Thind *et al.*, "Use of Adjuvant Bisphosphonates and Other Bone-Modifying Agents in Breast Cancer: A Cancer Care Ontario and American Society of Clinical Oncology Clinical Practice Guideline," *J. Clin. Oncol.*, vol. 35, no. 18, pp. 2062–2081, Jun. 2017.

[133] S. A. Arrington, E. R. Fisher, G. E. Willick, K. A. Mann, and M. J. Allen, "Anabolic and antiresorptive drugs improve trabecular microarchitecture and reduce fracture risk following radiation therapy.," *Calcif. Tissue Int.*, vol. 87, no. 3, pp. 263–272, 2010.

[134] S. A. Arrington, T. A. Damron, K. A. Mann, and M. J. Allen, "Concurrent administration of zoledronic acid and irradiation leads to improved bone density, biomechanical strength,

and microarchitecture in a mouse model of tumor-induced osteolysis," *J. Surg. Oncol.*, vol. 97, no. 3, pp. 284–290, 2008.

[135] N. Kohno *et al.*, "Zoledronic acid significantly reduces skeletal complications compared with placebo in Japanese women with bone metastases from breast cancer: A randomized, placebo-controlled trial," *J. Clin. Oncol.*, vol. 23, no. 15, pp. 3314–3321, 2005.

[136] M. Tolia *et al.*, "The Key Role of Bisphosphonates in the Supportive Care of Cancer Patients," *Anticancer Res.*, vol. 34, no. 1A, pp. 23–37, 2014.

[137] H. C. Almstedt *et al.*, "Combined aerobic and resistance training improves bone health of female cancer survivors," *Bone Reports*, vol. 5, pp. 274–279, Dec. 2016.

[138] A.-S. Schreurs *et al.*, "Dried plum diet protects from bone loss caused by ionizing radiation," *Sci. Rep.*, vol. 6, no. November 2015, pp. 1–11, 2016.

[139] M. D. Willinghamm, M. D. Brodt, K. L. Lee, A. L. Stephens, J. Ye, and M. J. Silva, "Age-Related Changes in Bone Structure and Strength in Female and Male BALB/c Mice," *Calcif. Tissue Int.*, vol. 86, no. 6, pp. 470–483, Jun. 2010.

[140] D. V. Agoston, "How to translate time? The temporal aspect of human and rodent biology," *Front. Neurol.*, vol. 8, no. MAR, pp. 17–19, 2017.

[141] S. Schultze-Mosgau *et al.*, "Expression of bone morphogenic protein 2/4, transforming growth factor-β1, and bone matrix protein expression in healing area between vascular tibia grafts and irradiated bone—experimental model of osteonecrosis," *Int. J. Radiat. Oncol.*, vol. 61, no. 4, pp. 1189–1196, Mar. 2005.

[142] G. J. Kazakia, A. J. Burghardt, S. Cheung, and S. Majumdar, "Assessment of bone tissue mineralization by conventional x-ray microcomputed tomography: comparison with synchrotron radiation microcomputed tomography and ash measurements.," *Med. Phys.*, vol. 35, no. 7, pp. 3170–9, Jul. 2008.

[143] N. Kaynia, E. Soohoo, T. M. Keaveny, and G. J. Kazakia, "Effect of Intraspecimen Spatial Variation in Tissue Mineral Density on the Apparent Stiffness of Trabecular Bone," *J. Biomech. Eng.*, vol. 137, no. 1, pp. 1–6, 2015.

[144] T. Coughlan and F. Dockery, "Osteoporosis and fracture risk in older people.," *Clin. Med.*, vol. 14, no. 2, pp. 187–91, Apr. 2014.

[145] J. D. Adachi *et al.*, "Impact of Prevalent Fractures on Quality of Life: Baseline Results From the Global Longitudinal Study of Osteoporosis in Women," *Mayo Clin. Proc.*, vol. 85, no. 9, pp. 806–813, Sep. 2010.

[146] W. He, D. Goodkind, and P. R. Kowal, "An Aging World: 2015," Washington D.C., 2016.

[147] J. A. Cauley, "Public Health Impact of Osteoporosis," *Journals Gerontol. Ser. A Biol. Sci.*

Med. Sci., vol. 68, no. 10, pp. 1243–1251, Oct. 2013.

[148] M. R. McClung *et al.*, "Effect of Risedronate on the Risk of Hip Fracture in Elderly Women," *Obstet. Gynecol. Surv.*, vol. 56, no. 7, pp. 423–424, 2001.

[149] D. M. Black *et al.*, "Treatment-related changes in bone mineral density as a surrogate biomarker for fracture risk reduction: meta-regression analyses of individual patient data from multiple randomised controlled trials," *Lancet Diabetes Endocrinol.*, vol. 8, no. 8, pp. 672–682, 2020.

[150] J. D. Currey, "Stress Concentrations in Bone," *J. Cell Sci.*, vol. s3-103, no. 61, pp. 111–133, 1962.

[151] T. M. Keaveny and M. L. Bouxsein, "Theoretical implications of the biomechanical fracture threshold.," *J. Bone Miner. Res.*, vol. 23, no. 10, pp. 1541–1547, 2008.

[152] S. K. Eswaran, M. R. Allen, D. B. Burr, and T. M. Keaveny, "A computational assessment of the independent contribution of changes in canine trabecular bone volume fraction and microarchitecture to increased bone strength with suppression of bone turnover," *J. Biomech.*, vol. 40, no. 15, pp. 3424–3431, Jan. 2007.

[153] S. K. Easley, M. T. Chang, D. Shindich, C. J. Hernandez, and T. M. Keaveny, "Biomechanical effects of simulated resorption cavities in cancellous bone across a wide range of bone volume fractions," *J. Bone Miner. Res.*, vol. 27, no. 9, pp. 1927–1935, Sep. 2012.

[154] C. J. Hernandez, A. Gupta, and T. M. Keaveny, "A Biomechanical Analysis of the Effects of Resorption Cavities on Cancellous Bone Strength," *J. Bone Miner. Res.*, vol. 21, no. 8, pp. 1248–1255, May 2006.

[155] N. Hong, D. C. Lee, S. Khosla, T. M. Keaveny, and Y. Rhee, "Comparison of Vertebral and Femoral Strength Between White and Asian Adults Using Finite Element Analysis of Computed Tomography Scans," *J. Bone Miner. Res.*, vol. 35, no. 12, pp. 2345–2354, 2020.

[156] US Department of Health and Human Services, *Bone Health and Osteoporosis: A Report of the Surgeon General*. Rockville, MD: U.S. Department of Health and Human Services, Office of the Surgeon General, 2004.

[157] A. L. Adams *et al.*, "Osteoporosis and Hip Fracture Risk From Routine Computed Tomography Scans: The Fracture, Osteoporosis, and CT Utilization Study (FOCUS)," *J. Bone Miner. Res.*, vol. 33, no. 7, pp. 1291–1301, Jul. 2018.

[158] S. N. Robinovitch, T. A. McMahon, and W. C. Hayes, "Force attenuation in trochanteric soft tissues during impact from a fall," *J. Orthop. Res.*, vol. 13, no. 6, pp. 956–962, Nov. 1995.

[159] A. Qaseem, M. A. Forciea, R. M. McLean, and T. D. Denberg, "Treatment of low bone

density or osteoporosis to prevent fractures in men and women: A clinical practice guideline update from the American college of physicians," *Ann. Intern. Med.*, vol. 166, no. 11, pp. 818–839, 2017.

[160] O. Johnell *et al.*, "Predictive value of BMD for hip and other fractures," *J. Bone Miner. Res.*, vol. 20, no. 7, pp. 1185–1194, 2005.

[161] M. R. McClung *et al.*, "Effect of denosumab treatment on the risk of fractures in subgroups of women with postmenopausal osteoporosis," *J. Bone Miner. Res.*, vol. 27, no. 1, pp. 211–218, 2012.

[162] S. R. Cummings *et al.*, "Effect of alendronate on risk of fracture in women with low bone density but without vertebral fractures. Results from the fracture intervention trial," *J. Am. Med. Assoc.*, vol. 280, no. 24, pp. 2077–2082, 1998.

[163] S. J. Jacobsen, J. Goldberg, T. P. Miles, J. A. Brody, W. Stiers, and A. A. Rimm, "Hip fracture incidence among the old and very old: a population-based study of 745,435 cases.," *Am. J. Public Health*, vol. 80, no. 7, pp. 871–3, Jul. 1990.

[164] S. R. Cummings and L. J. Melton, "Epidemiology and outcomes of osteoporotic fractures.," *Lancet (London, England)*, vol. 359, no. 9319, pp. 1761–7, May 2002.

[165] D. S. Zingmond, N. F. Soohoo, and S. L. Silverman, "The role of socioeconomic status on hip fracture.," *Osteoporos. Int.*, vol. 17, no. 10, pp. 1562–8, Oct. 2006.

[166] W. E. Bacon and W. C. Hadden, "Occurrence of hip fractures and socioeconomic position.," *J. Aging Health*, vol. 12, no. 2, pp. 193–203, May 2000.

[167] M. Herrera-Marschitz, H. Utsumi, and U. Ungerstedt, "Scoliosis in rats with experimentally-induced hemiparkinsonism: dependence upon striatal dopamine denervation.," *J. Neurol. Neurosurg. Psychiatry*, vol. 53, no. 1, pp. 39–43, Jan. 1990.

[168] L. A. Pruitt and A. M. Chakravartula, *Mechanics of Biomaterials: Fundamental Principles for Implant Design*. Cambridge University Press, 2011.

6 Appendices

6.1 Fracture Risk Modeling – Definition of Key Variables

Abbreviation	Name	Description	Calculation
P(Fracture)	Probability of Fracture	Likelihood of fracture on its own	$\frac{\#\ fractures}{\#\ people}$
$P(Fracture)_{TRT}$	Probability of Fracture in the treated group	Likelihood of fracture on its own in the treated group	$\frac{\#\ fractures\ in\ TRT}{\#\ people\ in\ TRT}$
$P(Fracture)_{PLB}$	Probability of Fracture in the placebo group	Likelihood of fracture on its own in the placebo group	$\frac{\#\ fractures\ in\ PLB}{\#\ people\ in\ PLB}$
P(Fall)	Probability of Falling	Likelihood of falling on its own	$\frac{\#\ falls}{\#\ people}$
P(Fracture | Fall)	Probability of Fracture given Falling	Likelihood of Fracture occurring given that a Fall has occurred	
P(Fall | Fracture)	Probability of Falling given Fracture	Likelihood of Falling given that the individual has Fractured	$\frac{P(Fracture \mid Fall)\ \times\ P(Fall)}{P(Fall \mid Fracture)}$

RR	Relative Risk or Risk Ratio	Ratio of the probability of a Fracture in the Treatment group to the probability of a Fracture in the Placebo group When RR > 1, treatment increases the likelihood of fracture When RR < 1, treatment decreases the likelihood of fracture	$\frac{P(Fracture)_{TRT}}{P(Fracture)_{PLB}} = \frac{P(Fracture \mid Fall)_{TRT} \times P(Fall)_{TRT} \times P(Fall \mid Fracture)_{PLB}}{P(Fall \mid Fracture)_{TRT} \times P(Fracture \mid Fall)_{PLB} \times P(Fall)_{PLB}}$ Simplify via two assumptions: (3) the probability of fall is equivalent for both TRT and PLB, i.e. $P(Fall)_{TRT} = P(Fall)_{PLB}$ (4) the probability of falling given a fracture is equivalent for both TRT and PLB: $P(Fall \mid Fracture)_{TRT} = P(Fall \mid Fracture)_{PLB}$ Final simplified formula: $\frac{P(Fracture)_{TRT}}{P(Fracture)_{PLB}} = \frac{P(Fracture \mid Fall)_{TRT}}{P(Fracture \mid Fall)_{PLB}}$
RR (%)	Risk Reduction (%)	Reduction in risk of fracture for patients in the treatment group	$\left(1 - \frac{P(Fracture)_{TRT}}{P(Fracture)_{PLB}}\right) \times 100\% = Risk\ Reduction$

6.2 Standard Operating Procedures

6.2.1 In vivo X-Ray Irradiation at X-RAD 320 in Li Ka Shing

University of California, Berkeley

Berkeley Biomechanics Lab

Standard Operating Procedure

In vivo X-Ray Irradiation at X-RAD 320 in Li Ka Shing

SOP, Version 2

Date: 07/18/2019

Author(s): Shannon Emerzian

Principal Investigator: Tony M. Keaveny

Summary: This protocol outlines the steps used to irradiate small animals (mice or rats) with X-rays using the X-RAD 320 in B140 Li Ka Shing (LKS). Contact Mike Wendland who manages the Berkeley Preclinical Imaging Core (BPIC) at LKS (http://preclinical.ls.berkeley.edu/index.html). The X-RAD is a self-contained X-ray irradiation system designed for use in biology and medical research to deliver precise X-ray dosages in a radiation enclosure.

Note: Before you begin

- Before using the X-RAD device, you must be trained by Mike Wendland. Training consists of two training sessions (~1-1.5 hours each) and a written exam. Once you pass the exam, you will be added the RUA for the device, and will be able to request access to the building and room with irradiator (B140).
- Before working with live animals, you must submit an Animal Use Protocol to the Animal Care and Use Committee at UC Berkeley (https://acuc.berkeley.edu/about.html). The protocol must detail the procedure to be performed and must be approved by the institutional animal care and use committee (IACUC) before the study can begin.

Key Words: ionizing radiation, X-ray, in vivo, mouse, rat

Materials:

- X-RAD 320 (B140 LKS)
- Anesthesia unit with rat box/nose cone (rented from OLAC)
- Isoflurane scavenging unit (Mike Wendland)
- Ophthalmic ointment
- Dosimeter

Steps:

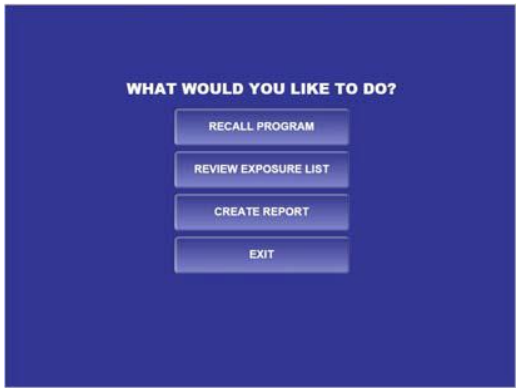
1. Put on your dosimeter (ring).
2. Turn on the Geiger counter (usually stored in the cabinet next to the X-RAD) and place to the right of the cabinet.
3. Change the filter to F2.
    a. When opening the door to the X-RAD, ensure that your dosimetry ring is on the hand you plan to put inside of the machine. (Generally – open the door with your left hand, hold Geiger counter in right hand and have dosimeter on this hand as well). Upon first opening the door, check for hotspots with Geiger counter.
    b. If safe, switch to Filter 2 (F2)
        i. Note: This filter is more radiodense; it narrows the spectrum and shifts the median to higher energy – better for live animal experiments. F2 = 1.5mm Al, 0.25mm Cu, 0.75mm Sn (Half Value Layer = 3.7mm Cu)
4. Get key for X-RAD from the cabinet; turn key-operated switch (bottom right in Figure below) of the TouchRAD control console from OFF to STAND BY.



5. Once initialization process has completed, login (see Figure below).
    a. Username and password to be assigned upon completion of exam.
        i. Username: ShannonE
        ii. Password: bioMech18



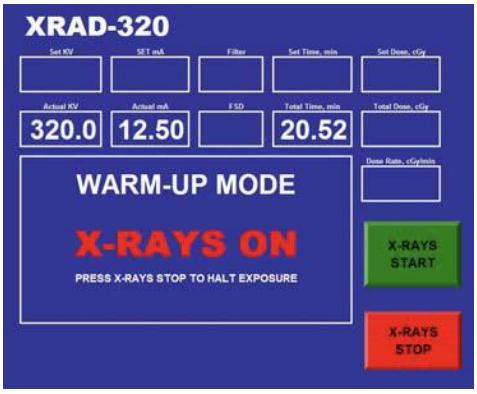
6. Once logged in, the Main Menu window will appear (see below).



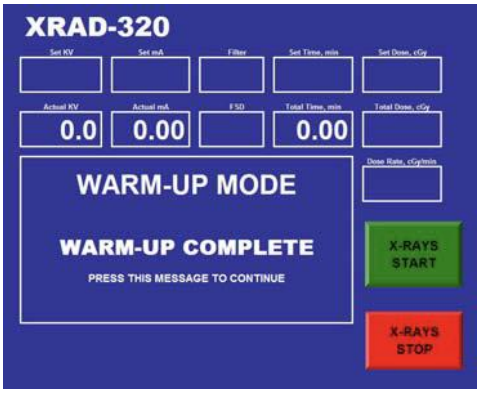
7. Turn key to ON
8. Select "Recall Program", and then Program 12. Press Continue.
    a. Program 12 details:
        i. Mode V = variable; we can input the dose (in cGy)
        ii. SSD (sample to source distance) = 50cm
        iii. 320 kV
        iv. 12.5 mA
9. **Warm-Up** (usually 15-20 minutes). If warm-up is necessary, the normal operating screen will be replaced with the screen below.
    a. Note: Warm-up refers to the X-ray tube conditioning process that is required for the X-RAD system to operate reliably. This automated process detects when a warm-up is necessary and calculates the appropriate period to perform it. Warm-up must be completed prior to performing normal exposures.
    b. Important: Specimens must not be inserted into the cabinet prior to warm-up completion. X-rays are produced during warm-up.



    c. To begin warm-up, touch X-RAYS START. The following screen will be displayed:

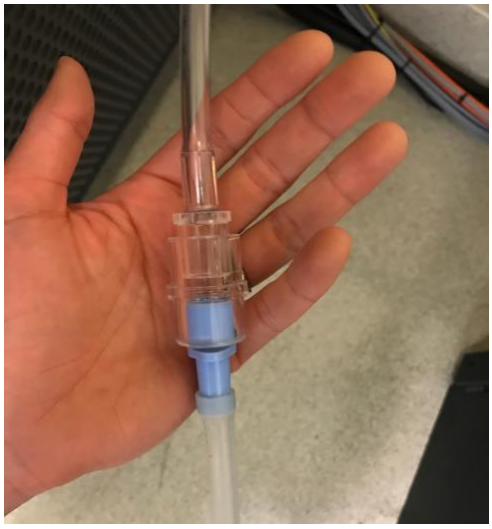


d. After a few seconds, the yellow X-RAYS ON lamp on the control panel will illuminate, as well as the X-RAYS ON light over the X-RAD cabinet. In addition, values for Actual kV and Actual mA will be displayed, and the Total Time remaining will count down.
e. Once complete, the unit will automatically stop X-ray generation and display the following screen:



f. Once the warm-up is complete, it will not be required until the next 8 hours of non-operation.
g. PRESS CONTINUE
h. Confirm that the filter selected and the filter displayed (FSD) are correct. (F2)
i. Set dose (in cGy; recall 1 Gy = 100 cGy).
j. Press CONTINUE

10. Set up room B140
    a. Anesthesia
        i. Connect isoflurane unit to the clear tubing on the right-hand side of the XRAD. See image of connector, below (tubing to XRAD at top, tubing to anesthesia unit at bottom):



ii. Put acrylic sheet or Tupperware inside machine and line with paper towels (to hold animal during procedure).
iii. Weigh scavenging units and record.
iv. Connect the nose cone to the isoflurane inlet tubing inside of the XRAD. Connect scavenging unit (stored in cabinet above the sink) to the exhaust of the nose cone. See below:





v. Put rat anesthesia box in the hood. Connect second isoflurane line to the rat anesthesia box.
vi. Check isoflurane and oxygen levels. Ensure they are sufficient.

b. Recovery cage
   i. Set up small rat cage in hood as recovery cage.
   ii. Activate HotHands hand warmer (or equivalent). Place under the recovery cage on one side.

11. ANIMAL PREP – IRRADIATION GROUP
    a. Anesthetize with isoflurane gas

i. Place animal home cage in hood.
ii. Ensure line to the rat anesthetic box is open; close line to XRAD.
iii. Start flow of oxygen at 1L.
iv. Move animal from home cage to anesthesia box.
v. Turn on **isoflurane at 5% to induce anesthesia**. Animal should lose consciousness slowly. Wait until animal appears to be fully unconscious and is breathing slowly and steadily before removing from anesthesia box.
vi. Pick up animal and check for blink reflex. If no blink reflex is present, apply **ophthalmic ointment**. Note: failure to apply may result in irritation, infection, and corneal ulcers.
vii. Check for **toe pinch reflex**. Take the animal's paw between the pad of your thumb and index finger and pinch firmly, but not so hard as to hurt the animal. If the animal withdraws the foot, it is still able to feel pain and you should re-dose with anesthesia. If there is no response, continue.
viii. Quickly **weigh** animal and record in data sheet.
ix. Switch isoflurane flow line to XRAD; close line to box.
x. Place animal in XRAD on acrylic sheet and put animal in nose cone. Maintain anesthesia with ~2-3% isoflurane (adjust as needed).
xi. Monitor for a minute or two to ensure anesthesia is maintained and animal is breathing slowly and steadily. Throughout anesthesia, monitor respiratory rate and skin color.

b. Shield
   i. Collimate the X-rays using the collimator in the XRAD. Focus area to lumbar spine (below rib cage, top of pelvis). See below:

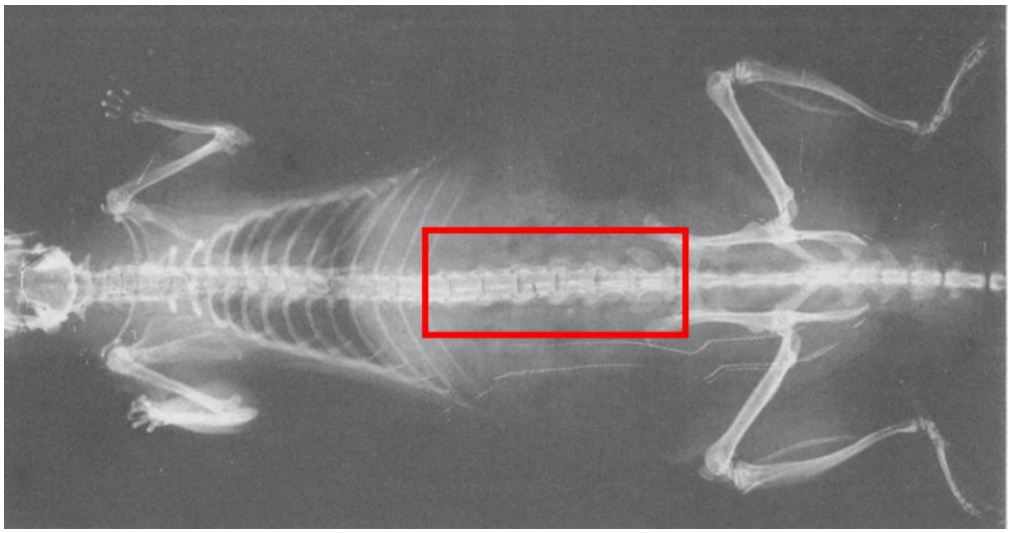


Figure: Dorsal view of rat with target treatment area in red; image adapted from [167]

c. Close XRAD door.
d. Perform exposure
   i. Press X-RAYS START to begin the exposure. The following screen will be displayed.



ii. Note: in the past the dose rate was around 95 cGy/min (~1 Gy/min)
iii. After a few seconds, the yellow X-RAYS ON lamp on the control panel will illuminate, as well as the X-RAYS ON light over the X-RAD cabinet. In addition, values for Actual kV and Actual mA will be displayed, and the Total Time remaining will count down.
iv. Step outside room until dosage is complete.
v. Once exposure is complete, remove animal from XRAD and place in recovery cage.

12. ANIMAL PREP - CONTROL GROUP
    a. Anesthetize with isoflurane gas
        i. Place animal home cage in hood.
        ii. Ensure line to the rat anesthetic box is open; close line to XRAD.
        iii. Start flow of oxygen at 1L.
        iv. Move animal from home cage to anesthesia box.
        v. Turn on **isoflurane at 5% to induce anesthesia**. Animal should lose consciousness slowly. Wait until animal appears to be fully unconscious and is breathing slowly and steadily before removing from anesthesia box.
        vi. Pick up animal and check for blink reflex. If no blink reflex is present, apply **ophthalmic ointment**. Note: failure to apply may result in irritation, infection, and corneal ulcers.
        vii. Check for **toe pinch reflex**. Take the animal's paw between the pad of your thumb and index finger and pinch firmly, but not so hard as to hurt the animal. If the animal withdraws the foot, it is still able to feel pain and you should re-dose with anesthesia. If there is no response, continue.
        viii. Quickly **weigh** animal and record in data sheet.
        ix. Switch isoflurane flow line to nose cone; close line to box.
        x. Place animal in nose cone. Maintain anesthesia with ~2-3% isoflurane (adjust as needed) for a time that matches the duration of anesthesia for irradiation.
        xi. Throughout anesthesia, monitor respiratory rate, pedal reflex, and skin color.
        xii. Once anesthesia time is complete, place animal in recovery cage

13. Recover
    a. Place animal in recovery cage on heat source. Maintain in recovery cage until fully awake and ambulatory. Once fully recovered, return to home cage.
    b. While animal recovers, move on to next animal (return to step 11 and repeat).
    c. When finished with study, proceed to step 14.
14. Shut off machine
    a. Hit “Exit” as many times as it pops up
    b. Once back to login screen, turn key to “OFF”
    c. Turn off Giegercounter; return it and the machine key and dosimetry ring to cabinet above sink.
15. IF THERE IS AN ERROR
    a. Cooling system error
        i. To reset, turn off and turn back on again
    b. Arcing error
        i. If it stops warmup midway, press “clear” and then restart warmup
        ii. If it fails 3x or more, you’ll need to do a hard shut off and turn on again

6.2.2 Rat Dissection and Cleaning: Vertebrae + Femur

University of California, Berkeley
Berkeley Biomechanics Lab
Standard Operating Procedure

Rat Dissection and Cleaning: Vertebrae + Femur

SOP, Version 1
Date: 01/07/2020

Author(s): Shannon Emerzian
Principal Investigator: Tony M. Keaveny

Summary: This protocol outlines the steps to dissect the vertebrae femur from a rat.
Key Words: dissection, murine, vertebra
Materials:

- KimWipes
- Gauze
- Ziplock bags (storage)
- 1X PBS
- 70% ethanol
- Forceps
- Scalpel (blade #22)
- Sharp-pointed dissecting scissors
- Dissection pads (absorbent blue pads)
- Biohazardous waste bag (red)

Equipment:

- N/A

Procedure:

1. Setup
    1.1. If frozen (-20°C), thaw before dissection (*Note: ~ 36-48 hours*)
        1.1.1. Thaw in the refrigerator (4°C) at least 24-36 hours prior to dissection. Keep carcass in its storage plastic bag during thaw.
        1.1.2. Once carcass is mostly thawed (i.e., joints are moveable, skin/muscles are soft), put rat in its storage bag into a separate outer plastic bag (Note: a double layer of plastic bags will help to prevent water from entering storage bag). Submerge this bag into a tub of cool water for ~1 hour.

1.1.3. Rest on the counter to allow rat to come to room temperature while you set up (~30 minutes)

1.2. Place absorbent pad under the work area (white side up).

1.3. Label Ziploc bags (one small bag per each vertebra, plus one larger bag to keep all vertebrae together) using a permanent marker.

1.4. Set up workstation with forceps (fine-tipped and roughened edge), scalpel (with spare #22 blades nearby) dissection scissors, gauze, KimWipes, PBS in squeeze bottle, 70% ethanol in spray bottle, and red biohazard bag.

2. Lumbar Vertebra Dissection

2.1. Position the rat in a supine position (abdomen up).

2.2. Spray the rat with 70% ethanol, thoroughly dousing the abdomen.

2.3. Make a small incision at the midline in the lower abdomen, just above the hip.

2.4. Extend the incision up to the rib cage.

2.5. Pull back the skin and expose the abdomen.

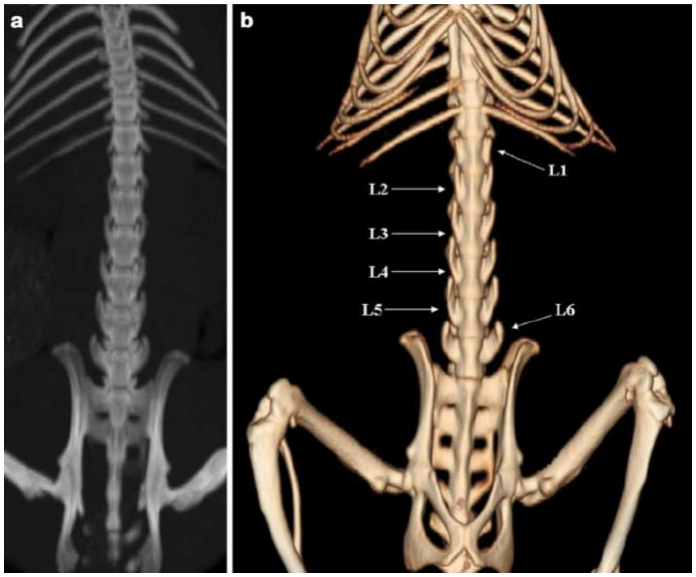
2.6. Move aside the internal organs within the abdominal cavity to expose the vertebral column.

2.7. Expose vertebral column from the rib cage to the pelvis. Caution: Be certain not to damage the vertebrae with cuts or scrapes during this process.

2.8. Using a scalpel, cut through the intervertebral disc of the T12 vertebra (the last rib will be connected to the **top** of the T12).

2.9. Cut through the intervertebral disc above the first fused vertebra (below the final lumbar vertebra - L5 or L6, see Figure below).

2.10. Using the scalpel, cut the muscles surrounding the spine and separate from the skin of the back. *Caution: Be certain not to damage the bones with cuts or scrapes during this process.*



2.11. Cut any remaining connective tissue attaching the spine to the soft tissue.

2.12. Remove any additional muscle or connective tissue attached to the vertebrae.

2.13. Separate the vertebrae by cutting through the adjacent intervertebral discs. Caution: Be certain not to damage the vertebrae with cuts or scrapes during this process.
2.14. Use forceps and Kim wipes to remove as much soft tissue as possible.
2.15. Wrap each individual bone in PBS-soaked gauze and store in individual (labeled) bags at -20°C.

3. Femur Dissection
3.1. Position the rat in a supine position (abdomen up).
3.2. Spray the rat with 70% ethanol, thoroughly dousing the abdomen.
3.3. Make a small incision to the right of midline in the lower abdomen, just above the hip.
3.4. Extend the incision down the leg and past the ankle joint.
3.5. Pull back the skin and cut the quadriceps muscle anchored to proximal end of the femur to expose the anterior side of the femur.
3.6. With the blade of the scissors against the posterior side of the femur, cut the hamstrings away from the knee joint. *Caution: Be certain not to damage the femur with cuts or scrapes during this process.*
3.7. Pull back the skin and the hamstring muscles anchored to proximal end of the femur to expose the posterior side of the femur.
3.8. With the forceps, hold the distal end of the femur, just above the knee joint. Guide the blades of the scissors on either side of the femoral shaft towards the hip joint, being VERY careful not to cut into the femur itself.
3.9. After reaching the femoral head, indicated by the scissors opening slightly, twist the scissors with the top blade of the scissors moving directly over the femoral head to dislocate the femur, being careful not to snap the bone below the femoral head.
3.10. Grasp the top of the femoral shaft with the forceps, cut the soft tissue away from the femoral head to release it from the acetabulum.
3.11. Pull the entire leg bone, including femur, knee, and tibia, up and away from the body, carefully cutting away the connective tissue and muscle connecting the leg to the skin.
3.12. Overextend the knee joint and again use the scissors in a twisting motion to dislocate the tibia.
3.13. Cut any remaining connective tissue attaching the long bone to the mouse at the knee.
3.14. Remove any additional muscle or connective tissue attached to the femur.
3.15. Use forceps and Kim wipes to remove as much soft tissue as possible.
3.16. Wrap each individual bone in PBS-soaked gauze and store in individual (labeled) bags at -20°C.

6.2.3 Specimen Preparation of Whole Rat Vertebrae for Biomechanical Testing

University of California, Berkeley
Berkeley Biomechanics Lab
Standard Operating Procedure

Specimen Preparation of Whole Rat Vertebrae for Biomechanical Testing

SOP, Version 2
Date: 03/04/2020

Author(s): Shannon Emerzian
Principal Investigator: Tony M. Keaveny

Summary: This protocol summarizes the method of embedding the rat vertebral body and removing the endplates to obtain a specimen with planoparallel ends perpendicular to the long axis of the vertebral (VB) body.
Key Words: rat vertebral bodies, PMMA, Isomet
Materials:

- Rat vertebrae
- KimWipes
- Gauze
- Absorbent pads
- Ziplock bags (storage)
- Sharpie
- 1X PBS
- Bone clippers (flat edge)
- Tweezers (1 fine point, 1 with teeth)
- PMMA (Bosworth Fastray, COE Tray Plastic or equivalent, liquid and powder)
- Small glass graduated cylinder (10 mL)
- Vice
- Per 1 vertebral specimen...
    - Mixing cup (polypropylene mini shot glasses work well) and popsicle stick
    - Monojet Curved Tipped Syringe (or equivalent)
    - 3D printed vertebral mold

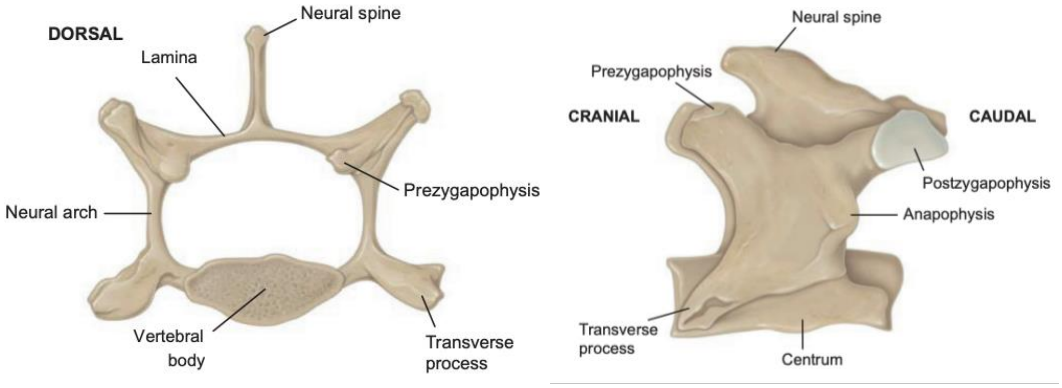
Equipment:

- Digital calipers
- IsoMet 1000 Precision Saw
    - 4” Isomet blade (IsoMet Diamond Blade, 15LC, 4” diameter)
    - IsoMet Jigs
        - IsoMet Rat VB Sample Chuck
        - IsoMet Dressing Stick Chuck

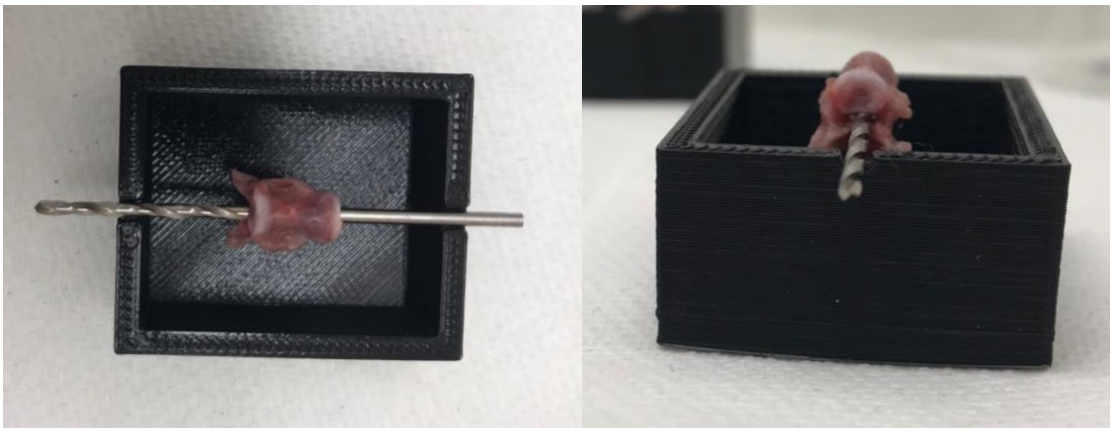
- Dremel with Dremel 409 Cut-off wheels

Procedure:

1. Preparation (~2 hours)
    1.1. Verify that there are enough 3D-printed molds for the number of specimens to be prepared. Each VB will require one mold. If there are too few, more may be 3D-printed using ABS or PLA plastic.
    1.2. If frozen (-20°C), thaw before embedding (*Note: this will take ~ 2 hours*)
        1.2.1. Thaw in the refrigerator (4°C) at least 1 hour. Keep VB in their storage plastic bag during thaw.
        1.2.2. After at least 1 hour, submerge VB (inside of its storage bag, and inside of a secondary bag) into a tub of cool water for 15 minutes.
        1.2.3. Rest on the counter to allow rat to come to room temperature while you set up (~10 minutes)
        1.2.4. Note: Specimens may only be embedded in PMMA if they are *fully* defrosted.
    1.3. Place absorbent underpad on work area (white side up)
    1.4. Clear a work area underneath the fume hood
2. Embedding (~ 45 minutes)
    2.1. Place absorbent underpad on work area (white side up)
    2.2. Remove sample bags from water and unwrap the sample on the work area.
    2.3. Clean off any excess soft tissue with the tweezers and Kim wipes, as necessary.
    2.4. Use bone clippers to remove the two transverse spinous processes from the VB. Leave the dorsal process (neural spine in the image below) for embedding.



    2.5. Test all VB being potted for fit in drill bit library. Fit should be snug but not forced. Once drill bits are inserted, maintain hydration with 1x PBS. Record the VB specimen number and level, as well as the drill bit size.
    2.6. Label molds with the specimen number and VB level on one side, drill bit size on the other. Gently place VB on mold with processes facing down, as illustrated below.



2.7. Align the VB such that the remaining spinous process on the sample are below the top of the mold. The VB body should be above the drill bit entirely. Observe it from the top and side. Sift as necessary to ensure the major axis of the VB is aligned with the drill bit and the VB body is centered on the drill bit.

2.8. Clear a work area underneath the fume hood; place an absorbent pad here as well.



2.8.1. Measure out 10mL of PMMA powder into a plastic test tube. Measure 5.1mL of PMMA liquid into a glass graduated cylinder.

2.8.2. **Mix slowly** in a plastic cup (note: polystyrene cups will disintegrate upon contact with the PMMA! Use polypropylene.) with a popsicle stick**.** After mixing for ~10 sec, the mixture should be a uniform liquid.

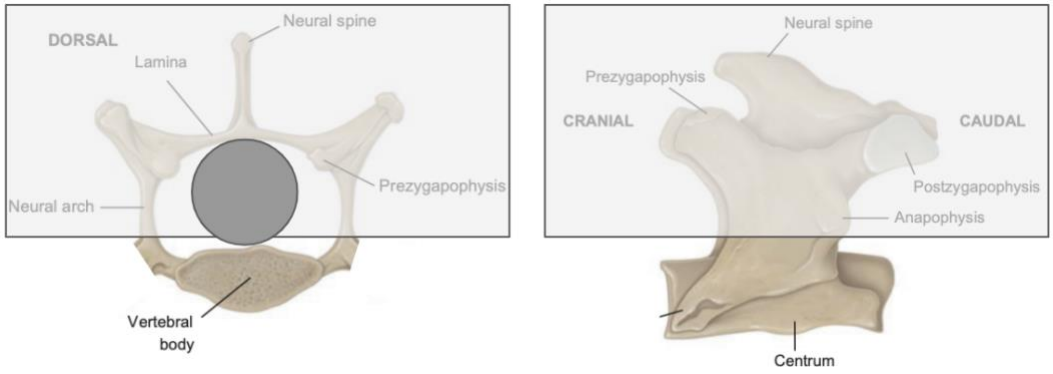
2.8.3. Use a curved tipped syringe to suck up approximately half of the PMMA.

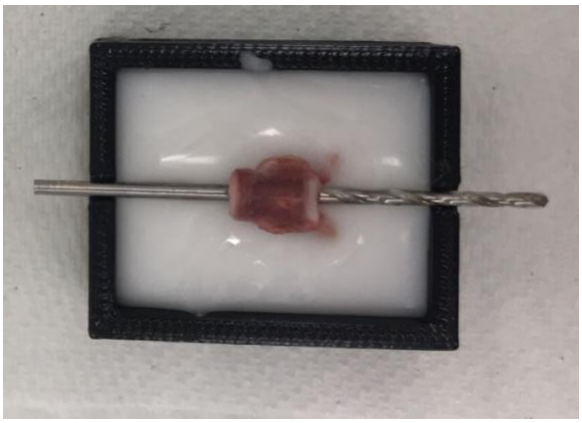
2.8.4. Carefully pour the remainder of the PMMA into the mold.

2.8.5. Using the curved tipped syringe, fill the mold with PMMA until the posterior elements of the VB are mostly submerged in the mixture. The body of the VB should not contact the cement. Watch closely from the side. See images below.

Note: **Pour continuously!** Stopping and starting again may create air bubbles in the mixture as the PMMA cures.

Note: Ensure that the VB remains level and in line with the drill bit.





2.9. Once the PMMA has begun to set (slightly, ~7 minutes), maintain hydration by covering the bone with 1x PBS.

2.10. The PMMA mixture will begin to harden after approximately 15 minutes. Test this by gently poking the PMMA in the corner, far from the VB.

Note: Embed other tissue while you wait but keep an eye on the current sample.

2.11. When the PMMA has fully set, remove the drill bit with extreme care. Pull it straight out, do not lift it up or down, this could unseat or crack the bone.

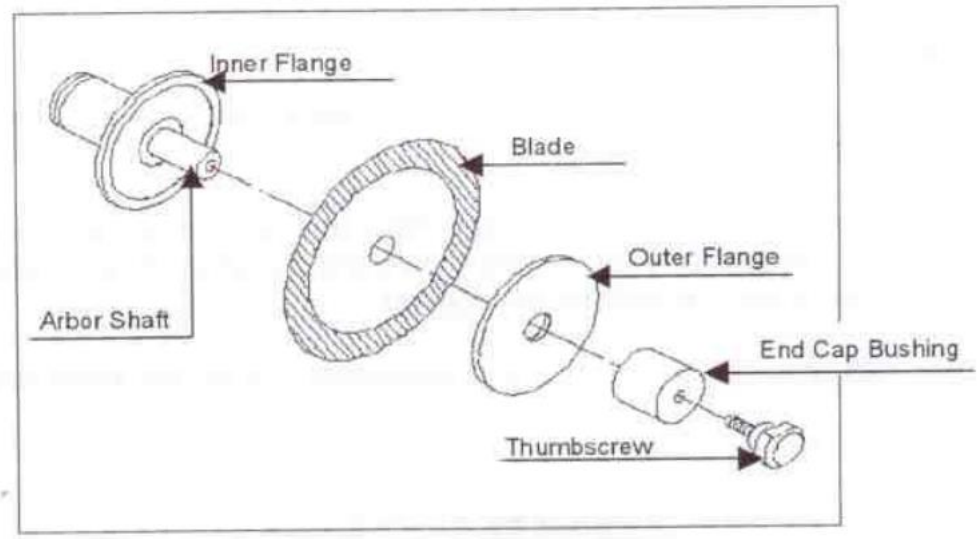
2.12. Maintain hydration with a piece of gauze and 1X PBS.

2.13. Immediately move on to cutting.

3. Cutting ~ 5 minutes

3.1. IsoMet Blade installation

Note: Use a 4” blade for rat VB. See Equipment List above for details.

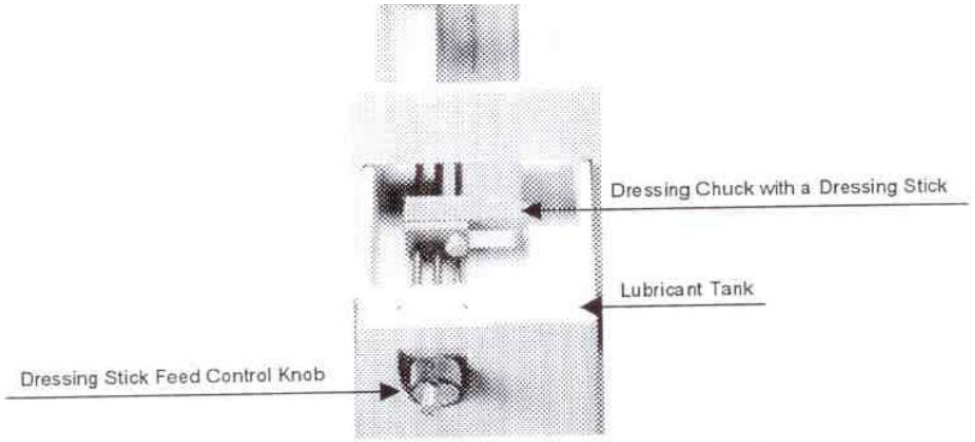


3.1.1. Remove the thumbscrew, end cap bushing, and outer flange from the arbor shaft.
3.1.2. Install the 4” blade on the arbor shaft against the inner flange (3” flanges).
3.1.3. Slide the outer flange, the end cap bushing, and the thumbscrew on to the arbor shaft.
3.1.4. Hand tighten the thumbscrew to secure the blade.

3.2. Fill the lubricant tray with distilled water to a level that will immerse the blade by approximately ¼ inch.

3.3. Blade dressing (as needed)

Note: Blade dressing removes built up matrix metal and exposes the abrasive grain to provide clean, aggressive cutting. New wafering blades should be dressed several times and older blades should be dressed as required.



3.3.1. Secure the dressing stick in the dressing chuck.

3.3.1.1. From the front of the machine, pull the lubricant tank straight out until the blade contacts the back of the tank. Slide the IsoMet Dressing Stick Chuck onto the tracks in the lubricant tank. Secure with a set screw.

3.3.1.2. Position the dressing stick as needed in the chuck.

3.3.1.3. Secure the dressing stick with a set screw.

3.3.1.4. Close the lubricant tank until the chuck is just out of reach of the blade.

3.3.2. Close the hood.

3.3.3. Set speed to 175 RPM.

3.3.4. Press the SAW button to activate the saw.

3.3.5. Slide the lubricant tank slowly in to feed the dressing stick into the wafering blade.

3.3.6. Make as many cuts through the dressing stick as needed to dress the blade (175 RPM). Three to five cuts usually works well.

3.4. Parallel Cut VB

3.4.1. Mount the VB Sample Chuck onto the Sample Arm of the saw

Note: The VB Sample Chuck will probably already be on the Sample Arm.

3.4.1.1. If a new fixture needs to be manufactured, drawing files for the fixture may be found in the Google Drive under “IsoMet Rat VB Sample Chuck”. It should be machined from aluminum and fit with four set screws (1 x 4-20 and 3x10-32).

3.4.2. Use a scalpel to remove disc material from each VB body.

3.4.3. Take three measurements of VB body height at 90° intervals. Calculate average height, **H**. Record these values in the specimen data collection sheet.

3.4.4. Calculate the location of the two cuts:

3.4.4.1. Cut 1: **H**/4

3.4.4.2. Cut 2: 3**H**/4 + BW (where BW = blade width = 0.26 mm ≃ 0.3 mm)

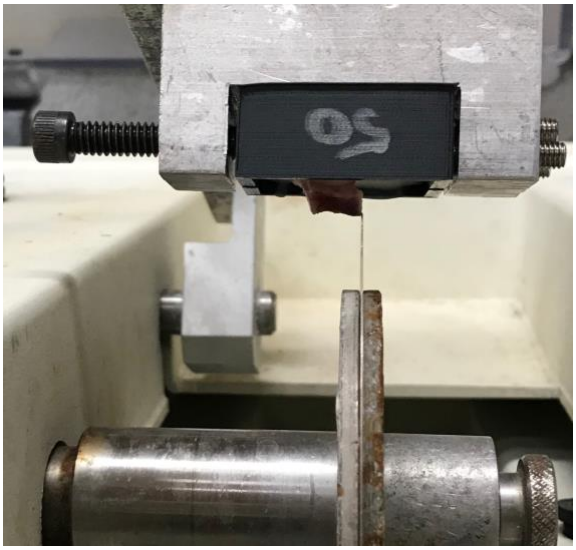
3.4.4.3. Record the cut locations in the specimen data collection sheet.

3.4.5. Place the embedded specimen in the IsoMet Rat VB Sample Chuck with the caudal side towards the IsoMet arm. (This results in the cranial end, which is usually more parallel to the blade, closest to the blade).



3.4.6. Adjust the four set screws to align the VB horizontally. The major axis of the VB must be perpendicular to the IsoMet blade. Note: Take care while doing this - if the cuts are not parallel and perpendicular to the major axis, the sample will not undergo uniaxial compression, distorting experimental results.

3.4.7. Use the sample positioning knob to move the Sample Arm such that the blade is against the cranial side of the VB (right side). Zero the position.



3.4.8. Adjust speed to 250 RPM.

3.4.9. **Cut 1:** Raise IsoMet Sample Arm and move the arm to the right to the calculated position for Cut 1 (H/4 mm). Turn the blade on and make one cut all the way through the VB.

3.4.10. **Cut 2:** Turn off the blade, raise IsoMet Sample Arm and move the sample to the calculated position for Cut 2 (3H/4 + BW). Make a second cut at 250 RPM.

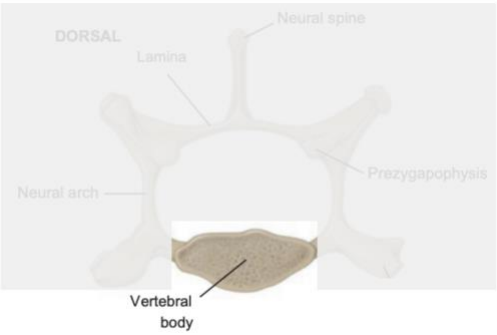
3.4.11. Remove the specimen from the IsoMet.

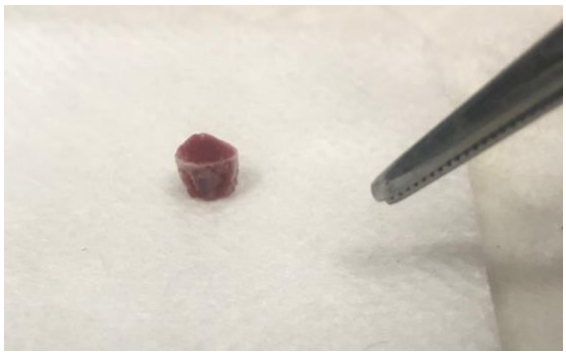
3.5. Remove specimen from mold

3.6. Secure specimen in a vice.

3.7. Using a Dremel with a 409 cut-off wheel, carefully remove the VB from the sample mold. Be certain not to damage the VB body during this process.

3.8. Using bone clippers, remove any remaining pieces of the spinous processes. Use Kim wipes to remove any soft tissue. At this point, you want to have the VB body isolated.





3.9. Any remaining spinous processes or soft tissue should be removed.

3.10. Measure the height 4 times with calipers at 90° intervals. Calculate the mean height (H). Record all measurements in the specimen data collection sheet.

3.11. Calculate maximum percentage variation in specimen height to determine planoparallelism. Value should be less than 1.5% of mean height H in order to be "Accepted". Note Accept/Reject in the sample data collection sheet.

3.12. Repeat steps 3.4 and 3.5 for all other VBs.

3.13. Rewrap and moisten the sample with 1X PBS solution, storing it in the bag and replacing the bag in the -20°C freezer.

6.2.4 Method for Scanning Rat Vertebrae on BIDMC ChaCha microCT Scanner

University of California, Berkeley
Berkeley Biomechanics Lab
Standard Operating Procedure

Method for Scanning Rat Vertebrae on BIDMC ChaCha microCT Scanner

SOP, Version 1
Date: 05/12/2020

Author(s): Shannon R. Emerzian
Principal Investigator: Tony M. Keaveny (BIDMC: Mary Bouxsein)

Summary: This protocol guides you through the image processing steps needed collect microCT scans at the Center for Advanced Orthopaedic Studies at BIDMC (PI: Mary Bouxsein) with a voxel size of 15µm^3 (isotropic). This procedure was adapted from the "Method for four femur scanning on BIDMC ChaCha microCT Scanner" by Daniel Brooks (Shannon Emerzian's Lab Notebook #2, p 159).
Key Words: microCT, Scanco, vertebrae
Materials:

- Prepared vertebral bodies
- Software: µCT 80 (Scanco Medical)
- Hardware: Scanco µCT 40
- Data collection sheets (for tracking progress)

Equipment:

- External Hard Drive

Note: this protocol was written for scans collected in the following manner:

- Scanning medium: 1X PBS
- Loading notes: Thaw for 30 minutes, orient cranial end on top, load 4 specimens at random; After scanning, wrap in PBS-moistened gauze and store at -20C
- Instrument: Scanco Medical uCT40 specimen scanner
- Voxel size: 15µm^3 (isotropic)
- X-ray settings: 70kVp potential, 114µA intensity
- Integration time: 300ms
- Global threshold: 500 mgHA/cm^3

Steps:

1. Create samples in the sample database

a. Create your sample in the database. Click on “Gear” button (farthest to the left) to open the sample creation window. Enter in a sample name, click “Save” and then record the sample number in your data collection sheet. Click “New” to repeat the process for all samples. Be sure to include the study name and the scan number in the sample name (UCB2020-1_scan1).
b. Load samples into the four-femur fixture
    i. Use forceps to place rubber stoppers in each hole of the fixture. Align the stoppers so the tops are at the same height. Partially fill each tube of the fixture with PBS.
    ii. Use forceps to place one vertebra in each of the tubes of the fixture. Position the bones such that the posterior side of the bone faces the number on the tube.
    iii. Record the position of each vertebra in your scan setup sheet.
    iv. Insert a rubber stopper on top of each vertebra to prevent PBS from evaporating during scan.
    v. Place the fixture into the 20mm diameter sample tube. Position the fixture such that the marking on the top is in line with the sample tube seam.
    vi. Place the fixture in the scanner such that the seam is facing you.
    vii. Close the scanner door.
c. Scan setup
    i. Open the Sample Measurement program by clicking on the second button from the left.
    ii. Enter the sample number of the scan you are performing.
    iii. Select control file (#95)
    iv. Click “Scout-View”
    v. In the scout-view window, ensure that the startposition, endposition, and angle are reasonable Then click “Scout-View” in the scout-view window. It might take a few seconds for the scout-view to be performed.
    vi. Select “Reference Line”. Move your cursor such that the reference line is at the bottom of the vertebra in tube #1.
    vii. Adjust the number of slices in the scan by holding down the shift key and then moving the mouse up/down to reach the correct number of slices. Once you have the correct number, place the top of the reference line at the top of the vertebra, and then click the left mouse button. The reference line will now be fixed in position.
    viii. Once the reference line has been added, click “Add Task” A window will pop up telling you a task has been added.
    ix. Start the batch scan by clicking the “Submit Task List” button. After you click the button, the Sample Measurement Program window will remain open for 5 seconds and then close. It may take a minute of the scanner to start up.
    x. Scans will take approximately 1 hour.

6.2.5 Image Processing of Rat Vertebral microCT Scans

University of California, Berkeley
Berkeley Biomechanics Lab
Standard Operating Procedure

Image Processing of Rat Vertebral MicroCT Scans

SOP, Version 1
Date: 05/12/2020

Author(s): Shannon R. Emerzian
Principal Investigator: Tony M. Keaveny

Summary: This protocol guides you through the image processing steps needed to go from the original micro-CT scans to the final stack needed later for the FEA model. This protocol does not include steps for the mesh and FEM. The original microCT scans were conducted at the Center for Advanced Orthopaedic Studies at BIDMC (PI: Mary Bouxsein) with a voxel size of 15µm^3 (isotropic).
Key Words: ImageJ, micro-CT, thresholding, reorientation
Materials:

- Original DICOM stack of images from micro-CT
- Software: ImageJ or Fiji with plugin 3D Viewer
- Software: DataViewer (Windows only; Bruker microCT Software Downloads)
- Data collection sheets (for tracking progress)

Equipment:

- External Hard Drive

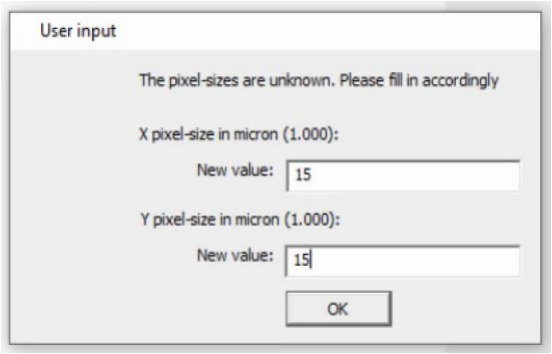
Note: this protocol was written for scans collected in the following manner:

- Scanning medium: 1X PBS
- Loading notes: Thaw for 30 minutes, orient cranial end on top, load 4 specimens at random; After scanning, wrap in PBS-moistened gauze and store at -20C
- Instrument: Scanco Medical uCT40 specimen scanner
- Voxel size: 15µm^3 (isotropic)
- X-ray settings: 70kVp potential, 114µA intensity
- Integration time: 300ms
- Global threshold: 500 mgHA/cm^3

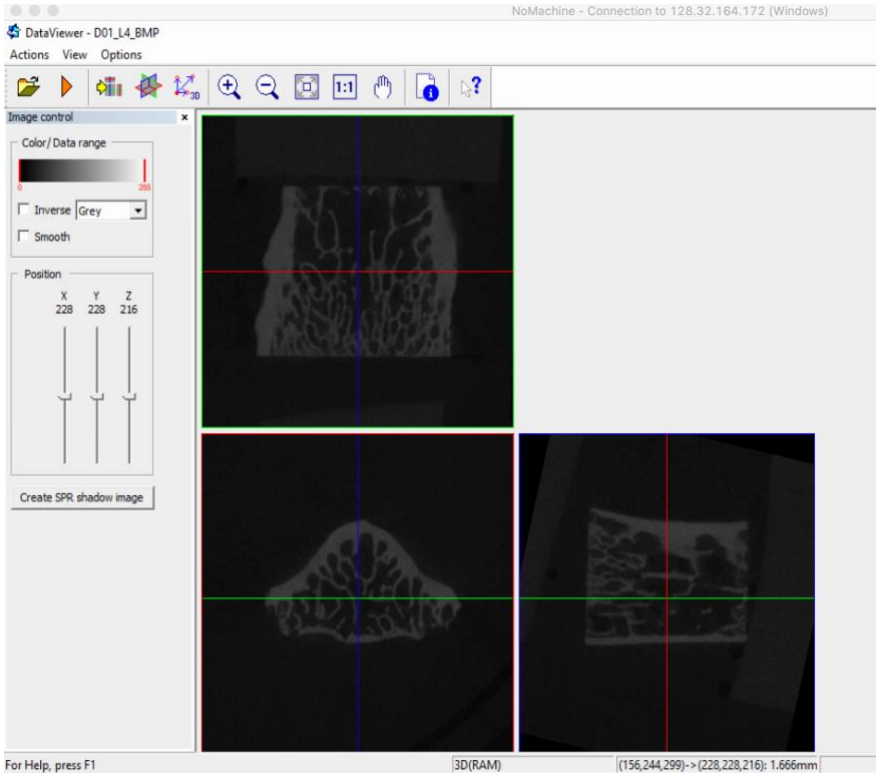
Steps:

2. Create the following folders for your sample DXX_LY (where XX is the specimen number 01-27 and Y is the vertebral level, either L4 or L5).
    a. Create one folder for your sample DXX_LY (e.g., D01_L4)
        i. Rename original scan folder: DXX_LY_DICOM
        ii. DXX_LY_BMP
        iii. DXX_LY_Reorient
        iv. DXX_LY_ReorientTruncate
        v. DXX_LY_TIF
3. Fiji/ImageJ Part I - this begins from the original DICOM stacks made from microCT
    a. File->Import ->Image Sequence. Click on the first DICOM file of the series of DICOM files. Press OK. Image sequence will open in Fiji.
    b. File -> Save As -> Image Sequence. Save as BMP format in the BMP folder (DXX_LY_BMP) and press OK.

4. DataViewer - Reorient and Truncate
    a. Open DataViewer and import the file with the BMP images (Actions>Open>Open Dataset, double click on the first image).
    b. Click "Load for 3D Viewing" icon (third button from left)
    c. Input the pixel size from the scan. In this case, 15 µm/vox, for both x and y.



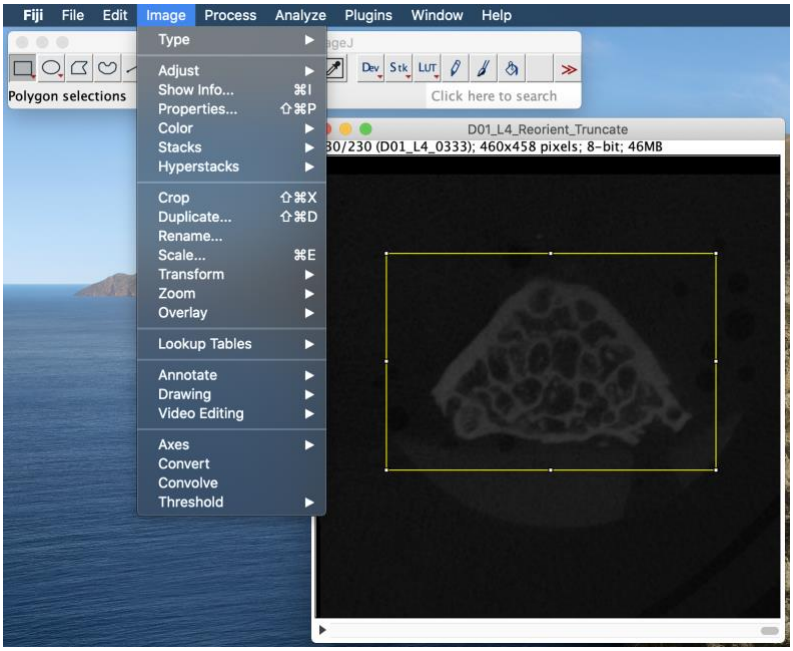
    d. Reorient the image stack.
        i. General instructions for DataViewer:
            1. Three cross-sectional images:
                a. Bottom left: Transverse X-Y view (orientation of original scans)
                b. Bottom right: Sagittal Z-Y view
                c. Top left: Coronal X-Z view
            2. To change the plane of view, use the cursor to drag the axes bars on the images. Dragging the blue bar moves you along the X-axis, green along the Y-axis, and red along the Z axis.
            3. To reorient your image, hold down CTRL and drag the cursor.



ii. Begin aligned with views down the middle of the bone cross section.
iii. Rotate the transverse X-Y view (bottom left) such that that the bone is oriented such that the triangle is pointed to the top of the image.
iv. Reorient the coronal X-Z view such that the top and bottom of the VB (this is where the parallel cuts were made) are as close to horizontal as possible.
v. Reorient the sagittal Z-Y view (right bottom image) such that the left and right sides (in reality, this is the top and bottom of the VB - again, your cut surfaces) are as vertical as possible.

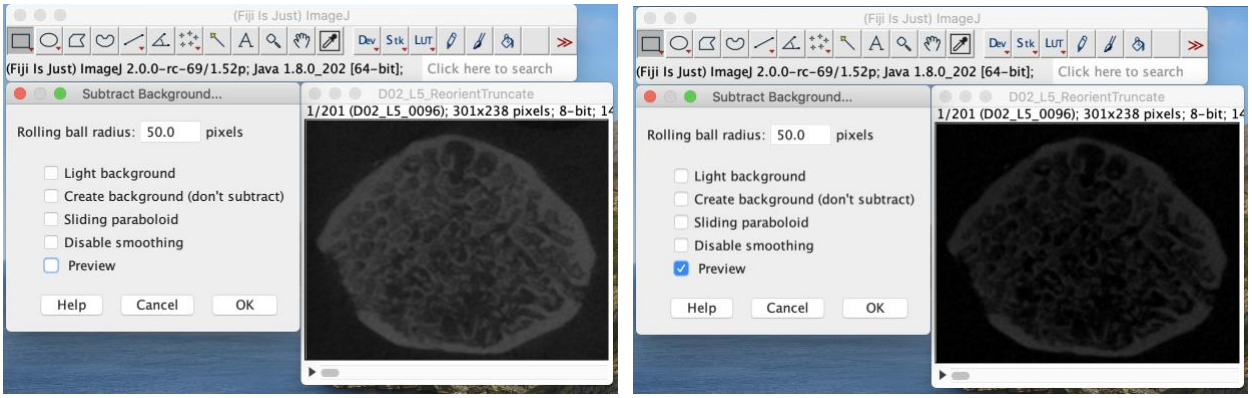
e. Once finished, save the images as a dataset: Actions→ Save→ Transaxial (X-Y) Image as a dataset (DXX_LY_xxxx). Save as BMP in the "Reorient" folder (DXX_LY_Reorient).
f. While still open in DataViewer, mark down which slices to remove on either end of the imageset. Click the Z-axis to adjust one slice at a time. Anything with "grey" you will remove! Mark down which slices to remove on either end in the spreadsheet.
g. Go into the "Reorient" folder. Copy and paste the imageset into the "Reorient_Truncate" folder.
h. Delete the slices to remove on either end of the imageset. This is now the truncated dataset.

5. Fiji/ImageJ Part II - Threshold
   a. File > Import > Image Sequence (Open "reorient truncate" folder)
   b. Crop image



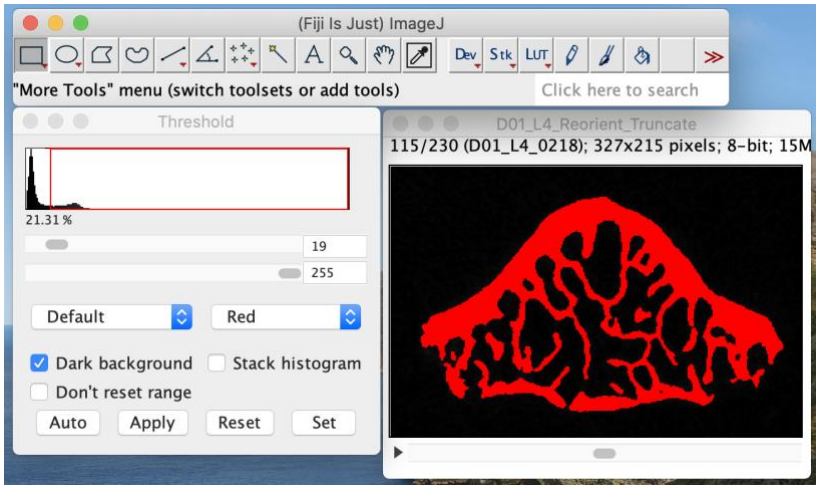
i. Use the rectangle tool to draw a rectangle around the bone. Be certain to scroll through every slice in order to select the entire bone in all slices.
ii. Image > Crop

c. Remove background (makes thresholding easier if there are high contrast areas)

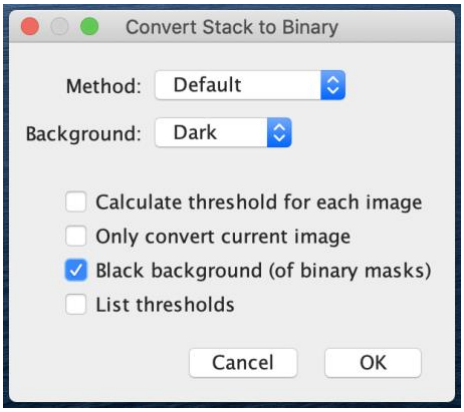


i. Process > Subtract Background
ii. Rolling ball radius: 50 pixels
iii. Select and deselect “Preview” to verify that this radius is not removing too many bone pixels.
iv. Click ‘OK’
v. Process all XXX images? There is no Undo if you select ‘“Yes”. → Click ‘Yes’.

d. Threshold



i. Scroll to a slice in the middle of the stack.
ii. Image>Adjust>Threshold
iii. Make sure "dark background" is checked. Use "Default" threshold mode.
iv. Jump to beginning/end slices to verify the threshold values are reasonable.
v. Record threshold values in the datasheet.
vi. Click Apply.



vii. New window will pop up called "Convert Stack to Binary" (see above)
    1. Method: Default
    2. Background: Dark
    3. Ensure everything is unchecked **except** "Black background (of binary masks)"
    4. Click OK

e. This step is VERY important! Open in 3D viewer (Plugins > 3D Viewer). Note anything unusual in the datasheet. If there appears to be an error in image processing (slices missing, etc.), backtrack!
f. Calculate the specimen height: write down total number of slices, multiply by voxel size (15um).
g. File > Save As > Image Sequence > TIFF > OK (save in folder DXX_LY_TIFF) IMPORTANT: Be sure to save files as DXX_LY_ and allow the auto index to

immediately follow (e.g., D01_L4_0000, D01_L4_0001, etc.) or you will have to edit a file in the FEA steps for each sample.

h. Note: This final TIFF stack will be used to continue with the mesh and model steps needed for FEA.

6. Transfer TIF directory to Biomech5 using a Terminal session on local machine
    a. Navigate to directory with files to transfer
    b. First, tar sample directory with TIF files
        i. tar cf sample-directory_TIF.tar sample-directory_TIF
    c. Transfer to biomech5 using scp
        i. scp sample-directory_TIF.tar shannon@128.32.164.178:/home/shannon/Dissertation

6.2.6 Build Connected Volume for Rat Vertebral Body Finite Element Analysis

University of California, Berkeley
Berkeley Biomechanics Lab
Standard Operating Procedure

Build Connected Volume for Rat Vertebral Body Finite Element Analysis

SOP, Version 1.1
Date: November 2020, minor updates April 2021

Author(s): Shannon Emerzian
Principal Investigator: Tony M. Keaveny

Summary: This protocol outlines the steps to create connected volumes from microCT scans.
Key Words: finite element analysis, rat vertebral bodies
Materials:

- Image Processed microCT scans in TIF format (whole bone, isolated cortical compartment, isolated trabecular compartment)

Equipment:

- Access to Biomech5
- Scripts
    - tiff2vol.pro
    - loadmodel.pro
    - volcheck.pro

Procedure:

1. Transfer image stacks to Biomech5

    For this process, you MUST have an image stacks for at least one of these:
    - the whole VB (SOP 3),
    - the isolated cortical shell (SOP 3b)
    - the isolated trabecular compartment (SOP 3c)

Note: This step is written for transferring just 1 file at a time - feel free to bulk transfer files to make your life easier.

    a. Navigate to your (local) directory with image stacks to transfer
    b. First, compress sample directory with the TIF files using tar
        i. CORTICAL: tar cf ID_Cortical.tar ID_Cortical
        ii. TRABEC: tar cf ID_Trabec.tar ID_Trabec
        iii. WHOLE: tar cf ID_Whole.tar ID_Whole

c. Transfer to biomech5 using scp
   i. CORTICAL:
   scp ID_Cortical.tar shannon@128.32.164.178:/home/shannon/Dissertation/JMYA
   ii. TRABEC:
   scp ID_Trabec.tar shannon@128.32.164.178:/home/shannon/Dissertation/JMYA
   iii. WHOLE:
   scp ID_Whole.tar shannon@128.32.164.178:/home/shannon/Dissertation/JMYA

2. Log in to Biomech5

----Physical login:
ALT+CTRL+Backspace
Log in to the computer with
Username: shannon
Password: berkeley
----Remote access:
Open NoMachine to remote access Biomech5
Log in to the computer with
Username: shannon
Password: berkeley

3. For all samples

**Note: you will do this step 3x, once for each compartment/model (i.e., once for cortical compartment, once for trabecular compartment, once for the whole bone)

On Biomech5, open up a Terminal by right clicking on the desktop. Navigate to the directory with all of the TIF files. (/home/shannon/Dissertation/JMYA)

You are going to start with this directory structure for EACH sample

- SampleID
  - SampleID_Whole
    - All TIF files for the whole bone
    - tiff2vol.pro
  - SampleID_Cortical
    - All TIF files for the cortical shell
    - tiff2vol.pro
  - SampleID_Trabec
    - All TIF files for the trabecular compartment
    - tiff2vol.pro

Example of this directory structure for sample D01_L4. Note we are already in /home/shannon/Dissertation/JMYA

- D01_L4
  - D01_L4_Whole
    - All TIF files for the whole bone
    - tiff2vol.pro
  - D01_L4_Cortical

        - All TIF files for the cortical shell
        - tiff2vol.pro
    - D01_L4_Trabec
        - All TIF files for the trabecular compartment
        - tiff2vol.pro

In order to get to the structure described above, we first need to create the top-level directory (e.g., SampleID) for both the cortical and whole bone.

mkdir SampleID Hit 'enter'

Now, move your .tar files (Whole, Cortical, Trabecular) into this new directory.

mv *.tar SampleID Hit 'enter'

Move into that sample directory

cd SampleID Hit 'enter'

Extract files from tar

tar xf SampleID_Whole/Cortical/Trabec.tar Hit 'enter'

a. Create volume using tiff2vol.pro in IDL

Find the IDL script called 'tiff2vol.pro' (Note: IDL scripts end with .pro). If not already in the same directory as the TIF files, you need to copy the tiff2vol script to that directory. Do this by typing in commands to the terminal like the following:

Go to the directory where you want your tiff2vol.pro to be on and get the path for this directory.

pwd Hit 'enter'

Copy and paste the path by right clicking. (Note: keyboard CTRL+C and CTRL+V will not work!)

Open a new Terminal window by right clicking on the desktop. Navigate to the directory where the tiff2vol.pro currently exists. (Note: to paste the directory path, right click).

scp tiff2vol.pro ../directory_path_copied_and_pasted_here Hit 'enter'

Once tiff2vol is already in your working directory, update it for your sample:

nano tiff2vol.pro Hit 'enter' ← opens tiff2vol.pro in nano

The data to be adjusted <u>each time you run this job</u> are in **red** below.

tiff2vol.pro

```
PRO tiff2vol,id,xx,yy,start,finish
;Tongge WU
;Dec 10 2018
;Updated by SRE 2020
;Project Emerzian Rat Irradiation

;IDL script runs at local workstation

;construct volume for original microCT scan
;id is the sample id (e.g., 'D01_L5')
;xx, yy are the tiff X and Y dimension
;start is (usually) 0, finish is the max id of the microCT scan tiff files
;output: a volume file

;input parameters
zsize=finish-start+1
vol=intarr(xx,yy,zsize); size for this model is xx by yy
slcr=intarr(xx,yy)
startz=start
endz=finish
sizez=endz-startz+1
for i=start, finish DO begin
  ;pile up images
  ;loading the tiff files corresponding to z-slices
  fn='D01_L4_'+ strcompress(string(format='(I4.4)',i)) + '.tif'
  slc=read_tiff(fn)
  slcr(*,*)=slc(*,*)
  vol(*,*,endz-i)=slcr(*,*)
  ;assigning the slice pixel values to the z-slices in the newly defined volume,vol
endfor
print, 'Finished loading .tif files'

;convert to bindat
;original data is uint16 tif, now is binary8
vol = (vol eq 255)*255b + (vol eq 0)*0b

; Writing to file
ofn=id+'.'+strcompress(string(xx),/remove_all)+'.'+strcompress(string(yy),/remove_all)+'.'+strcompress(string(siz
ez),/remove_all)+'.'+strcompress(string(startz),/remove_all)+'_'+strcompress(string(endz),/remove_all)+'.vol'
print,'writing to file',ofn
scanvol,vol
```

Hit 'control+x' ← exit nano

Save modified buffer? y Hit 'Enter' ← save changes

File Name to Write: tiff2vol.pro Hit 'Enter' ← exit nano

---------- START IDL ----------

Now enter into the IDL (Interactive Data Language) language.
Note: IDL gives you more tools to work with when building a volume, you will only need to learn a handful of these tools. **Note that indexing in IDL starts with 0**. You can leave IDL by typing exit and hitting enter.

idl Hit 'Enter" ← enter IDL

We first need to know the size of this TIF stack of images before turning it into a volume. Once in IDL, get the dimensions from only one of the TIFs so that you know the dimensions when building the volume. (You can highlight a filename and press the scroll wheel to copy and paste which makes command entering faster.)

Use the following commands:

a =read_tiff('Sample_name.tif') Hit 'Enter'
print, size(a) Hit 'Enter'

print returns an array that is organized like the following:

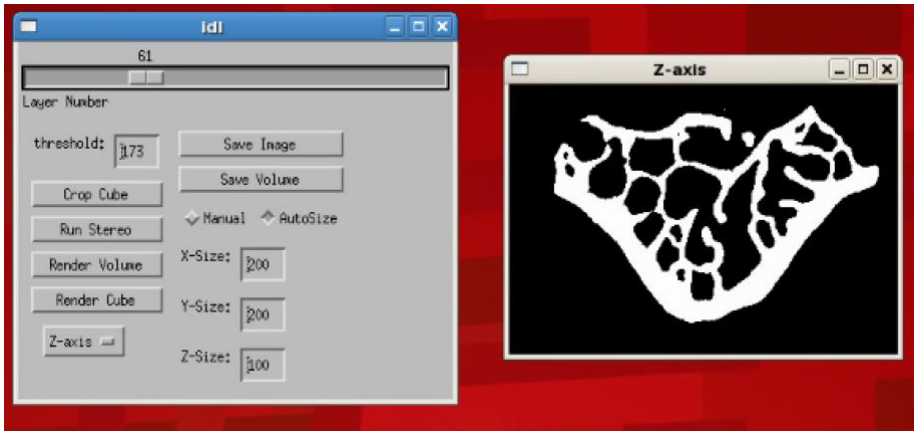
sizeX size Y #

Record sizeX and sizeY in the "Data Collection Sheet". These values are the number of pixels (slices) of the image in the X and Y direction. Also, make note of the number of slices (e.g., they are numbered from 0000 to 0229, then z-dim start is 0 and z-dim end is 229).
Now you can stack these images together to build a volume! Still in IDL, type the following to run the script (recall: id is sample ID, e.g., D01_L5; xx and yy are the tiff X and Y dimensions; start is z-dim start; finish is z-dim end).

tiff2vol,'id',xx,yy,start,finish Hit 'enter' ← see example** below

**Example: for D01_L4, x = 327, y = 215, z= 230, z-dim start = 0, z-dim end = 229
Whole bone → tiff2vol,'D01_L4',327,215,0,229
Cortical bone → tiff2vol,'D01_L4_Cortical',327,215,0,229
Trabecular bone → tiff2vol,'D01_L4_Trabec',327,215,0,229

You will see the volume pop-up on the screen. Scroll through the images to make sure they loaded correctly.



Type exit to exit IDL.

---------- END IDL ----------

Use ls to verify that a new file is present → nameOfVol.vol

Create .vol files for ALL samples you are working with (i.e., Whole, Trabec, Cortical) before continuing to the next step.

At this stage, if you have created individual volumes for: cortical compartment, trabecular compartment, and the whole bone. You should have the following directory structure:

- SampleID (e.g., D01_L4)
  - SampleID_Whole (e.g., D01_L4_Whole)
    - All TIF files for the whole bone
    - tiff2vol.pro
    - SampleID.xx.yy.zz.zstart_zend.vol
  - SampleID_Cortical (e.g., D01_L4_Cortical)
    - All TIF files for the cortical shell
    - tiff2vol.pro
    - SampleID_Cortical.xx.yy.zz.vol
  - SampleID_Trabec (e.g., D01_L4_Trabec)
    - All TIF files for the trabecular compartment
    - tiff2vol.pro
    - SampleID_Trabec.xx.yy.zz.vol

Once all .vol files are created (Cortical.vol, Trabec.vol, Whole.vol), proceed to one of the following steps:

→ For a single material sample, EITHER

1. Isolated cortical compartment
2. Isolated trabecular compartment
3. Whole bone - no separation of cortical/trabecular compartments

Go to #4 below.

→ For a two material whole bone sample (with separate cortical and trabecular compartments), go to #5 below.

4. For a single material sample
    a. Use connect to remove noise

Now you need to remove small isolated solid clusters (noise) that are not connected to the large solid cluster which is the entire vertebra. Use the following command to remove pieces of the model disconnected from the bone. Be sure to add .connect at the end, otherwise you will overwrite your original volume. Fill in the dimensions that match your sample.

The following command is all one line, then hit 'Enter':
connect –v nameOfVol.vol –x xDim –y yDim –z zDim –o nameOfVol.vol.connect

Use ls to verify that a new file is present → nameOfVol.vol.connect

At this stage, if you have done ALL steps (individual connected volumes for cortical compartment and trabecular compartment, and connected volume for a single material whole bone) you should have the following directory structure:

- SampleID (e.g., D01_L4)
    - SampleID_Whole (e.g., D01_L4_Whole)
        - All TIF files for the whole bone
        - tiff2vol.pro
        - SampleID.xx.yy.zz.zstart_zend.vol
        - SampleID.xx.yy.zz.zstart_zend.vol.connect
    - SampleID_Cortical (e.g. D01_L4_Cortical)
        - All TIF files for the cortical shell
        - tiff2vol.pro
        - SampleID_Cortical.xx.yy.zz.vol
        - SampleID_Cortical.xx.yy.zz.vol.connect
    - SampleID_Trabec (e.g. D01_L4_Trabec)
        - All TIF files for the trabecular compartment
        - tiff2vol.pro
        - SampleID_Trabec.xx.yy.zz.vol
        - SampleID_Trabec.xx.yy.zz.vol.connect

5. For a two material sample (whole bone)

Now we are going to move the .vol file from the Cortical directory into the Whole directory (as shown below).

Currently, you are here:

- SampleID (e.g. D01_L4)
  - SampleID_Whole (e.g. D01_L4_Whole)
    - All TIF files for the whole bone
    - tiff2vol.pro
    - SampleID.xx.yy.zz.zstart_zend.vol
  - SampleID_Cortical (e.g. D01_L4_Cortical)
    - All TIF files for the cortical shell
    - tiff2vol.pro
    - SampleID_Cortical.xx.yy.zz.vol
    - SampleID_Cortical.xx.yy.zz.vol.connect
  - SampleID_Trabec (e.g. D01_L4_Trabec)
    - All TIF files for the trabecular compartment
    - tiff2vol.pro
    - SampleID_Trabec.xx.yy.zz.vol
    - SampleID_Trabec.xx.yy.zz.vol.connect

Navigate to the Cortical directory and use cp to copy and transfer the .vol file:
cp SampleID_Cortical.xx.yy.zz.vol ../SampleID_Whole/ Hit 'enter'
Copy the volcheck.pro script into the SampleID_Whole directory.

Currently, you are here:

- SampleID (e.g. D01_L4)
  - SampleID_Whole (e.g. D01_L4_Whole)
    - All TIF files for the whole bone
    - tiff2vol.pro
    - SampleID.xx.yy.zz.zstart_zend.vol
    - SampleID_Cortical.xx.yy.zz.vol
    - volcheck.pro
  - SampleID_Cortical (e.g. D01_L4_Cortical)
    - All TIF files for the cortical shell
    - tiff2vol.pro
    - SampleID_Cortical.xx.yy.zz.vol
    - SampleID_Cortical.xx.yy.zz.vol.connect
  - SampleID_Trabec (e.g. D01_L4_Trabec)
    - All TIF files for the trabecular compartment
    - tiff2vol.pro
    - SampleID_Trabec.xx.yy.zz.vol
    - SampleID_Trabec.xx.yy.zz.vol.connect

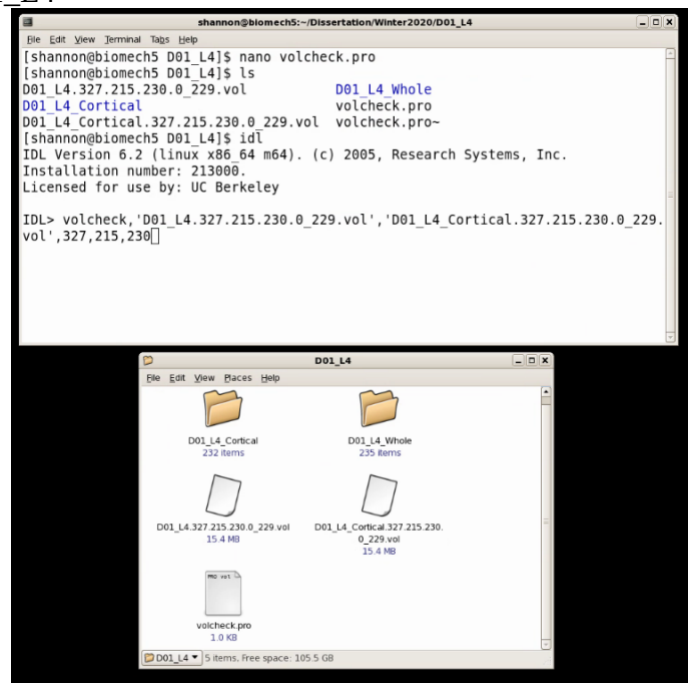
If you are interested in the contents of volcheck.pro, click here.

a. Merge .vol files using volcheck.pro

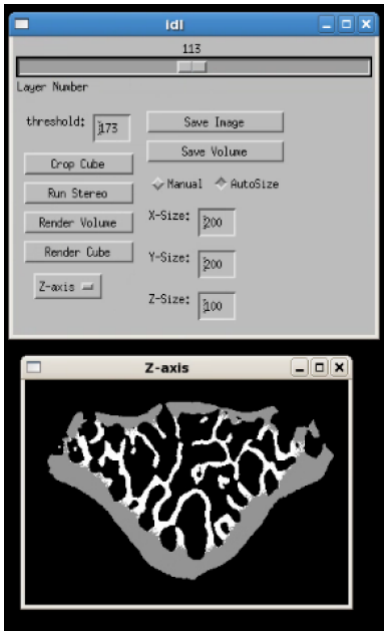
---------- START IDL ----------
In IDL, type the following to run the script. (Note: input format for this script is at the top of the volcheck.pro script → volcheck,oofile,ccfile,xx,yy,zz)
idl Hit 'Enter" ← enter IDL

volcheck,'whole-bone.vol','cortical.vol',xx,yy,zz Hit 'enter' ← see example**

**Example for D01_L4



Upon completion, a window will pop up enabling you to visualize how well the unet segmented the cortical bone.



Close the IDL popup windows. Type exit to exit IDL.

---------- END IDL ----------

Check to see that you have both a visual (vol.visual) and nonvisual (vol.nvisual) file in your directory.

At this stage, you should have the following directory structure:

- SampleID (e.g. D01_L4)
  - SampleID_Whole (e.g. D01_L4_Whole)
    - All TIF files for the whole bone
    - tiff2vol.pro
    - SampleID.xx.yy.zz.zstart_zend.vol
    - SampleID_Cortical.xx.yy.zz.vol
    - Volcheck.pro
    - SampleID.xx.yy.zz.zstart_zend.vol.nvisual
    - SampleID.xx.yy.zz.zstart_zend.vol.visual
  - SampleID_Cortical (e.g. D01_L4_Cortical)
    - All TIF files for the cortical shell
    - tiff2vol.pro
    - SampleID_Cortical.xx.yy.zz.vol
    - SampleID_Cortical.xx.yy.zz.vol.connect
  - SampleID_Trabec (e.g. D01_L4_Trabec)
    - All TIF files for the trabecular compartment
    - tiff2vol.pro
    - SampleID_Trabec.xx.yy.zz.vol
    - SampleID_Trabec.xx.yy.zz.vol.connect

b. Use connect to remove noise

Now you need to remove small isolated solid clusters (noise) that are not connected to the large solid cluster which is the entire vertebra. Use the following command to remove pieces of the model disconnected from the bone. Be sure to add .connect at the end, otherwise you will overwrite your original volume. Fill in the dimensions that match your sample.
Connect .nvisual using the connect program. The following command is all one line, then hit 'Enter'

connect –v nameOfVol.vol.nvisual –x xDim –y yDim –z zDim –o nameOfVol.vol.connect

Use ls to verify that a new file is present → nameOfVol.vol.connect

At this stage, you should have the following directory structure:

- SampleID (e.g. D01_L4)
  - SampleID_Whole (e.g. D01_L4_Whole)
    - All TIF files for the whole bone
    - tiff2vol.pro
    - SampleID.xx.yy.zz.zstart_zend.vol
    - SampleID.xx.yy.zz.zstart_zend.vol
    - SampleID_Cortical.xx.yy.zz.zstart_zend.vol
    - volcheck.pro
    - SampleID.xx.yy.zz.zstart_zend.vol.nvisual

        - SampleID.xx.yy.zz.zstart_zend.vol.visual
        - SampleID.xx.yy.zz.zstart_zend.vol.connect
    - SampleID_Cortical (e.g. D01_L4_Cortical)
        - All TIF files for the cortical shell
        - tiff2vol.pro
        - Sample_ID_Cortical.xx.yy.zz.vol
        - SampleID_Cortical.xx.yy.zz.vol.connect
    - SampleID_Trabec (e.g. D01_L4_Trabec)
        - All TIF files for the trabecular compartment
        - tiff2vol.pro
        - SampleID_Trabec.xx.yy.zz.vol
        - SampleID_Trabec.xx.yy.zz.vol.connect

6.2.7 Nonlinear FE Workflow and Protocol for Rat Vertebral Bodies

University of California, Berkeley
Berkeley Biomechanics Lab
Standard Operating Procedure

Nonlinear FE Workflow and Protocol for Rat VBs

SOP, Version 1.1
Date: February 2021

Author(s): Shannon Emerzian
Principal Investigator: Tony M. Keaveny

Summary: This protocol outlines the steps to create FE models from microCT scans, check the volume for connection, mesh, and run nonlinear analysis on Stampede2.
Key Words: finite element analysis, rat vertebral bodies, linear, nonlinear, Stampede2
Equipment:

- Access to Biomech5
- Access to TACC/Stampede2
    - https://portal.tacc.utexas.edu/user-guides/stampede2#accessing-the-system

Procedure:

1. Move .connect file to Stampede2
    a. Log in to Biomech5
    b. Move vol.connect to supercomputer.

Now these models need to be placed on the supercomputer so that they can be submitted with the supporting scripts.

--------Direct transfer: Biomech5 → Stampede2:

To transfer the connected volume (nameOfVol.vol.connect) to the supercomputer, open up a new terminal to access Stampede2 and find the directory you want to send the volume to. *Note: text in green is specific to your account; for Stampede2, your username is your TACC account username, your password will be your TACC account password, and the OTP is from the TACC Token app.*

ssh emerzian@stampede2.tacc.utexas.edu	Hit 'enter'
Password: {your password}	Hit 'enter'
TACC Token: OTP	Hit 'enter'

Find the path to the directory of choice in the supercomputer with the following commands:

cdw	This brings you to your working directory
ls	

In the working directory we will create a new directory for each sample and transfer the volume we created locally (the one we gzipped) to this new directory.

ls	
mkdir newDir	newDir is probably your sample ID, e.g. D01_L5
ls	Verify new directory is present
cd newDir	Change to newDir directory
pwd	This is the absolute path to your current directory, something like: /work/05030/emerzian/stampede2/newDir

Copy the path to your current working directory on Stampede2.

Switch over to the Terminal session you have opened locally (Biomech5) in the directory containing nameOfVol.vol.connect.gz. In order to transfer to Stampede2, we need to use a data transfer node (dtn). *Note: below, path is where you paste the path copied from Savio. This will look something like /work/05030/emerzian/stampede2/newDir*.

Type this all in one line:

scp nameOfVol.vol.connect emerzian@stampede2.tacc.utexas.edu:path Hit 'enter'

The supercomputer will ask for a Password and TACC Token again.

Navigate back to your terminal window for Stampede2. Use ls to verify the vol.connect file is in the directory you expect it to be in!

2. Nonlinear FE on Stampede2
    a. Mesh (Run "mesh.job")

Now that the .connect file is on Stampede2, close the Biomech5/local computer terminal(s) and find the .connect file on Stampede2 (Terminal session on local machine).

Move supporting files to the current directory (/newDir). These 3 files can be found in a previous study's directory. Copy over the files you need *Note: You will need to copy and paste these files into each new directory for each new job.*

```
cd ../old directory of folder with files to be copied/
cp mesh.job premesh.sh postmesh.sh ../newDir
```

Checklist:

- .connect file
- premesh.sh
- postmesh.sh
- mesh.job

Note: In order for "mesh.job" to run successfully, node_new_softlayer should be located (for me it is here: /home1/05030/emerzian/mesher/node_new_softlayer) and compiled.

Now we will build the sample mesh using "mesh.job". The input file is a connected volume (.vol.connect). There are two key steps to this job.

- "premesh.sh" → generates "input_softlayer", the collection of commands needed for node_new_softlayer (C program).
- "postmesh.sh" → does some housekeeping (renaming and removing garbage files, modifying the last section of the .feap file)

If successful, "mesh.job" will output the text input file for parFEAP.

→ If you are running a **two material** job
(i.e. your vol.connect file has a .vol from both whole bone and cortical bone), make sure your premesh.sh script calls for 2 materials (in red below).

nano premesh.sh Hit 'enter' ← opens mate in nano

premesh.sh

```
#!/bin/bash
# Tongge Wu | Shannon Emerzian
# Nov 20 2020
# Project: Rat Localized Irradiation
# WARNING: This is set for 15 um resolution, 2 materials!

# Shell script runs on Stampede2

# Generate meshing command for a given volume
# "input_softlayer" is the meshing command for "node_new_softlayer" mesher
# Input: (1).connect file name, (2)outputname (3-5)xyz dimension
# Output: "input_softlayerfile"

printf "$1\n$2\ny\n$2\nn\ny\n" > input_softlayer
printf "1e-6 1e-6 1e-6\n0 $3 0 $4 0 0\ny y\ny\ny\n" >> input_softlayer

# 2% compressive displacement boundary condition
# WARNING: (4 locations) 0.015 is the microCT resolution (in mm)
# WARNING: (1 location) 2 materials, second last printf
printf "0 0 %0.4f\n" $(bc -q <<< scale=5\;$5*0.015*-0.02) >> input_softlayer
```

```
printf "0 $3 0 $4 $5 $5\ny y\ny\nn\ny\n2\nn\ny\n" >> input_softlayer
printf "$3 $4 $5\n0.015 0.015 0.015\n1\n1\n1\n1\n1\n1\n4\n" >>input_softlayer
```

Hit 'control+x' ← exit nano

Save modified buffer? y Hit 'Enter' ← save changes

File Name to Write: premesh.sh Hit 'Enter' ← exit nano

First, update mesh.job.

nano mesh.job Hit 'enter' ← opens mesh.job in nano

The data to be adjusted each time you run this job are in **red** below.
mesh.job (input commands for node_new_softlayer, see details here)

```
#!/bin/bash
# Tongge Wu
# Shannon Emerzian
# Aug 6 2020
# Project: Rat Local Radiation
#-----------------------------------------------------
# SLURM job script to run node_new_softlayer on TACC Stampede2 SKX node.
#
# Usage: "sbatch mesh.job" on a Stampede2 login node
#
# Required input files: 1) .connect file
#-----------------------------------------------------
#SBATCH -J D07_L5_Mesh          # Job name {I like to use sample ID_Mesh}
#SBATCH -o SLURM_out.%j          # Output file
#SBATCH -e SLURM_err.%j          # Error file
#SBATCH -p skx-dev               # Queue (partition) name
#SBATCH -N 1                   # Total # of compute nodes (1 for serial)
#SBATCH -n 10                  # Total number of mpi tasks (processors)
#SBATCH -t 00:30:00              # Run time (hh:mm:ss), limit 48hr (normal queue)
#SBATCH -A TG-MCA00N019              # Account to charge against
#SBATCH --mail-user=semerzian@berkeley.edu  # Email notification {use your email}
#SBATCH --mail-type=ALL                # Notification types to be sent

# premesh ------------------------------
bash premesh.sh D07_L5.488.360.177.0_176.vol.connect D07_L5 488 360 177 ← change to your .connect volume, sampleID, x-dim, y-dim, z-dim
# meshing process ------------------------------------
/home1/05030/emerzian/mesher/node_new_softlayer/node_new_softlayer < input_softlayer ← Make sure you are pointing to the correct directory in your account for node_new_softlayer. Also make sure you have not changed the name of input_softlayer (above). Any changes need to be modified here.
# postmesh --------------------------------------
bash postmesh.sh D07_L5    ← change to your sample ID
```

Hit ‘control+x’		← exit nano
Save modified buffer? y	Hit ‘Enter’	← save changes
File Name to Write: mesh.job	Hit ‘Enter’	← exit nano

We are ready to submit the job!

```
sbatch mesh.job
```

You can check the status of your job (you’ll also get emails):

```
squeue -u emerzian
```
← will be your TACC username (note: alias sq)

This should take ~5 minutes.

Record the run time.

Using less, check SLURM_err and SLURM_out files.

```
less SLURM_err.jobID
```

SLURM_err should be empty (no errors).

```
less SLURM_out.jobID
```

SLURM_out should have information from input_softlayer, as well as the number of elements and nodes.

Record the number of nodes and elements.

b. Solve (Run “olympus.job”)

Move supporting files to the current directory (/newDir). These 3 files can be found in a previous study’s directory. Copy over the files you need *Note: You will need to copy and paste these files into each new directory for each new job.*

```
cd ../old directory of folder with files to be copied/
cp olympus.job mate solv .petscrc ../newDir
```

Checklist:

- .feap file → output of ‘node_new_softlayer’
- Img link → e.g. 96 domains will give you Img96

- files/ → directory to save O, F, L files from FEAP
- mate → user 30 element, bilinear failure mode
- .petscrc → contains all numerical detail, especially
    - ksp_rtol: linear solver relative tolerance
    - ksp_max_it: linear solver max iteration
    - ksp_type cg: use conjugate gradient linear solver
    - olympus_nl_tol: newton-raphson convergence tolerance
    - olympus_max_nl_its: newton-raphson nonlinear solver max iteration
    - olympus_nstep: number of time step
    - olympus_dt: time step
- solv → contains all solving commands for FEAP (usually you don't need to touch this)
- olympus.job

Now we are ready to run the nonlinear FE analysis using "olympus.job". If successful, "olympus.job" will output a text file with FEA results (stress, strain) for analysis in Matlab.

→ If you are running a **two material** job
(i.e. your vol.connect file has a .vol from both whole bone and cortical bone), make sure your mate file has 2 materials.

nano mate Hit 'enter' ← opens mate in nano

```
para
E = 10        # modulus (GPa)
K = 833.333*E      # bulk modulus (MPa)      -> K = E / (3*(1-2v)) * 10^3
G = 384.615*E      # shear modulus (MPa)      -> G = E / (2*(1+v)) * 10^3
c = 5.7*E       # compressive yield strain      -> = (c + t) / (10 E) in %
t = 2.4*E       # tensile yield strain     -> = (c - t) / (10 E) in %

mate,1
user,30
5,0,0
orth,K,G,G,G,G,G,0,0,0
plast,c,0,1,0,0,0,t
1.0,1.0,1.0,1.0,1.0,0.1*G,0.1*G,0.1*G,0.1*G,0.1*G
1.0,0.0,0.0,0.0,0.0,1.0,0.0

mate,2
user,30
5,0,0
orth,K,G,G,G,G,G,0,0,0
plast,c,0,1,0,0,0,t
1.0,1.0,1.0,1.0,1.0,0.1*G,0.1*G,0.1*G,0.1*G,0.1*G
1.0,0.0,0.0,0.0,0.0,1.0,0.0
```

Hit ‘control+x’		← exit nano
Save modified buffer? y	Hit ‘Enter’	← save changes
File Name to Write: mesh.job	Hit ‘Enter’	← exit nano

Update olympus.job.

nano olympus.job	Hit ‘enter’	← opens olympus.job in nano

The data to be adjusted each time you run this job are in **red** below.

olympus.job

```
#!/bin/bash
# Tongge Wu
# Shannon Emerzian
# Aug 6 2020
# Project: Rat Local Radiation
#----------------------------------------------------
# SLURM job script to run Olympus on TACC's Stampede2 SKX nodes.
#
# Run "sbatch olympus.job" on a Stampede2 login node
#----------------------------------------------------
#SBATCH -J D12_07_Solve           # Job name {I like to use sample ID_Solve}
#SBATCH -o SLURM_out.%j           # Output file
#SBATCH -e SLURM_err.%j           # Error file
#SBATCH -p skx-normal             # Queue (partition) namew
#SBATCH -N 2                      # Total # of compute nodes (1 for serial, 2 for parallel)
#SBATCH -n 96                     # Total number of mpi tasks (processors)
#SBATCH -t 01:00:00               # Run time (hh:mm:ss)
#SBATCH -A TG-MCA00N019           # Account to charge against
#SBATCH --mail-user=semerzian@berkeley.edu       # Email notification
#SBATCH --mail-type=ALL                          # Notification types to be sent

cat olympus.job .petscrc solv
date
set -x

# Launch Olympus code
ibrun /home1/05030/emerzian/olympus-keaveny/Olympus/olympus.${PETSC_ARCH} -athena_temp_dir ./files
date
```

Hit ‘control+x’		← exit nano
Save modified buffer? y	Hit ‘Enter’	← save changes
File Name to Write: mesh.job	Hit ‘Enter’	← exit nano

Now, update .petscrc with model parameters.

nano .petscrc Hit ‘enter’ ← opens .petscrc in nano

The data to be adjusted each time you run this job are in **red** below.

.petscrc

```
#-olympus_solid_type 2              # MA added
-athena_use_solv_file
-athena_proc_node 1
-pc_type mg                    # pre-conditioner type
-pc_mg_type multiplicative          # from old .petscrc
-aggmg_smooths 1
-pc_mg_smoothdown 2
-pc_symmetric                  # ADDED from old .petscrc
-pc_mg_cycles 1                # ADDED from old .petscrc
-mg_levels_ksp_type chebychev
# -mg_levels_pc_type nodal_asm      # nodal asm
#-aggmg_use_aggragate_blocks       # include when using nodal asm
-mg_levels_pc_type gs             # gauss-seidel
-prometheus_tol_2 1.0e-01
-ksp_rtol 1.0e-04
-ksp_max_it 200
-ksp_monitor                  # ADDED from old .petscrc
-aggmg_factor2 1.0             # from old .petscrc
-prometheus_random_mis
-prometheus_top_grid_limit 1500            # from old .petscrc
#-prometheus_reuse_matrix_factors 10        # NOT in old .petscrc
-aggmg_avoid_resmooth
-ksp_type cg
-log_view
-options_left
-out_verbose 2                # verbosity of output file (ie use 5 for more info)
-olympus_nl_tol 1.e-4           # use for non-linear jobs
# -olympus_nl_tol 1.e-8          # use for linear jobs
-olympus_max_nl_its 10
-olympus_nstep 20             # number of solution steps
-olympus_dt 0.05             # time step. (n_step * dt) needs to = 1
-olympus_out_stre            # outputs element stresses
-olympus_out_db              # outputs .DB files (VisIt)
-mat_aij_inode_limit 3          # ADDED from old .petscrc
-prometheus_mis_levels 2        # ADDED from old .petscrc
-prometheus_preduce_base 500      # ADDED from old .petscrc
#!-pc_mg_smoothup 2          # ADDED from old .petscrc
```

We are ready to submit the job!

sbatch olympus.job

You can check the status of your job (you’ll also get emails):

squeue -u semerzian ← will be your TACC username (note: alias sq)

This should take ~60 minutes.

Once the job has completed (queue appears empty / you get an email alerting you of its completion), check the output files.

Use ls to check the output files. You will see many: input files (e.g. ID01_L5, and 0000 through 0096, one for each of the prescribed domains), output files (e.g. OD01_L5, and 0000 through 0096), log files (e.g. LD01_L5, and 0000 through 0096), a new slurm file, feapname files, input_softlayer, and a solve file (solve.D01_L4).

First, check that all of the solution steps you prescribed (olympus_nstep) are present, and that none of the steps has maxed out the number of prescribed max iterations (ksp_max_it and olympus_max_nl_its).
→ Success? Continue.
→ Fail? Proceed to next step (#3. Resubmitting jobs).

Record run time.

Proceed with MATLAB and VisIt post-processing.

3. Resubmitting jobs

***IF THERE IS AN ISSUE WITH CONVERGENCE, try these adjustments in the order listed.

0) Try running again (no change to .petscrc)

If rerunning does not work, update your .petscrc file:

1) Update olympus_nstep AND olympus_dt
* NONLINEAR max iterations *
What is happening:
- Number of time steps is too coarse
What to do:
- increase number of time steps
- WARNING: be sure to update BOTH nstep and dt such that nstep*dt = 1
- common nstep/dt options:
20/0.05
25/0.04
40/0.025
50/0.02
80/0.0125

2) Update ksp_rtol

* LINEAR solver tolerance *

What is happening:

- allows solving of Ax=B in a more accurate manner
- x --> delta --> update for N-R solver

What to do:

- decrease this value (1e-3 to 1e-4; 1e-3 to 0.5e-3) by one order or half order of magnitude

3) Update olympus_nl_tol

* NONLINEAR solver tolerance *

What is happening:

- how accurate solution is for nonlinear solution f(u)=0 (how close is u to letting f(u)=0)

What to do:

- change: either increase nl_its or decrease nl_tol
- if solver always reaches max_nl_its (10), it is too strict on nl_tol; need to EITHER

→ increase max_nl_its (10 to 20)

OR

→ increase nl_tol (convergence will be less accurate at each nl step); options: 1E-4, 1E-3

Notes:

ksp_max_its = 200 ---> don't touch this; want to keep # iterations low

If you are always reaching the max number of iterations (either ksp_max_it or olympus_max_nl_its), then you are requiring the solver to be too accurate; need to reduce the accuracy (too strict! not giving sufficient number of iterations to achieve tight tolerance)

SO either increase # iterations so solver can achieve high accuracy OR increase tolerance (convergence will be less accurate)

If you relax tolerance, your solution at each timestep will be less accurate compared to "true" solution (f(u) is not as close to zero as it could be)

SOP APPENDIX 1: Questions for node_new_softlayer that input_softlayer is answering:

Input data file:
Output file name:0
Output FEAP file for this volume (y/n)? y
Enter the heading of FEAP file:
Do you want to apply load on the model? (y/n):n
Do you want to apply disp on the model? (y/n): y
Enter the total disp in X,Y,Z directions: 0 0 1e-6
Enter Xmin, Xmax, Ymin, Ymax, Zmin, Zmax locations: 0 540 0 540 0 0
Is Zmin, Zmax surface: y y
Do you want to search in both x and y direction: y
Do you want to apply disp again? (y/n): y
Enter the total disp in X,Y,Z directions: 0 0 .456 (in millimeters)
Enter Xmin, Xmax, Ymin, Ymax, Zmin, Zmax locations: 0 540 0 540 127 127
Is Zmin, Zmax surface: y y
Do you want to search in both x and y direction: y
Do you want to apply disp again? (y/n): n
Do you have any material cards? (y/n): y
Enter total number of material cards: 3
Do you have soft layers in the model? (y/n): n
Output boundary nodes for this volume? (y/n): y
Enter the size of the array Number of pixels in the X,Y,Z directions: 540 540 127
Enter the pixel dimensions (mm) X, Y, Z dimensions: 0.074 0.074 0.074 (these are in millimeters)
Enter the modulus (Mpa): 1
Enter the Poisson's ratio: 1
Enter the maximum number of iterations: 1
Enter the covergence tolerance: 1
Enter the output frequency: 1
Select the desired boundary condition:

1. Simple compression and tension
2. Confined compression or tension
3. Simple shear stress
4. Confined shear strain
5. Combined compressive and shear strain

Enter your selection: 1
Select the loading direction:

1. X
2. Y
3. Z
4. Done

Enter your selection: 4

SOP APPENDIX 2: How to calculate the number of domains needed on Savio/Stampede

Here we will calculate the total number of nodes and number of processors. First, find the number of nodes in the entire volume by using the command:

head -n 10 sampleID.feap

Line 2 will display the following information in this order:

[# nodes] [# elements] [# materials] [spatial dimension] [max # DOF per node] [max # nodes per element]

Example:

```
[semerzian@ln003 D01_L4]$ head -n 10 D01_L4.feap
FEAP D01_L4
 4434070  3701083     2     3     3     8  ← line we are interested in, listed as above

nopr
nopa
nocr

COORDinates ALL
    1 0 2.2200000e+00 4.0500000e-01 0.0000000e+00
```

Multiply the number of nodes by the number of DOF per node

[# nodes] * [max # DOF per node] = [~ # DOF]

Ex. 4434070 * 3 = 13302210 ← approximate number of DOF

To get the number of processors this job requires, take the number of degrees of freedom and divide by 150,000 (rough number of DOF each processor can handle based on previous calculations. Note: this could be optimized with a scalability study).

[~ # DOF] / [150,000 DOF/processor] = [# processors]

Ex. 13302210 / 150,000 = 88.68 ← approximate number of processors

To get the total number of compute nodes needed for the job, divide the number of processors by 24, the total number of cores/compute node on savio2.

[# processors] / [24 cores/compute node] = [# compute nodes needed]

Ex. 88.68 / 24 = 3.7 ~ 4 ← number of compute nodes required

Now multiply the number of compute nodes required by the number of cores (total number of cores/cmopute node on savio2).

[# compute nodes] * [# cores/compute node on super computer] = [# processors]

Ex. 4 * 24 = 96 ← number of domains

SOP APPENDIX 3: Job Scripts for Stampede2 (Nonlinear analyses)

Premesh.sh

```
#!/bin/bash
# Tongge Wu | Shannon Emerzian
# Oct 9 2020
# Project: Rat Localized Irradiation
# WARNING: This is set for 15 um resolution, 1 material!

# Shell script runs on Stampede2

# Generate meshing command for a given volume
# "input_softlayer" is the meshing command for "node_new_softlayer" mesher
# Input: (1).connect file name, (2)outputname (3-5)xyz dimension
# Output: "input_softlayerfile"

printf "$1\n$2\ny\n$2\nn\ny\n" > input_softlayer
printf "1e-6 1e-6 1e-6\n0 $3 0 $4 0 0\ny y\ny\ny\n" >> input_softlayer
# 2% compressive displacement boundary condition
# WARNING: (4 locations) 0.015 is the microCT resolution (in mm)
# WARNING: (1 location) 1 material, second last printf
printf "0 0 %0.4f\n" $(bc -q <<< scale=5\;$5*0.015*-0.02) >> input_softlayer
printf "0 $3 0 $4 $5 $5\ny y\ny\nn\ny\n1\nn\ny\n" >> input_softlayer
printf "$3 $4 $5\n0.015 0.015 0.015\n1\n1\n1\n1\n1\n1\n4\n" >>input_softlayer
```

Postmesh.sh

```
#!/bin/bash
# Tongge Wu | Shannon Emerzian
# Oct 9 2020
# Project: Rat Localized Irradiation
# WARNING: 96 domains

# Shell script runs on Stampede2

# clean the files
mv $1.feap I$1
rm $1
rm $1.[a-z]*
mv I$1 $1.feap

# create link for 96 domains
ln -s $1.feap Img96
# create output folder
mkdir files/
```

Mate

```
para
E = 10        # modulus (GPa)
K = 833.333*E     # bulk modulus (MPa)      -> K = E / (3*(1-2v)) * 10^3
G = 384.615*E     # shear modulus (MPa)      -> G = E / (2*(1+v)) * 10^3
c = 5.7*E       # compressive yield strain      -> = (c + t) / (10 E) in %
t = 2.4*E       # tensile yield strain     -> = (c - t) / (10 E) in %

mate,1
user,30
5,0,0
orth,K,G,G,G,G,G,0,0,0
plast,c,0,1,0,0,0,t
1.0,1.0,1.0,1.0,1.0,0.1*G,0.1*G,0.1*G,0.1*G,0.1*G
1.0,0.0,0.0,0.0,1.0,0.0
```

Solv

```
macr
prop,,1
end
2,1
0.0,  .0
10.0, 10.0
```

Olympus.job

```
#!/bin/bash
#----------------------------------------------------
# SLURM job script to run Olympus on TACC's Stampede2 SKX nodes.
#
# Run "sbatch olympus.job" on a Stampede2 login node
#----------------------------------------------------
#SBATCH -J D08_L5              # Job name
#SBATCH -o SLURM_out.%j               # Output file
#SBATCH -e SLURM_err.%j               # Error file
#SBATCH -p skx-normal                 # Queue (partition) namew
#SBATCH -N 2                  # Total # of compute nodes (1 for serial)
#SBATCH -n 96                  # Total number of mpi tasks (processors)
#SBATCH -t 06:30:00                # Run time (hh:mm:ss)
#SBATCH -A TG-MCA00N019               # Account to charge against
#SBATCH --mail-user=semerzian@berkeley.edu       # Email notification
#SBATCH --mail-type=ALL               # Notification types to be sent

cat olympus.job .petscrc solv
date
set -x

# Launch Olympus code
ibrun /home1/05030/emerzian/olympus-keaveny/Olympus/olympus.${PETSC_ARCH} -athena_temp_dir ./files
date
```

.petscrc

```
#-olympus_solid_type 2             # MA added

-athena_use_solv_file
-athena_proc_node 1
-pc_type mg                   # pre-conditioner type
-pc_mg_type multiplicative           # from old .petscrc
-aggmg_smooths 1
-pc_mg_smoothdown 2
-pc_symmetric                 # ADDED from old .petscrc
-pc_mg_cycles 1                # ADDED from old .petscrc
-mg_levels_ksp_type chebychev
# -mg_levels_pc_type nodal_asm      # nodal asm
#-aggmg_use_aggragate_blocks       # include when using nodal asm
-mg_levels_pc_type gs             # gauss-seidel
-prometheus_tol_2 1.0e-01
-ksp_rtol 5.0e-04
-ksp_max_it 200
-ksp_monitor                  # ADDED from old .petscrc
-aggmg_factor2 1.0             # from old .petscrc
-prometheus_random_mis
-prometheus_top_grid_limit 1500            # from old .petscrc
#-prometheus_reuse_matrix_factors 10        # NOT in old .petscrc
```

```
-aggmg_avoid_resmooth
-ksp_type cg
-log_view
-options_left
-out_verbose 2                # verbosity of output file (ie use 5 for more info)
-olympus_nl_tol 1.e-4          # use for non-linear jobs
# -olympus_nl_tol 1.e-8        # use for linear jobs
-olympus_max_nl_its 10
-olympus_nstep 40             # number of solution steps
-olympus_dt 0.025             # time step. (n_step * dt) needs to = 1
-olympus_out_stre             # outputs element stresses
-olympus_out_db              # outputs .DB files (VisIt)
-mat_aij_inode_limit 3        # ADDED from old .petscrc
-prometheus_mis_levels 2      # ADDED from old .petscrc
-prometheus_preduce_base 500  # ADDED from old .petscrc
#!-pc_mg_smoothup 2          # ADDED from old .petscrc
```

SOP APPENDIX 4: Script information

volcheck.pro

```
PRO volcheck,oofile,ccfile,xx,yy,zz
;Tongge Wu | Shannon Emerzian
;Nov 2020
;Project: Rat Local IR

;IDL script runs at local workstation
;for given original and cortical volumes, turn cortical to 150b (mid-grey) and 2b (invisible)
;oofile, original file
;ccfile, cortical file
;xx yy zz are dimensions of this sample
;output: two volume files
;'.visible' is for checking trabecular and cortical separation.
;'.invisible' is for later connecting process, the real model

;load two volumes
oofilename=oofile
ccfilename=ccfile
read_bindat,oofilename,oo,xx,yy,zz
read_bindat,ccfilename,cc,xx,yy,zz

;turn to 150b
for i=0,xx-1 do begin & for j=0,yy-1 do begin & for k=0,zz-1 do begin & if (cc(i,j,k) gt 0) then (oo(i,j,k) = 150b)
& endfor & endfor & endfor
temp=oofilename+'.visual'
scanvol,oo
;generate checking file
write_bindat,temp,oo

;turn to 2b
```

```
for i=0,xx-1 do begin & for j=0,yy-1 do begin & for k=0,zz-1 do begin & if (cc(i,j,k) gt 0) then (oo(i,j,k) = 2b) &
endfor & endfor & endfor
temp=oofile + '.nvisual'
;generate modeling file
write_bindat,temp,oo

end
```

SOP APPENDIX 5: Generic UNIX/IDL Information

UNIX COMMANDS:

- ls lists the files in a directory
- cd <directory name> changes from current directory to the directory called directory_name. Include the full path, do not include the < >
- cd .. goes back one directory. cd ../../ goes back two directories, and so on
- up arrow recalls previous commands
- pwd reports your current directory
- If you want to copy and paste, double click to highlight and copy, and press center scroll button to paste

IDL COMMANDS:

If at any point IDL presents an error indicating it cannot find the necessary scripts, do the following. Enter IDL and type:

PREF_SET,'IDL_PATH','+$HOME/idl:+/usr/local/idl:<IDL_DEFAULT>',/COMMIT

6.2.8 Nonlinear FEA Post-Processing with MATLAB

University of California, Berkeley
Berkeley Biomechanics Lab
Standard Operating Procedure

Nonlinear FEA Post-Processing with MATLAB

SOP, Version 1
Date: September 16, 2020

Author(s): Shannon Emerzian, Tongge Wu
Principal Investigator: Tony M. Keaveny

Summary: This protocol outlines the steps to run a basic MATLAB analysis on the outputs from Olympus.
Key Words: finite element analysis, rat vertebral bodies, MATLAB
Materials:

- Raw output files in files/ (O files = data for each domain, all time steps)
- MATLAB scripts/functions on Stampede (written by TW):
    - Ofile2rawfile shell script
        - namelist.txt → list all names of files you want to analyze
        - Ofile2rawfile.sh → an awk script to extract stress data from O_a files for Matlab processing
        - O2raw.job → job script file to run as a batch
    - Main MATLAB script (Matlab on Stampede2)
        - main.m → get all data at each time step for all domains
            - a_FEA2burn.m → convert to .mat file with useable data
            - b_zload.m → force in z-direction
    - Compute strength on MATLAB (local computer)
        - main_nonlinearFEA.m
            - b_yield.m → strength

Equipment:

- Access to Stampede2
    - Username (e.g. emerzian)
    - Password
    - TACC Token (OTP)
- Access to MATLAB on Stampede2
    - https://portal.tacc.utexas.edu/software/matlab#example1

Procedure:

1. Move files from your local machine to Stampede2.

Begin a Terminal session on your local machine. Navigate to the directory containing the MATLAB scripts listed above. *Note: It is easiest to edit these scripts locally and then reupload to Savio.*

Use tar to compress all scripts/MATLAB files in current directory:

```
tar cf post-scripts.tar *
```

Now, start an sftp session for Stampede2. We will use sftp to move files from the local machine to Stampede2 Note: text in green is specific to your account; for Stampede2, your username is your TACC account username, your password will be your TACC account password and the OTP is from the TACC Token app.

```
sftp emerzian@stampede2.tacc.utexas.edu          Hit 'enter'

Password: {your password}                        Hit 'enter'

TACC Token: OTP                                  Hit 'enter'
```

Put all files in the scratch directory (/scratch/05030/emerzian).

```
put *
```

Use cp or mv to relocate files to their proper directories, as described below:

File locations:

namelist.txt = in the directory containing all of the sample directories listed in the text file. (e.g. /scratch/05030/emerzian/spring2021/whole/)

Ofile2rawfile.sh = in the parent directory of namelist.txt (/scratch/05030/emerzian/spring2021)

All MATLAB scripts (.m files) = a directory for post-processing (e.g. /scratch/05030/emerzian/matlab-post)

2. Convert FEAP O files to a "rawfile" of usable data
   a. Update files/scripts.

Update the scripts by changing the entries that are highlighted in red (below) to match your sample/situation.

→ Example: I want to run all of the samples in /test1. So I put the path to test1 in Ofile2rawfile.sh and make sure namelist.txt contains a list of all samples in test1 (D01-D03).

Ofile2rawfile.sh

```
#!/bin/bash
path=/scratch/05030/emerzian/winter2020   ← directory containing all of your samples
for i in $(cat $path/namelist.txt); do
{
cd $path/$i/files/
touch "$i"_readme.txt
awk '/%SIG/{print FILENAME,"\t"$2"\t"$3"\t"$4"\t"$5"\t"$6"\t"$9}' O_a* > "$i"_nlFEAraw
}
done
```

namelist.txt

```
D01_L4     ← Update this file with the name of all samples you are analyzing
D01_L5       These are all located in the directory called in Ofile2rawfile.sh
D02_L4
D02_L5
D03_L4
D03_L5
```

b. Verify Ofile2rawfile.sh is working.

Before running the full script, we will first verify we are properly locating all the proper directories. First, comment out the "awk" line in Ofile2rawfile.sh.

nano Ofile2rawfile.sh Hit 'enter'

Ofile2rawfile.sh

```
#!/bin/bash
path=/scratch/05030/emerzian/spring2021/whole   ← directory containing all of your samples
for i in $(cat $path/namelist.txt); do
{
cd $path/$i/files/
touch "$i"_readme.txt
# awk '/%SIG/{print FILENAME,"\t"$2"\t"$3"\t"$4"\t"$5"\t"$6"\t"$9}' O_a* > "$i"_nlFEAraw   ← #
used to comment out this line (for now)
}
done
```

bash Ofile2rawfile.sh Hit 'enter'

Move to directories/files/ in namelist.txt and verify that each contains a file called *_readme.txt (* = sample ID, e.g. D01_L4). If not, correct any path issues in Ofile2rawfile.sh and run again.

c. Run Ofile2rawfile.sh as a batch job (easiest) or in an interactive session

------as a batch job

Navigate to the directory containing Ofile2rawfile.sh (e.g. /scratch/05030/emerzian/). In order to run the full script, we need to remove the comment we added on the "awk" line in Ofile2rawfile.sh.

nano Ofile2rawfile.sh Hit 'enter'

Ofile2rawfile.sh

```
#!/bin/bash
path=/scratch/05030/emerzian/winter2020
for i in $(cat $path/namelist.txt); do
{
cd $path/$i/files/
touch "$i"_readme.txt
awk '/%SIG/{print FILENAME,"\t"$2"\t"$3"\t"$4"\t"$5"\t"$6"\t"$9}' O_a* > "$i"_nlFEAraw  ← remove
# used to comment out this line on the previous step
}
done
```

Edit job script

O2raw.job

```
#!/bin/bash
#----------------------------------------------------
# SLURM job script to run Ofile2rawfile.sh on TACC Stampede2 SKX node.
#
# Usage: "sbatch O2raw.job" on a Stampede2 login node
#
# Required input files: FEAP output files for all domains/timesteps
#----------------------------------------------------
#SBATCH -J test2_rawfile              # Job name
#SBATCH -o SLURM_out.%j               # Output file
#SBATCH -e SLURM_err.%j               # Error file
#SBATCH -p skx-normal              # Queue (partition) name
#SBATCH -N 1                  # Total # of compute nodes (1 for serial)
#SBATCH -n 48                  # Total number of mpi tasks (processors)
#SBATCH -t 02:00:00              # Run time (hh:mm:ss), limit 48hr (normal queue)
#SBATCH -A TG-MCA00N019              # Account to charge against
#SBATCH --mail-user=semerzian@berkeley.edu      # Email notification
#SBATCH --mail-type=ALL              # Notification types to be sent
```

```
# run shell script ------------------------------
bash Ofile2rawfile.sh
```

sbatch O2raw.job Hit 'enter'

You can monitor the progress in a new terminal with squeue emerzian.

Skip to the next step.

-----or as an interactive session

In order to run these scripts with the large output files, we need an interactive node on Stampede2 (https://portal.tacc.utexas.edu/user-guides/stampede2#citizenship-loginnodes-examples)

Open up a new terminal to access Stampede2.

ssh emerzian@stampede2.tacc.utexas.edu Hit 'enter'

Password: {your password} Hit 'enter'

TACC Token: OTP Hit 'enter'

Now, begin the interactive session with idev. NOTE: The default for "idev" (i.e. if you just run "idev" without any flags) is on the development queue with a 30 minute time cap. Here I am setting it to run on the normal queue (-p normal), for a 2 hour session (-t 02:00:00) with 68 tasks per node (-tpn 68) on 1 node (-N 1). See https://portal.tacc.utexas.edu/user-guides/stampede2#running-idev or idev --help for more information.

idev -p normal -t 02:00:00 -tpn 68 -N 1 Hit 'enter'

After some verifications and checks by Stampede2, idev session will open.

Navigate to the directory containing Ofile2rawfile.sh (e.g. /scratch/05030/emerzian/). In order to run the full script, we need to remove the comment we added on the "awk" line in Ofile2rawfile.sh.

nano Ofile2rawfile.sh Hit 'enter'

Ofile2rawfile.sh

```
#!/bin/bash
path=/scratch/05030/emerzian/test1   ← directory containing all of your samples
for i in $(cat $path/namelist.txt); do
{
```

```
cd $path/$i/files/
touch "$i"_readme.txt
awk '/%SIG/{print FILENAME,"\t"$2"\t"$3"\t"$4"\t"$5"\t"$6"\t"$9}' O_a* > "$i"_nlFEAraw  ← remove
# used to comment out this line on the previous step
}
done
```

bash Ofile2rawfile.sh Hit 'enter'

You can monitor the progress in a new terminal with squeue emerzian.

3. Convert nlFEAraw to .mat file
   a. Move all *_nlFEAraw files to MATLAB post-processing directory

   Note: You must have access to MATLAB on Stampede2 in order to proceed. See https://portal.tacc.utexas.edu/software/matlab#example1 for details.

   The easiest way to move all *_nlFEAraw files from their current directories (e.g. /scratch/05030/emerzian/test1/D01_L4/files) to the matlab post-processing directory (e.g. /scratch/05030/emerzian/matlab-post) is to use a shell script. Update this script for your situation.

   nano move.sh Hit 'enter'

   move.sh

```
for ID in {01..03}
        do
        for level in L4 L5
                do
                        cd /scratch/05030/emerzian/test2/D${ID}_${level}/files/
                        cp D${ID}_${level}_nlFEAraw /scratch/05030/emerzian/matlab-post
        done
done
```

   bash move.sh Hit 'enter'

   Before running the main.m (our MATLAB script), we need to update it. This is easiest to do locally on MATLAB. In the main.m script, you will need to update group.ID and group.nstep. See screenshot below for syntax.

   **Important: make sure you have the appropriate nstep value for each sample!!

   ** Important: If you are running a 2 material model, make sure you are using the 2 material script!

Save this file with all updates!

In a new Terminal window on your local machine, navigate to the directory containing the main.m file you just updated. Start an sftp session to move files from the local machine to Stampede2 *Note: text in green is specific to your account; for Stampede2, your username is your TACC account username, your password will be your TACC account password and the OTP is from the TACC Token app.*

sftp emerzian@stampede2.tacc.utexas.edu	Hit 'enter'
Password: {your password}	Hit 'enter'
TACC Token: OTP	Hit 'enter'

Put all files in the MATLAB post-processing directory with the *_nlFEAraw files (e.g. /scratch/05030/emerzian/matlab-post).

put main.m

Once all *_nlFEAraw files are in the matlab-post directory and main.m has been updated, update the matlab.job file:

matlab.job

```
#!/bin/bash
#
#----------------------------------------------------------------------------------
# SLURM job script to run Matlab on TACC's Stampede2
#
#
# DO THIS: Run "sbatch matlab.job" on Stampede2.
#
#----------------------------------------------------------------------------------
#
#SBATCH -J test1_post_matlab           # Job name
#SBATCH -e SLURM.%j.err              # Error file name
#SBATCH -o SLURM.%j.out               # Output file name
#SBATCH -p skx-normal                # Queue (partition) name
#SBATCH -N 1                      # Total # of compute nodes (1 for serial)
#SBATCH -n 16                      # Request all 16 cores
#SBATCH -t 05:00:00                  # Max run time (hh:mm:ss)
#SBATCH -A TG-MCA00N019                  # Account to charge against
#SBATCH --mail-user=semerzian@berkeley.edu         # Email notification
#SBATCH --mail-type=ALL                  # Notification types to be sent
#
# Command(s) to run ----------------------------------------------------------------
module load matlab
matlab -nodesktop -nodisplay -nosplash < main.m
```

sbatch matlab.job Hit ‘enter’

4. Move .mat files from Stampede2 to your local machine.

Open a Terminal window and log into Stampede2. Navigate to the directory with all of the .mat files. Use tar to compress all .mat files in current directory:

tar cf matlab-nl.tar *.mat

Open a second Terminal session on your local machine. Navigate to the directory where you would like to save the .mat files. Now, start an sftp session for Stampede2. We will use sftp to move files from Stampede2 to our local machine. *Note: text in green is specific to your account; for Stampede2, your username is your TACC account username, your password will be your TACC account password and the OTP is from the TACC Token app.*

sftp emerzian@stampede2.tacc.utexas.edu Hit ‘enter’

Password: {your password} Hit ‘enter’

TACC Token: OTP Hit ‘enter’

Navigate to the directory containing the .mat files (/scratch/05030/emerzian/matlab-post).

cd /scratch/05030/emerzian/matlab-post

get matlab-nl.tar

```
#!/bin/bash
#
#-----------------------------------------------------------------------------------
# SLURM job script to run VisIt on TACC's Stampede2
#
#
# DO THIS: Run "sbatch visit-fail.job" on Stampede2.
#
#-----------------------------------------------------------------------------------$
#
#SBATCH -J visit-D02              # Job name
#SBATCH -e SLURM.%j.err           # Error file name
#SBATCH -o SLURM.%j.out           # Output file name
#SBATCH -p skx-normal             # Queue (partition) name
#SBATCH -N 1                      # Total # of compute nodes (1 for seri$
#SBATCH -n 16                     # Request all 16 cores
#SBATCH -t 01:00:00               # Max run time (hh:mm:ss)
#SBATCH -A TG-MCA00N019           # Account to charge against
#SBATCH --mail-user=semerzian@berkeley.edu     # Email notification
#SBATCH --mail-type=ALL           # Notification types to be sent
#
# Command(s) to run ----------------------------------------------------------------$
module load intel/18.0.0
module load impi/18.0.0
```

```
module load swr
module load visit/2.13.2
visit -nowin -cli -s mainFailureCount.py
```

6.2.9 Compressive Testing of Whole Rat Vertebrae on the MTS

University of California, Berkeley
Berkeley Biomechanics Lab
Standard Operating Procedure

Compressive Testing of Whole Rat Vertebrae on the MTS

SOP, Version 2
Date: 12/18/2020

Author(s): Shannon Emerzian
Principal Investigator: Tony M. Keaveny

Summary: This protocol summarizes the method for compressive testing of whole rat vertebral bodies with endplates removed.
Key Words: rat vertebral bodies, mechanical testing, MTS
Materials:

- Rat vertebrae
- Absorbent pads
- 1X PBS
- Tweezers

Equipment:

- Digital calipers
- MTS
    - Bottom platen
    - Spherically seated top platen
    - 1” extensometer (SN: 2103)
    - 250-lb load cell (SN: M3337)

Procedure:

1. Preparation (~12 hours)
    1.1. If frozen (-20°C), thaw
        1.1.1. Thaw in the refrigerator (4°C) overnight. Keep VB in their storage tube during thaw.
        1.1.2. After overnight thaw, submerge VB in room temperature 1x PBS before testing.
        1.1.3. Note: Specimens may only be tested if they are *fully* defrosted.
    1.2. Place absorbent underpad on work area (white side up)

2. MTS Setup (~ 25 minutes)
    2.1. Install load cell (M3337) and connect extensometer (2103).
    2.2. Clamp spherically seated platen in the top grips; align base below.
    2.3. Ensure platens are properly aligned.
    2.4. Start the MTS (see SOP entitled "MTS Test Suite"). Lower crosshead to optimal height above lower platen.
    2.5. Calibration - Connect proper calibration files for load cell and extensometer to the machine in "Calibration" mode (password: Calibration)
        2.5.1. In Station Manager…
            2.5.1.1. Display > Station Setup
                2.5.1.1.1. Channels > Ch 1 > Force
                2.5.1.1.2. Sensor - verify "M3337-force" calibration file is attached - if it is not, "Assign"
                2.5.1.1.3. Channels > Ch 1 > Strain
                2.5.1.1.4. Sensor - verify "extensometer1inchMax" calibration file is attached - if it is not, "Assign"
                2.5.1.1.5. Click Save
    2.6. Tuning - Verify tuning values are properly assigned for crosshead displacement control in "Tuning" mode (password: Tuning)
        2.6.1. In Station Manager…
            2.6.1.1. Display > Station Setup
                2.6.1.1.1. Channels > Ch 1 > Displacement
                2.6.1.1.2. Click Tuning icon (left)
                2.6.1.1.3. P = 30, I = 3, D = 0.03061
                2.6.1.1.4. Click Save
3. MTS Testing (~ 10 minutes per specimen)
    3.1. Using calipers, measure specimen height 4x. Calculate the average height (H_{AVG}).
    3.2. Calculate scaling ratio (between extensometer and specimen) by dividing the average height (H_{AVG}) by extensometer gauge length (25 mm).
    3.3. Using scaling ratio (and calibration factor for uncalibrated sensors), calculate extensometer strain (rate) and corresponding displacement (rate) values corresponding to 0.3%, 8%, and 0.5%/s.
    3.4. Note: Keep specimen submerged in 1x PBS between steps.
    3.5. Load sample into the MTS. Place VB on bottom platen. Center the bone directly below the upper platen.
    3.6. Lower top platen to just above top of VB. Change displacement range to 10mm.
    3.7. Go to displacement control and zero load.
    3.8. Lower top platen onto the specimen VERY SLOWLY to manually preload to 2-3 "N" (units in quotations because this is what the MTS is displaying, not the calibrated value i.e. reality. In reality, this is ~10 N).
    3.9. Tighten the screws on the upper platen to secure in place.
    3.10. Add extensometer, remove pin, zero strain value and check offset (should be <7%).
    3.11. Check interlocks:
        3.11.1. Load value: +/- 200 lbf
        3.11.2. Strain: +/- 1.95%

3.11.3. Displacement: +/- 2 mm

3.12. Run test (“SRE_RatVBMono”).

3.13. When prompted, manually input the values for the current specimen:

Specimen ID: (e.g. D01_L4)
Displacement rate (0.5%/s): (e.g. 0.023 mm/s)
Preload displacement (0.3%): (e.g. -0.014 mm ← this must be negative!!)
Ramp displacement (8%): (e.g. -0.365 mm ← this must be negative!!)

3.14. Execute test. Note: After 5 cycles of preload, you must manually click the “preload okay!” button to proceed with ramp to 8% strain. You need to verify F-d curve is behaving correctly before proceeding (i.e. overlapping during preconditioning).

3.15. Once the test has completed, verify that strain has returned to zero. Insert extensometer pin and remove extensometer.

3.16. In manual control, raise the platen (~ +5mm) off of the sample.

3.17. Remove sample, loosen upper platen.

3.18. Repeat Step 3 for each specimen.

Biomechanical Testing					
Specimen #:			Date:		Time:
Program File Name:			Test Run #:		Notes:
Specimen Height					
H_1	H_2	H_3	H_4	H_{AVG}	
Strain					
Scaling Ratio (H_{AVG}/H_{EXT})	Disp Rate, mm/s (0.5%/s)	Precond., mm (-0.3%)	Ramp, mm (-8%)	Make sure strains are negative!	
Pre-Test				Test	
Preload (N)	Upper Platen Tightened	Extensometer Pin Out	Interlocks Set	Check Preconditioning	
Post-Test					
Peak Load (N)		Loosen Upper Platen			